Physical properties of basaltic glasses

Lönnroth, Nadja Teresia

Publication date:
2009

Document Version
Publisher's PDF, also known as Version of record

AALBORG UNIVERSITY

PhD Dissertation

Physical properties of basaltic glasses

by
Nadja Lönnroth

Section of Chemistry
Department of Biotechnology, Chemistry and Environmental engineering
Aalborg University

Date of defence
30.3.2007

Assessment committee
Tanguy Rouxel
Méchanique des Materiaux Fragiles
Université de Rennes 1, France
Reinhard Conradt
Department of Glass and Ceramic Composites
RWTH Aachen University, Germany
Ryszard Pyrz
Aalborg University

Supervisor
Yuanzheng Yue
Aalborg University

Defended 30.3.2007
Accepted by the Faculty of Engineering, Science and Medicine 20.6.2007
Text reviced according to assessment committee advises

Printed in Denmark by
UNIPRINT, Aalborg University, November 2009
ISBN 978-87-90033-62-0

Abstract

Basaltic stones are used as raw material to produce insulation fibers and glass ceramics. It is affordable to use, as it is very abundant. The composition of basalt varies with the location of collection, influencing the processing methods and the quality of the product. In this study some aspects important for fiber production of basaltic composition are discussed.

There exists a general understanding of the effect of single elements on the final glass. Here is presented a systematic study around a composition used in insulation fiber. Variations in composition change the physical, the mechanical and the thermal properties of the glass. In future, this information can be used to optimize the composition of the glass to fit the requirements of the final fiber product.

Basaltic melts crystallize at a relatively high temperature and correspondingly the crystals need high temperature to melt. When producing glass, it is very important to ensure that the material is fully molten and homogenized, as inhomogeneities will deteriorate the mechanical properties of the glass and reduce its durability. During fiber production the dwell time for the melt is rather short, so it is necessary to know that all crystals melt during that time. With the study on the crystallization and melting processes of typical wool fiber compositions the weakness observed in some cases can be understood. Further, it is observed that the liquid remembers the crystal structure at temperatures above liquidus.

Generally, mechanical properties of short and thin glass fibers are difficult to measure. Within traditional methods tensile strength is the only applicable method. By nanoindentation both hardness and elastic modulus of the tested sample can be determined. As the last part of this work nanoindentation is introduced as a new method for fiber testing.

Dansk resume (Danish abstract)

Basaltiske stene bruges som råmateriale i production af stenuld for isolering og i udvalgte glas-keramiske produkter. Basalt eksisterer over alt på jorden og er således en billig råvare. Den kemiske sammensætning varierer mellem samlingsstederne og det vil påvirke kvaliteten af produkterne og produktionsmetoden. I dette studie gennemgås flere aspekter, der er vigtige for produktionen af isoleringsulds fibre af basaltisk sammensætning. Dette fuldføres med tre underpunkter.

Effekten af de enkelte elementer i en glas er vel forstået. I dette studie bruges en glas med gennemsnits-sammensætningen af fabriksproduceret stenuld, hvori variationer er introduseret for at kunne udføre et systematisk studie. Ændringer i sammensætningen foråsager ændringer i de fysiske, mekaniske og termiske egenskaber af glaset. I fremtiden kan denne information anvendes til at optimere sammensætningen af glasset til de enkelte formål.

En basaltiskt smelte krystalliserer ved en relativt høj temperatur og modsvarende kræver krystallene høj smeltetemperatur. Under glas-produktion er det meget vigtigt at sikre sig, at materialet er helt smeltet og homogeniseret. Inhomogeniteter reducerer styrken af glaset og holdbarheden af produktet. Under fiber-produktion befinder materialet sig kun i kort tid i smeltet tilstand, så det er vigtigt at sikre sig at alle krystaller smelter i løbet af den tid. Med dette studie af krystallisation og smelteprocesser af typiske uldsammensætninger kan svaghederne i nogle fibre forstås bedre. Desuden kunne observationen om struktur i væskefase blive konfirmeret.

Generalt er det svært at måle mekaniske egenskaber af tynde og korte glasfibre. Den eneste metode, som bliver brugt, er træstyrkemålinger. Med nanoindentation kan både hårdhed og elastisk modul af prøvematerialet bestemmes. I den sidste del af dette arbejde introduceres nanoindentation som en ny metode til glasfiberprøvning.

Contents

Foreword

This work was made possible by Rockwool International. The company's interest in a higher level of knowledge within basalt glass and fiber properties led to the formation of the Myrddin project. My employment as a PhD student is a part of the project and I hope that the information that I have gained also will gain Rockwool in the future. I thank my contact persons at Rockwool, Marianne Guldberg, Søren Primdahl and Dorthe Lybye, for feedback, discussions and ideas. The work will be presented as a plurality, with an introduction and some discussion on the different issues that I have worked with, followed by the articles written for publication. The articles contain all main results and discussion of them, and generally, this information will not be repeated in this introduction.

Part of this work was made at The Pennsylvania State University, Materials Research Institute. Without the generous help and funding by Professor Carlo Pantano in experimental techniques and instrument time, the contents of this book would be much thinner. I am also grateful for the inspiring discussions that we had, giving me a glimpse of the ocean of knowledge in the glass world.

Aalborg has been a nice base for my three last years and a good place to conduct a PhD study. Especially, I would like to acknowledge my colleges in the glass group Lasse Hornbøll, Majbritt Lund and our professor Yuanzheng Yue who always has been positive what ever obstacles there were ahead.

Background and objectives

The starting point for the idea of this project came from a product related problem that puzzled the research and development section in Rockwool International A/S. The same type of insulation wool product was made from two different sets of raw-materials, though mixed such that the end compositions were the same. The mechanical properties of the two products were very different, the one qualifying for sale and the other not. In preliminary tests, such as a sieving test, it seemed as though the other one was much more prone for breaking, more brittle. As all the other production steps were similar for the two products, it was decided that there has to be some differences in the glass itself that are not understood. From this background a project, Myrddin, was set up with the goal to better understand the mechanical properties of the fibers with relation to glass composition and forming conditions and to tackle the problem with the brittle fibers. Brittleness of bulk glass exists as a term and can be measured by determining the indent and crack sizes that originate from performing Vickers micro indentation tests on the surface. But there is no way to measure brittleness of fibers, and even more important there is no common definition on that. It was decided to approach the goal by three distinct sub-projects.

The first issue was to study the glass fibers in the two wool products where the problem with brittleness was discovered. Some preliminary studies had revealed that there were differences in the crystallization process. Thus a fairly large study on crystallization by differential scanning calorimetry (DSC) in different atmospheres was made, as the melting of the raw materials affects the quality of the produced fibers as well as if crystallization occurs during the fibrication process.

Secondly, as tensile strength was the only quantitative mechanical measurement performed on the fibers, it was evaluated that information such as hardness and elastic modulus of the fiber glass would be of great interest. Firstly, none of these parameters were known and secondly, as the cooling rate of fibers compared to bulk glass is different it was known that the structure of the glass in fibers would be different. Nanoindentation is the only technique to get hardness and elastic modulus on fibers due to their diminiscule size. After preliminary experiments, it was concluded that it is possible to indent fibers, and thus developing a nanoindentation measurement technique to be

used on fibers was set as a goal.

The third part of the project was to investigate general relationships between changes in the chemical composition of the basalt glass and changes in the thermal, rheological and mechanical properties. All measurements are made on bulk glass, so here brittleness measurements by Vickers micro indentation will be included, in order to investigate the effect of chemistry on brittleness.

Chapter 1

Introduction

1.1 Production process of stone wool fibers

Production of stone wool is based on cheap raw materials, basalt stones that are heated by burning of coke. To get a desired chemical composition of the final product, bricks with the needed additives are combined with coke and basalt stones. These three ingredients are charged into the cupola furnace. The coke are ignited from below and the basalt stones and bricks will start to melt when the temperature is sufficiently high. The temperature of the melt in the middle of the furnace is approximately 1500°C. The melt flows down between the remaining blocks and fills the bottom of the furnace. The hold time for the melt in a temperature above 1500 °C is only about 15 min. From the bottom of the furnace melt runs out onto the spinner wheels, that rotate at a high speed (Figure 1.1). Due to the centrifugal force, tiny droplets of melt are slung away from the wheels, each droplet trailing a fiber as it leaves the wheel. Thereafter, the fibers are blown away from the wheels to a catcher net while simultaneously sprayed by coating polymers to bind the fibers together. More information is given in Axten et al. (1993) and Mohr and Rowe (1978).

The burning environment in the cupola furnace is extremely reducing. In the burning process of coke, coke will oxidize from C^0 to C^{4+} by using atmospheric oxygen, but as that is used quickly, the transition metal ions of basalt will be reduced. In basalt there is considerable amounts of iron (5-13 wt % Fe_2O_3), the iron will be reduced from Fe^{3+} to Fe^{2+} and partly to Fe. Thus, nearly all iron oxide in these fibers will be FeO.

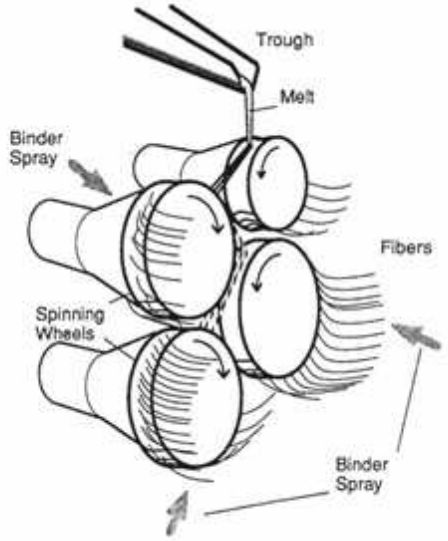

Figure 1.1: Melt from the cupola furnace flows down on the spinner wheels, where fibers will be drawn by droplets slung away from the wheels by centrifugal forces.

1.2 Mechanical properties of fibers

1.2.1 Strength of glass

By theoretical calculations, strength σ_m of a brittle solid, i.e the tensile stress required to separate two atoms a distance a_0 apart, is given by

$$\sigma_m = \sqrt{E\gamma_s/a_0}, \tag{1.1}$$

where E is Young's modulus and γ_s the fracture surface energy. This is valid for glasses as there is essentially no plastic flow or other mechanism for stress relief at the crack tip. Using typical values for glass $E = 70$ GPa, γ_s =3.5 J/m^2 and $a_0 = 0.2$ nm gives $\sigma_m = 35$ GPa which is extremely high. It makes silicate one of the strongest materials, but in general the measured strength values for glass are several orders of magnitude smaller than that due to external defects.

By the intrinsic strength of a glass is meant the strength of the glass network structure when no extrinsic issues cause degradation of strength. The intrinsic properties of glasses vary with thermal history and chemical composition, as these change the atomic structure and bonding of the glasses. Intrinsic strength of glass structure has been measured by 2-point bending tests performed in vacuum directly after fiber drawing, on fibers that have not undergone any contact. Measurements on such fibers confirm that the strength of glass is high, the measured intrinsic strength reaches values of up to 1/3 of the theoretical strength (Kurkjian et al., 2003; Lower et al., 2004), compared to bulk glass that has strength of the order of 1/1000 of the theoretical strength.

1.2.2 Tensile strength

Generally the tensile strength of fibers is much larger than the tensile strength of bulk glasses. A sample under tension breaks at the point where the stress concentration is largest. These stress concentrations occur usually at places with structural defects in the glass, such as gas bubbles, intrusions or crystallites, where the stress will not be evenly dispersed. When stress exceeds the fracture strength values the sample will break, the crack starting from this point. The larger the defect is, the easier the sample will break. This follows directly from Griffith's law on fracture (Griffith, 1921).

$$\sigma = \sqrt{\frac{2E\gamma_s}{\pi a}}, \tag{1.2}$$

where E is Young's modulus, γ_s the specific surface energy and a is one half of the length of an internal crack. This gives the criterion for crack propagation of an elliptical crack. The basic idea is that during the propagation of the crack there is a release of elastic strain energy, which is used on the increase of surface energy of the system due to the formation of new free surface at the crack faces. Applying this to fibers, it is evident that the dimensions of the fiber restrict the size of flaws that can be incorporated in it. Thus theoretically the thinner the fiber is, the smaller defect there can exist and thus the average strength of fibers increases with decreasing fiber diameter.

It has been long known that the tensile strength of fibers is dependent on the drawing ratio i.e. the ratio between die and fiber diameters, and that the higher drawing ratio the higher is the tensile strength of the fibers (Bartenev, 1970). And if fibers of different diameters are produced under identical drawing ratio conditions, their strengths are identical within experimental limits. This is also apparent from Ohe von der (2003), but here is further found a strong relationship between tensile strength and the forming stress of the fiber itself.

The production method by which the fiber is spun has a considerable effect on the actual strength of the fiber. Continuously spun fiber is not in contact with any surface until it is wound onto the collection wheel, and by that time it is totally cooled and the surface stays mainly intact. In contrast to fibers produced by cascade spinning or flame attenuation, where fibers are blown away in a bunch and fibers will be in contact with each other from the beginning. Contact causes defects on the fiber surfaces or causes fibers to break into short pieces, to be deformed or even to emerge into each other.

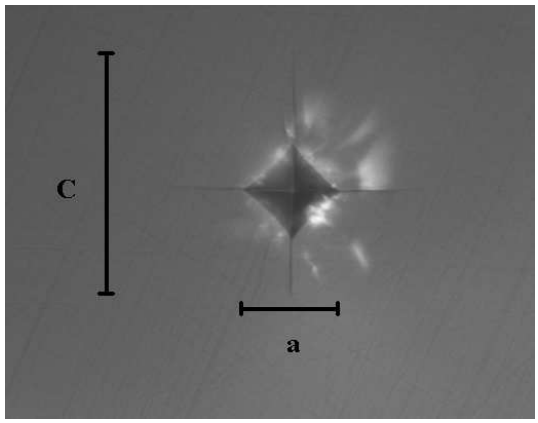

Figure 1.2: Image of a Vickers indentation depression on glass 8 of section 3. a is the diagonal of the indent and C is the half size of the radial cracks.

1.3 Hardness and fracture toughness

1.3.1 Hardness

Hardness is the oldest test method to determine a mechanical property of a material and it is a measure of the materials resistance to localized plastic deformation. Hardness is given on Moh's scale, which is determined by a natural minerals ability to scratch the test material. The very soft lime is in one end of the natural testing minerals and diamond as the hardest material in the other. The more quantitative way to determine hardness is by indentation experiments, usually Vickers hardness, where a diamond pyramid is pressed into a material under controlled load and rate conditions. The depth and size of the resulting indentation is a measure of the hardness number, the lower the value the softer the material and the larger and the deeper the indentation. The measured hardnesses are mostly relative, so care should be taken when comparing values determined by different techniques or already by different loads. For Vickers hardness, H_V

$$H_V = \frac{P}{\alpha_0 a^2} \tag{1.3}$$

where P is the applied load, a the characteristic dimension of the impression (Figure 1.2) and α_0 an indenter constant. A basic reference to indentation is Lawn and Marshall (1979).

The mechanism by which materials flow under an indenter are various, from plastic and viscous flow to volume flow i.e. compaction or densification. In soda-lime-silicate glass, at room temperature, shear flow is the method that leads to permanent deformation and it can be verified by visible shear lines at the faces of the indentation. In fused silica on the other hand, compaction is the method of deformation (Kurkjian and

Kammlott, 1995), which can be seen in refraction index measurements or by the lack of shear lines. In the case of plastic flow, pile-up of the material is clearly seen around the indentation impression, though the volume of it seldom equals the impression volume.

Origin of intrinsic hardness in perfect crystals

In covalent crystals hardness is an intrinsic property and equals to the sum of resistance of each bond per unit area. This resistant force of a bond is characterized by the energy gap and the amount of bond per unit area is determined by the valence electron density.

For polar covalent crystals both the covalent and the ionic component has to be considered. Here an electron-pair is partly screened due to the ionic bonding and this causes a lower effective covalent bond number. This is described by a falling exponential factor. The resulting hardness can approximately be described by an exponential function of ionicity (Gao et al., 2003). To have an extremely hard material all the following conditions have to be met: high bond density, short bond length and great degree of covalent bonding.

In comparison to hardness of crystals the origin of hardness of glasses is much more complicated. Since in glasses the bond angles and lengths are described by distributions around optimal values and the free volume within the network is large and randomly distributed. Therefore, establishing a precise theoretical model is a challenge and has not been done.

1.3.2 Fracture toughness

Fracture toughness is a measure of a materials ability to resist fracture when a crack is present and is generally given by

$$K_{Ic} = Y\sigma\sqrt{\pi a} \tag{1.4}$$

where σ is applied stress a is the length of a surface crack or half of the length of an internal crack and Y is a parameter that depends on both crack and specimen sizes and geometries.

Fracture toughness is a fundamental material property that depends on many factors where the most influential ones are temperature, strain rate and microstructure of the material. For Vickers indentation there is found a relation between K_c and the half of the mean size of the two radial cracks C (see Figure 1.2)

$$K_c = \chi\frac{P}{C^{3/2}} \quad \text{where} \quad \chi = \xi_0 \tan\phi\sqrt{\frac{E}{H_V}} \tag{1.5}$$

where P is applied load, E is Young's modulus, H_V the measured hardness and ξ_0 is a dimensionless constant where $\phi = 136°/2$ is the opening angle of the indenter pyramid.

1.4 Brittleness of glass

For a long time fracture toughness was regarded as a measure for brittleness, however fracture toughness values for glass are all in a narrow range and may, therefore, not be indicative of brittleness. Lawn and Marshall (1979) proposed the concept of brittleness from the notion that all materials experience deformation at low loads and fracture at high loads. Since hardness and fracture toughness describe the deformation and fracture behaviors Lawn and Marshall (1979) defined brittleness as the ratio of hardness to fracture toughness which can be estimated from the ratio of the median crack length to the diagonal length of a pyramidal deformation impression.

$$B = \frac{H_V}{K_c} = \frac{\beta_0}{\alpha_0 a^{1/2}}(\frac{C}{a})^{3/2}, \tag{1.6}$$

where C is characteristic crack length, a the indentation diagonal length, β_0 is obtained from hardness data and Young's modulus and α_0 is the indenter geometry constant. More conveniently brittleness can be defined as (Sehgal et al., 1995)

$$B = \gamma P^{-1/4}\big(\frac{C}{a}\big)^{3/2} \tag{1.7}$$

where P the indentation load and γ is a function of hardness and Young's modulus and it is $\gamma = 31.3 \times 10^{-3} H_V^{3/4}/E^{1/2}$. Within the range of typical inorganic glasses it is valid that $\gamma = 2.39\mathrm{N}^{1/4}\mu\mathrm{m}^{1/2} \pm 5\%$.

Brittleness is a relative susceptibility of a material to two competing mechanical responses, deformation and fracture. The measurement of crack initiation load is a manifestation of the competition of deformation and fracture, because it involves a ductile to brittle transition from deformation without cracking at smaller loads to cracking at larger load. A material with smaller brittleness has a larger crack initiation load (Sehgal and Ito, 1999). Brittleness of normal glasses decreases with density due to the ease of both plastic flow and densification. Brittleness has a minimum between densities 2.3 g/cm^3 and 2.4 g/cm^3 for SiO_2-based glasses (Figure 1.3). On the other hand, the brittleness of anomalous glasses (SiO_2-based glasses with densities approaching that of silica i.e 2.2 g/cm^3) increases with decreasing density due to the lack of plastic flow. In an indent this as seen as a lack of shearlines.

As a summary brittleness is believed to depend on stress relaxation due to densification and flow modes of deformation before crack initiation. If density is above 2.4 g/cm^3, the glasses have a large amount of alkali and alkaline earth oxides thus flow is possible but due to high density, densification is difficult. The opposite also applies if density is below 2.4 g/cm^3 then the glasses have rigid 3D-networks with open space, so densification is possible but flow is difficult (Ito, 2002).

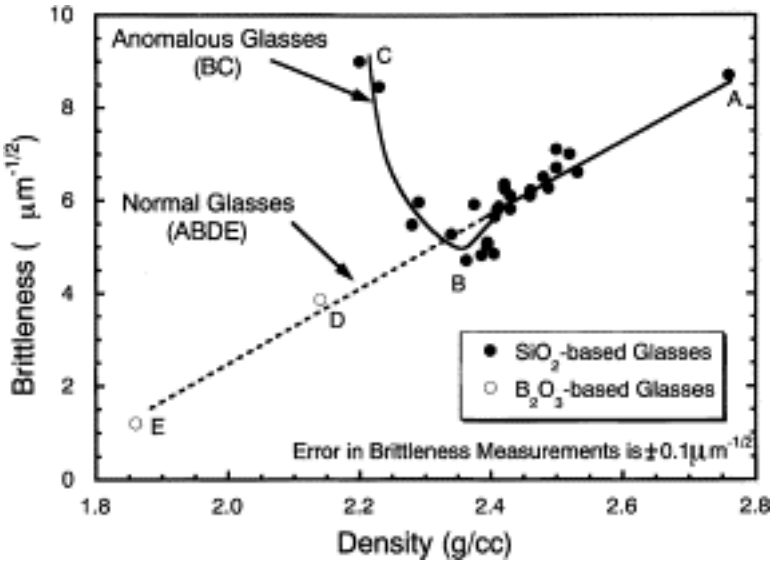

Figure 1.3: Brittleness of glasses in the SiO_2- and B_2O_3- based glasses as a function of density. Anomalous glasses are on the BC line and normal glasses on the AB line. Lines are for guidance of the eye. (Sehgal and Ito, 1999)

Another way to define brittleness is provided by Quinn and Quinn (1997). This is based on the thought that brittleness is defined by hardness, fracture toughness and Young's modulus.

$$B = \frac{H_V E}{K_c^2} = \frac{H_V}{G_c} = \frac{H_V}{2\gamma_f}, \tag{1.8}$$

where G_c is the critical strain energy release rate and γ_f the fracture surface energy. As H_v, the hardness in units of force per area is also directly proportional to the work per unit volume of deformation, then B compares deformation and fracture processes

$$B \propto \frac{\text{deformation energy per unit volume}}{\text{fracture surface energy per unit area}}. \tag{1.9}$$

Recently, molecular dynamics simulations have been conducted on the low brittleness glass to understand the mechanism of deformation and fracture in that versus normal soda-lime silicate glass (Ito, 2004). Under low tensile stress or pressure, the glasses showed mainly elastic deformation which is concluded to be related to changes in the Si-O-Si bond angles. Under higher stress or pressure levels both flow and densification of the glasses is observed. This deformation is more prominent under tensile stress than under pressure and it is caused by structural rearrangement of the network and by the movement of modifier ions.

1.5 Nanoindentation

Nanoindentation is an indentation method that measures both depth and load during the indentation process. The technique relies on high-resolution instruments that continuously monitor the load and displacement of the indenter as it is pushed into or withdraw from the material. The data gained is load-displacement data of cycles of loading and unloading that can be analyzed to derive a variety of mechanical properties, most commonly hardness and elastic modulus. The difficult task in nanoindentation is to understand the information contained in the loading-unloading curves, both due to the complex elastic and plastic deformation processes that occur during indentation and to the non-uniformity of the stress and relaxation fields in the vicinity of the contact.

The characteristic scaling dimensions for covalent-ionic solids are layer thickness, scale of micro-structure in the material and the contact dimension, and when these diminish it is generally observed that strength increases and toughness decreases (Lawn, 2004). Further it is observed that the nature of flaws that control strength properties of brittle solids change at the nanoscale region.

1.5.1 Theory

Determining hardness (H) and (reduced) elastic modulus (E_r) is done from the information in the loading-unloading curve (Figure 1.4). The usual method to analyze load-displacement data is by the method of Oliver and Pharr (1992). The main points of this method will be described next. The unloading curve is fitted to an empirical power-law equation

$$P = \alpha(h - h_f)^m \tag{1.10}$$

where P is indentation load, h is indenter displacement, α and m are empirically determined fitting parameters and h_f is the final displacement after complete unloading, also determined by curve fitting. By differentiating equation (1.10) at the maximum penetration depth $h = h_{max}$ the initial unloading stiffness S can be established.

$$S = \frac{dP}{dh} \tag{1.11}$$

Further the contact depth h_c is defined as the depth along which the indenter and the specimen are in contact at maximum load. This is not the same as the maximum depth as the material undergoes elastic deformation and the surface will bend close to the indenter, so $h_c < h_{max}$.

$$h_c = h_{max} - \epsilon\frac{P_{max}}{S}, \tag{1.12}$$

where P_{max} is the load at maximum displacement h_{max} and ϵ is an indenter geometry constant with the value 0.75 for the Berkovich indenter tip (Oliver and Pharr, 1992). Though later a model for the effective shape of the indenter gives $\epsilon = 0.76$ (Pharr and Bolshakov, 2002). The contact area i.e. the projected area of contact is for a perfect Berkovich tip $A_c = 24.5h_c^2$. A real tip is always rounded at the edge, thus we have $A = f(h_c)$. This tip area function is determined experimentally by indenting a known substrate that has a known modulus which does not change with depth, fused silica. How true this assumption is, I will not go into here. This is the generally used calibration method, even though there is several studies indicating that the area defined by experimental indentation is larger than the true area determined by AFM imaging (Van Landingham, 2003). With the contact area we get the hardness

$$H = \frac{P_{max}}{A_c} = \frac{P_{max}}{A(h_c)}, \tag{1.13}$$

and the reduced elastic modulus, where information on both the specimens and the indenters elastic modulus is included

$$E_r = \sqrt{\frac{\pi}{A}}\frac{S}{2}. \tag{1.14}$$

The elastic modulus of the specimen itself can be calculated by

$$\frac{1}{E_r} = \frac{1-\nu_s^2}{E_s} + \frac{1-\nu_i^2}{E_i}, \tag{1.15}$$

where ν is the Poisson's ratio and the subscripts s and i denote sample and indenter respectively.

As nanoindentation measures point information, it will detect small changes in the structure. These can be caused for example by temperature shifts or by varying the stress state (Tsui et al., 1996; Kese et al., 2004)

1.5.2 Indentation size effect, ISE

Most materials exhibit ISE, i.e. the apparent hardness decreases with increasing peak load (indentation size). Often ISE is described using the empirical Meyer's law, which correlates the test load with the resulting indentation size with a simple power law.

$$P_{max} = Ah_c^n \tag{1.16}$$

where A and n are constants derived from curve fitting.

Five empirical or semi-empirical equations have been employed to describe the nanoindentation data of ceramics and glass. It is proved that each of them is satisfactory in describing the relationship between peak load and the resulting indentation size

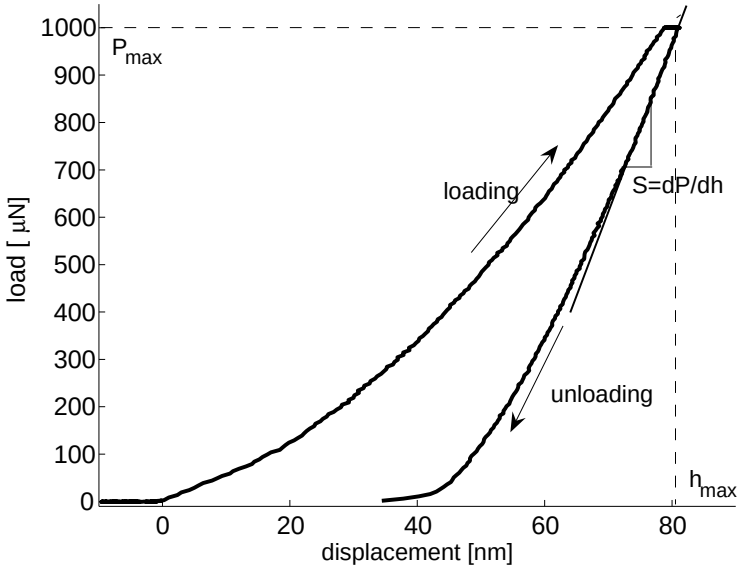

Figure 1.4: A typical loading-unloading curve, where the information needed for determining H and E_r is noted.

(Peng et al., 2004). The models are Meyer's law, Hays-Kendall approach, PSR model, elastic recovery model and modified PSR model. The analysis reveals that the observed ISE is a complex phenomenon and cannot be explained based on a unique mechanism. Each of the models has some drawbacks in their interpretation or description of the parameters. The mechanisms that contribute to ISE include the surface effect i.e. the ratio of surface to volume displaced by the indenter, the strain gradient effect i.e. the geometrically necessary dislocations produced due to the indent, and compaction of the material (Manika and Maniks, 2006).

The main goal of describing ISE is to find a way to determine the so-called true hardness for material characterization. The values determined based on three of the models (PSR, elastic recovery and modified PSR) in the study are in good agreement with each other. This can be attributed to the similarity of the models, as all of them can be considered to be truncated forms of the polynomial series representation of the applied load (Bückle, 1965).

Indentation size effect depends on the materials hardness, as the density of geometrically necessary dislocations increases with decreasing indentation depth. Thus very little ISE is expected on hard materials (Fischer-Cripps, 2004). For nanoindentation at low loads surface effects dominate the load-displacements characteristics, while at greater depths the bulk properties dominate.

1.5.3 The power law relation

With a theoretical study it has been possible to understand the varying results acquired in different indentation studies (Meinhard et al., 1997). It is found that the loading regime used has an effect on the power law that describes the process, there has not been paid attention to this aspect before. The general flow law reads for flow stress σ

$$\sigma = m_D b \dot{\epsilon}^m. \tag{1.17}$$

where m_D is a geometric constant of the deformation process, b is the factor of viscosity and m is the exponent of the strain rate sensitivity. For $m = 1$ the equation 1.17 describes Newtonian flow and then b is the Newtonian viscosity. For hardness measurements this yields

$$\sigma = m_D HU, \dot{\epsilon} = \frac{dh/dt}{h}, \tag{1.18}$$

where h is indentation depth, and HU the Universal Hardness, which is equal to the flow stress. From here it is inevitable that the strain rate $\dot{\epsilon}$ (and thus hardness) decreases with increasing indentation depth in penetration experiments. The indentation force F is given as the resistance of the material to the penetration of the indenter.

$$F = kHUh^2 = kb(\frac{\dot{h}}{h})^m h^2 \tag{1.19}$$

where k is the geometric constant of the indenter. This equation is proved experimentally by using three different loading regimes:
i) constant indentation rate

$$\dot{h} = \dot{h}_c = const \tag{1.20}$$

ii) constant loading rate

$$\dot{F} = \dot{F}_c = const \tag{1.21}$$

iii) variable indentation rate at constant piston speed

$$\dot{h} = \alpha\beta t^{\beta-1}, h = \alpha t^\beta \tag{1.22}$$

These experiments allow measurements $F(h)$, $F(t)$ and $h(t)$ and the relations can be derived with equations (1.19-1.22). All the cases will end as a power law:

$$F(h) = ah^n \tag{1.23}$$

$$F(t) = a't^{n'} \tag{1.24}$$

$$h(t) = At^B \tag{1.25}$$

The so-called Meyer parameters of these equations a, a', A and n, n', B can be determined by the parameters m and b of the flow equation (1.17), shown in table 1 and 2 in

Meinhard et al. (1997). The Meyer parameters depend on the loading regime and the material constants. With the relations between the different loading regime parameters solved, the indentation results of the regimes are consistent.

Generally, when indenting the loading curve should follow a power law. The exponent is determined by the effective shape of the tip, meaning the real area in contact with the indented material. For a perfect Bercovich tip this shape is a parabola and thus in the loading regime equation (1.26) is valid (Hainsworth et al., 1996).

$$P = Kh^2 \tag{1.26}$$

Here P is load, h the contact depth and K a constant that can be evaluated analytically and is a function of H and E and the shape of the indenter (Malzbender et al., 2000; Troyon and Martin, 2003). With a rounded tip h should be replaced by $h + h_b$ where h_b is the distance between the blunt end and the perfect end of the indenter cone.

Chapter 2

Chemistry of basaltic glasses

2.1 Basalt

Basalt is a common black to gray volcanic rock type. It is usually fine grained due to the rapid cooling of lava. By mineralogical terms basalt consists mainly of calcic plagioclase, feldspar and pyroxene (augite), also olivine can be a major constituent. Other minerals that can be present in relatively small amounts include iron oxides as magnetite, ulvospinel and ilmenite. Typically, basalt contains several oxides with a large variation in the composition depending on the origin. Basalt compositions are generally rich in MgO and CaO and low in SiO_2 and in the sum of Na_2O and K_2O compared to most other common rocks, and it has high liquidus and solidus temperatures relative to other igneous rocks. Generally, basalt has a composition with 45-55 wt% SiO_2, 2-6 wt% in total alkali oxides, 0.5-2 wt% TiO_2, 5-13 wt% FeO, 5-12 wt% MgO, 10 wt% CaO and 14 wt% or more of Al_2O_3.

2.2 The glassy state

2.2.1 General aspects

Glass is a under cooled liquid, where the structure of the liquid is frozen in when the liquid is cooled. When the timescales of relaxation in the liquid become long, longer than the experimental timescales, we have a frozen-in structure with no changes in time. From this point on we can talk about a glass. Generally, the temperature where the transition from a liquid to a glass happens is called the fictive temperature of the glass (T_f) and it describes the temperature at which, the liquid structure is frozen in. The higher the cooling rate used, the higher will the fictive temperature of the glass be. When a cooling rate of 10 K/min is used, then the glass is defined as a 'normal glass'

with respect to its structure and its fictive temperature is called the glass transition temperature T_g (Yue, 2008). By this definition different glasses can be compared, as they are related to a relaxation time of 100 s and the viscosity of the system is 10^{12} Pas at the glass transition temperature.

A glass is a solid amorphous state without repeating lattice units, i.e. glass does not have long range order. The short range order (SRO), is fairly strictly defined by the bonds between adjacent atoms. The nearest neighbor distances are very similar for the crystalline and glassy counterparts, for example for SiO_2, quartz and fused silica have d(Si-O)$\sim$0.162nm and d(O-O)$\sim$0.265nm respectively (Shelby, 2005). The differences become larger over larger distances, for example already in the Si-O-Si angle in the silica tetrahedral. The angle has an exact value for the crystal (144°) but it has a distribution around the crystalline angle (120-180°) in the glass. Further order, such as medium range order (MRO) or intermediate range order in glass has been discussed quite a lot lately eg. (Conradt, 2004; Henderson et al., 2006). This would include building blocks, distances, larger than one tetrahedra such as rings or chains as we know them from crystals, but where the dimensions are still relatively small. Real, quantitative, proof for intermediate range order has not yet been presented.

2.2.2 Structure of aluminosilicate glasses

The general silicon oxide glass structure is based on silicate tetrahedra, which are connected to each other at all four corners to form a three dimensional network. Then all the oxygens in the glass are bridging oxygen (BO) and the glass has a high connectivity. Disorder to the structure comes from variability of the Si-O-Si angle connecting adjacent tetrahedra and from rotation of single tetrahedron.

Addition of alkali oxides (usually of Li_2O, Na_2O, or K_2O) produces alkali silicate glasses, and generally the addition reduces viscosity of the melt, decreases the glass transition temperature and increases the refractive index, density and thermal expansion coefficient. Each alkali ion creates a non-bridging oxygen (NBO), as the oxygen ion must bind to the alkali ion in the vicinity of a such to maintain local charge neutrality. The alkali ions occupy free space (interstitial positions) in the network thus the free volume is decreased, the reason for the increased density. The increase in NBO content makes the network structure weaker and decreases viscosity and T_g.

Combining earth alkaline oxides (MgO, CaO, SrO or BaO) with alkali oxides and silica produces ternary glasses. The most known glass in this group is soda-lime-silica glass, that usually has 10-20% Na_2O, 5-15% CaO and 70-75% SiO_2. The principal structural model of these alkali/alkaline earth silicate glasses resembles that of the alkali silicate glasses. The alkali ions (R^+) needed one neighboring NBO, while the

earth alkaline ions (R^{2+}) will need two NBO's to maintain local charge neutrality. This bonds the alkaline earth ions more tightly to the network, increasing the strength of the network and reduces the mobility of the ions, so the net chemical durability is increased.

The next step in producing a usual glass would be to add aluminum oxide, Al_2O_3, to get an alkali/alkaline earth aluminosilicate glass. Alumina is generally added due to its favorable properties increasing T_g and T_C. Aluminum can occur in both tetrahedral and octahedral coordination in crystalline materials, and this is also expected in glasses. Generally, aluminum will occur in aluminum-oxygen tetrahedra and be part of the network. This will be the case as long as there are alkali and/or alkaline earth oxides of the same or higher concentration than alumina in total. As each aluminum-oxygen tetrahedra has a charge of -1, it needs to be charge compensated by a cation. If this cation is an alkaline earth ion (R^{2+}) it can charge compensate two aluminum-oxygen tetrahedra and requires them to occupy sites nearby each other. But they are not necessary next to each other, as then they would produce a Al-O-Al linkage, which is not favorable (Loewenstein, 1954). This Al-avoidance principle states that the Al-O-Si linkage is more favorable than Si-O-Si or Al-O-Al linkages, and aluminum-oxygen tetrahedra tend to connect to four silicate tetrahedra (Mysen, 1995; Shelby, 2005). When the aluminum concentration exceeds that of silica ($Si/Al \leq 1$) more Al-O-Al bonds will occur and the amount depends on the charge balancing cations (Stebbins et al., 1999). The Al-avoidance principle has more effect on Na- than on Ca-bearing glasses due to the higher field strength of the later, where the Ca-bearing glasses have more Al-O-Al bonds (Lee and Stebbins, 1999, 2000), and the general effect of the Al-avoidance principle is that it increases the order within the melt, as there are rules where the different tetrahedra statistically have the highest probability to occur.

In glass technology, the terms used are network formers, modifiers and intermediates. All oxides can be divided into these groups that directly tell the task of each oxide within the glass. Based on the previous text it is easy to distribute the discussed oxides under these terms, taking into account that the cations in charge compensation sites are not counted as network modifiers, but being part of the network. Then Si^{4+} is the network former, Al^{3+} an intermediate, but when enough charge compensating cations are present it will be a network former and the modifiers will be Na^+, K^+, Mg^{2+} and Ca^{2+} that are not in charge compensating positions.

Lately it has been possible to directly prove the openness of the structure of a glass with high fictive temperature, which earlier has just been taken as a statement. Kiczenski and Stebbins (2006) have invented an apparatus where the cooling rate of the quenched glass is known. Applying ^{17}O MAS NMR to E-glass (isotopically enriched with ^{17}O) with different cooling rates the NBO content with changing T_f was observed.

An increase in Si-NBO was observed with increasing T_f with accompanying decrease in 4-coordinated B and increase in 5-coordinated Al (Kiczenski et al., 2005).

The structure of glass is also discussed in terms of Q^n units. A Si-tetrahedra fully bonded to the network by four bridging oxygen is a Q^4 unit. In such a glass all the oxygen are bridging oxygen. Similarly an isolated tetrahedra is a Q^0 unit. So the value of n gives the amount of bridging oxygen (BO) in a tetrahedra. When modifiers are added to a glass more NBO's are formed and the glass will consist of both Q^3 and Q^4 units. Q^2 units, tetrahedra with only two BO will not be present before all the Q^4 units are transformed to Q^3 units. A glass will thus consist in maximum of two types of Q^n units, depending on the amount of modifiers. A material with only Q^0 units is totally depolymerized, and the Q^n values are used to describe the connectivity of the structure. Though later studies (Neuville et al., 2006) indicate that there generally will be present more than two types of Q^n units in a glass.

2.3 Glasses from basalt

Glasses made from basaltic compositions belong into aluminosilicate glasses with both alkali and alkaline earth oxides. They also contain a considerable amount of iron oxide and generally some titanium oxide. Basalt glass composition (see section 2.1) differs somewhat from general glass compositions. It contains less SiO_2 and alkali oxides, more Al_2O_3 and has iron in either as FeO or in the oxidized form of Fe_2O_3. Referring to the previous section, silica is the main network former, and further all aluminum will act as a network former to compensate for the lack of silica in the glass composition. There are plenty of cations present in the glass for charge compensation of the aluminum-oxygen tetrahedra.

The oxidized form of iron oxide (Fe^{3+}) will also be a network former in tetrahedral coordination, and similarly to an aluminum tetrahedra it requires to be charge balanced by a cation. If there is not enough charge balancing cations, Fe_2O_3 will be a network modifier. In that case it needs three NBO's around and a large amount will cause a weak network structure. The Fe^{2+} in FeO is always a modifier and what was earlier written for earth alkaline oxides is valid for FeO also. It can be charge balancing two neighboring Al- or Fe- tetrahedra or when modifying the network it needs two NBO's in the close vicinity. Hence the Fe^{+}-ion is fairly tightly bonded to its site. Generally, the equilibrium oxidation state in a melt contains iron in both oxidations states; it is a function of composition, temperature and atmosphere.

The ratio between Fe^{2+} and Fe^{3+} in a melt reaches equilibrium in 2 hours with melt temperatures higher than 1335 °C and the structural relaxation of Fe^{3+} in octa- and tetrahedral coordination takes 6 h at 1405 °C and 2 h at 1500 °C (Nagata and Hayashi,

2001). All glasses prepared within this study are melted in minimum 4 hours at 1450 °C, thus we can expect that both the electronic and structural relaxation of iron ions are in equilibrium in the glass. The splitting into Fe^{2+} and Fe^{3+} in a representative basalt glass is measured by Mössbauer spectroscopy with the result that there is 60% FeO and 40% Fe_2O_3 (measurements performed by Steen Mørup at Copenhagen University). As all our basalt compositions are fairly close to each other and prepared in same way, it is assumed that the ratio between the oxidation states is the same in all samples. Glass transition temperature measurements for glasses with increasing $Fe^{2+}/\Sigma Fe$ show a decreasing T_g. This gives general information on the polymerization of the network, Fe^{2+} is the modifier and causes decrease in T_g and Fe^{3+} is the network former and increases the T_g, i.e. the temperature where the viscosity is 10^{12} Pas is higher for the more network former containing melt (Bouhifd et al., 2004).

Generally, basalts are not good glass formers, their melting temperature is high requiring a lot of energy for the melting process, the melt has a strong tendency to crystallize when cooled and the melt is very fragile. All these make the glass processing a tough task which has to be well controlled. The main use of basalt in glass form is as insulation wool, secondly it is employed as an glass ceramic where high hardness is needed and also some continuous glass fibers are produced and used as reinforcement material.

Chapter 3

Physical properties of basalt glasses

The study in this chapter is based on a set of basaltic glasses that are made using a basic batch received from Rockwool A/S, whereto additions of oxides are made. The compositions of the glasses are given in table 3.1, where added oxides are MgO (glasses 2-4), Al_2O_3 (glasses 5-7) and Na_2O (glasses 8-9). In glasses 5-9, the addition is made to glass 2, which is a composition close to Rockwool HT glass fiber composition. The results of this study are given in article IV. In this chapter the main results are given in table format with some background information on the topics and more detailed results on some parts, but in general the discussion of these results is given in article IV. The densities in table 3.1 are determined from mass and volume measurements by a helium pychnometer and the NBO/T values are calculated based on the compositions measured by XRF.

3.1 Characteristic temperatures

Due to the complexity of the compositions, the crystallization process and the following melting are not well defined. As will be discussed in chapter 4, basalts generally crystallize to spinels and different pyroxenes. A recent study (Jensen et al., 2009) indicates that also mica is formed already at very low temperatures, but the volume being so small that it is not detected in DSC and the phase is not distinguishable in ordinary SEM or optical microscopy. Thus the crystallization temperature (T_c) determined by DSC is the onset temperature of the main phase crystallization i.e. of the pyroxene. The composition of the glass determines what kind of pyroxene will crystallize and at which temperature it happens.

First, the liquidus temperatures are determined with a model based on Nathan and Van Kirk's model where the liquidus temperatures of possible occurring minerals are taken into account (Nathan and Van Kirk, 1978). But these do not seem to fit

	Mg-series				Al-series			Na-series	
No.	1	**2**	3	4	5	6	7	8	9
SiO_2	47.82	**44.49**	41.95	39.11	43.39	42.71	41.93	43.12	42.32
Na_2O	1.58	**1.43**	1.40	1.37	1.46	1.46	1.48	3.89	5.74
K_2O	0.69	**0.67**	0.59	0.58	0.62	0.62	0.63	0.67	0.67
MgO	8.12	**14.54**	19.70	24.96	13.99	14.01	13.98	14.22	14.07
CaO	24.86	**23.10**	21.65	20.19	22.49	22.07	21.70	22.65	22.11
Al_2O_3	11.63	**10.90**	10.20	9.50	13.32	14.55	15.66	10.46	10.16
Fe_2O_3	1.20	**1.11**	1.03	0.98	1.08	1.04	1.05	1.14	1.11
FeO	3.61	**3.32**	3.09	2.93	3.24	3.13	3.17	3.43	3.34
TiO_2	0.25	**0.21**	0.21	0.20	0.22	0.22	0.22	0.24	0.24
P_2O_5	0.23	**0.22**	0.17	0.17	0.18	0.18	0.18	0.18	0.22
NBO/T	0.66	**0.85**	1.03	1.24	0.71	0.65	0.60	0.95	1.00
ρ	2.83	**2.87**	2.90	2.92	2.86	2.86	2.85	2.86	2.84

Table 3.1: Chemical composition in mol% of the studied basaltic glasses as measured by XRF. Measured density and the calculated NBO/T ratio for each glass are also given. Glass number 2 is used as the base glass where Al_2O_3 and Na_2O are added. So the Mg-series includes glasses 1-4, the Al-series glasses 2, 5, 6, and 7 and the Na-series glasses 2, 8 and 9.

Specific temperatures						Avramov parameters		
Glass	T_g [°C]	T_c [°C]	$T_{liq,\mathrm{main}}$	$T_{liq,\mathrm{fin}}$	T_{liq} [°C]	$\log\eta_\infty$	T_g [K]	α
1	683	1000	1220	1280	1238*	-1.78	956	3.29
2	685	1021	1232	-	1267*	-1.71	958	3.57
3	683	1006	1230	1295	1320*	-2.11	956	3.46
4	685	980	1217	1355	1374*	-2.11	958	3.53
5	689	978	1217	1270	1274*	-2.17	962	3.21
6	692	1000	1220	1295	1295*	-2.32	965	3.14
7	695	1012	1215	1305	1313*	-3.02	968	2.76
8	660	973	1200	-	1266*	-1.89	933	3.32
9	643	944	1160	1210	1256*	-1.63	916	3.44

Table 3.2: Specific temperatures of the glasses, T_g, T_c, $T_{liq,\mathrm{main}}$, $T_{liq,\mathrm{fin}}$ are measured by DSC. T_{liq} is a modeled liquidus temperature (marked with *) where the model is based on composition and the minerals that are contained in it according to Bottinga and Weill (1972). The viscosity curves of the melts are given by the Avramov parameters that are gained from fitting the data to equation 3.11.

with the T_c obtained by DSC measurements. Measurement of T_{liq} revealed how the melting proceeds in each glass and from that information further conclusions on the crystal structure and the preceding crystallization can be made. All the glasses show a well defined sharp melting peak that starts immediately after or already during the crystallization, the offset of this peak will be termed $T_{liq,\mathrm{main}}$. But most of the compositions have a following weak endotherm at higher temperatures, indicating that there exists a small volume fraction of another crystalline phase that has a higher liquidus temperature. The offset temperature of the final melting endotherm is given as $T_{liq,\mathrm{fin}}$. Generally, the $T_{liq,\mathrm{main}}$ should follow the trends observed in T_c as both are signals of the main crystalline phase.

The melting of the samples has one dominant main peak, followed by a weak peak at higher temperatures. These are denoted $T_{liq,\mathrm{main}}$ and $T_{liq,\mathrm{fin}}$ in Table 3.2. Thus in these samples there is a second phase that requires higher temperature to melt. Two samples (glass 2 and 8) have only 1 peak, but the lack of a second peak, i.e. a high temperature phase, causes the main peak to be at a higher temperature. The melting peaks of the glasses are shown in Figure 3.1, where the main and secondary melting peaks of the glasses can be seen. The liquidus temperatures of the melts are also modeled by the Bottinga and Weill model, these values are marked with * in Table 3.2. The model seems to overshoot the real liquidus temperatures especially in the Na-series. It seems to match best in the Al-series. The model should generate the equivalent to $T_{liq,\mathrm{fin}}$, the

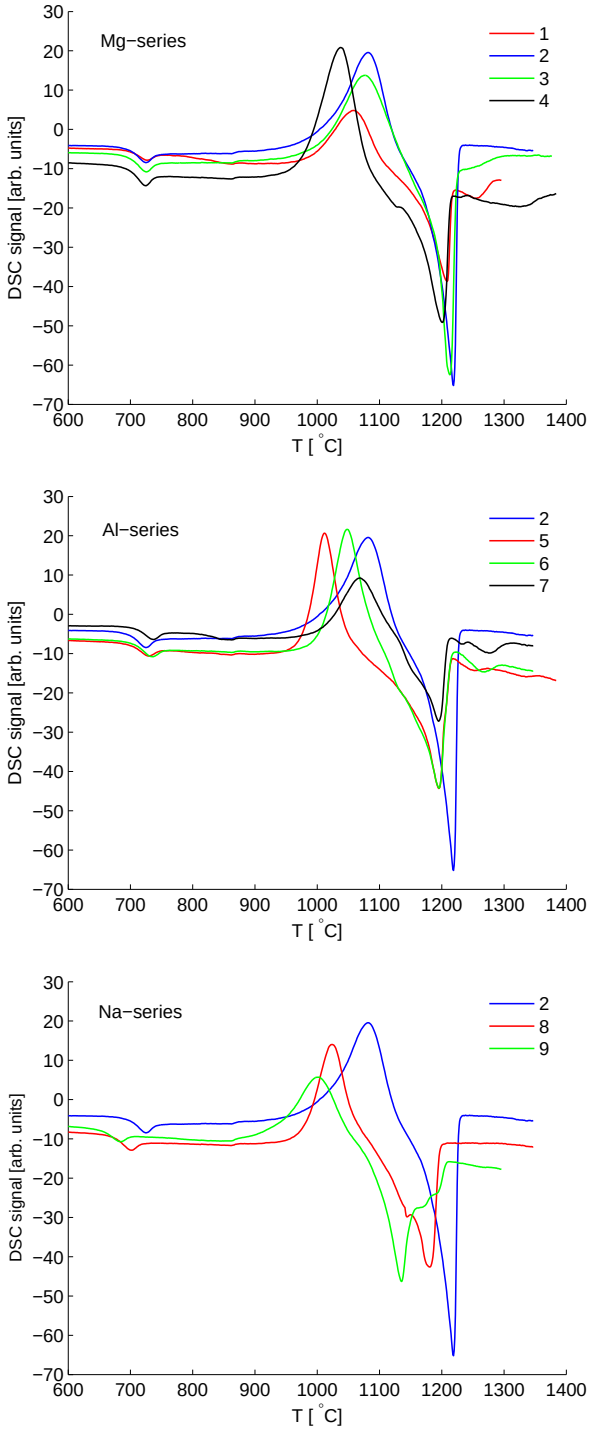

Figure 3.1: DSC-heating curves of all the glass series in the range of the melting temperatures of the glasses.

temperature where the last crystals melt, but as noted here it (most often) gives the general trends in the changes of T_{liq}, but the absolute values are not to be trusted.

In Solvang et al. (2004) is noted a pronounced change in T_g when MgO is substituted for CaO. In the Mg-series of this study there is added MgO and thus the ratio of CaO to MgO reduces accordingly, but in the Mg-series the T_g remains constant and seems not to be affected by the MgO addition.

3.2 Mechanical properties

Hardness, fracture toughness and brittleness of the glass compositions are determined by Vickers micro indentation measurements as described in sections 1.3 and 1.4. For calculation of K_c the measured values of E-modulus (Table 3.4) are used. The obtained results with standard deviations are given in Table 3.3. A general observation on iron containing alkalisilicate glasses made by Burkhard (1998) is that increase in network modifiers decreases hardness and addition of iron increases it. The effect of increase in modifiers is seen in the Na-series of this study, but for the Mg-series this can not be concluded as addition of MgO increases H. This is related to the bonding of the divalent Mg^{2+}-ion as the R^{2+} ions are more tightly bound at their sites and are less mobile than the R^+ ions that are bound to their sites by only one NBO. Increasing iron in the oxidized state (Fe^{3+}) has the same effect as increasing Al_2O_3. Both will substitute as a network formers as these glasses have a large enough amount of modifiers for charge compensation. They are tetrahedrally coordinated and thus increase the polymerization of the network. The general network structure will not change dramatically by the addition of Al_2O_3, so the increase in Al-tetrahedra in between the Si-tetrahedra has only a moderate effect on hardness.

The elastic wave velocities in the glasses were measured using ultrasound wavelengths. Knowing the wavelength and the distance the wave travels in the material the longitudinal and transverse wave velocities (v_l, v_t) can be calculated. With density (Table 3.1) and the wave velocities shear modulus (G), bulk modulus (K), Young's modulus (E) and Poisson's ratio (ν) can be calculated with the following equations.

$$G = v_t^2 \rho \tag{3.1}$$

$$K = v_l^2 \rho - 4/3 v_t^2 \rho \tag{3.2}$$

$$E = \frac{9KG}{3K + G} \tag{3.3}$$

$$\nu = \frac{1}{2}\Big(1 - \frac{1}{(v_l/v_t)^2 - 1}\Big) = \frac{3K - 2G}{2(3K + G)} \tag{3.4}$$

The measured wave velocities and the calculated values for all the glasses are given in Table 3.4. The wave velocities measured here as well as the values of modulus's are

Glass	H_V[GPa]	stdev(H_V)	K_c[MPa $m^{1/2}$]	stdev(K_c)	B[$\mu m^{-1/2}$]
1	6.83	0.16	0.30	0.01	8.0
2	7.14	0.04	0.30	0.02	8.2
3	7.29	0.18	0.31	0.03	8.0
4	7.25	0.09	0.32	0.01	8.0
5	7.18	0.08	0.31	0.02	7.9
6	7.08	0.10	0.34	0.02	7.3
7	7.19	0.09	0.34	0.03	7.4
8	6.90	0.11	0.31	0.03	7.8
9	6.76	0.15	0.31	0.02	7.7

Table 3.3: Mechanical properties of the glasses measured by Vickers micro indentation. Hardness (H) values are based on the indentations made with a load of 1.96 N, and fracture toughness (K_c) is based on measurements with the highest, 4.91 N, load.

in the same range as obtained by Schilling et al. (2003) in a study on several basaltic melts and their elastic properties as a function of temperature. The room temperature values that they obtain for diopside are v_l = 6708 m/s, v_s = 3736 m/s, G=39.9 GPa, K=75.4 GPa, E=101.8 GPa and ν=0.2750, which are in the same range as the values obtained in this work. Increase in network polymerization also increases E-modulus. This is noticed in the Al-series where a higher concentration of Al_2O_3 increases E-modulus, which is also found by Bansal and Doremus (1986). The largest changes in E-modulus are observed in the Mg-series with increasing content of MgO, while this addition also causes a very large increase in density. There exists several attempts on relating hardness and elastic modulus to the network structure via the composition as the ratio Al_2O_3/Na_2O (Yoshida et al., 2004) in sodium aluminosilicate glasses) or the SiO_2 content (Deriano et al. (2004); Lin and Liu (2006) in a wide range of glasses. The correlation between SiO_2 concentration and H and E for the basalt glasses studied in this work is shown in Figure 3.2. Actually only the two glasses with Na_2O additions fall outside the others, for both H and E values.

Poisson's ratio has also been found to be an indication on the structure of a glass; it can be correlated with densification ratio during indentation (Yoshida et al., 2005) and with atomic packing density and network dimensionality (Rouxel, 2006). With these basaltic glasses found that ν has the same tendencies as hardness and elastic modulus, which can be counted to reflect densification (to a certain limit) and network structure respectively. This is shown in Figure 3.3, where it seems to be a slight correlation that with increasing Poisson's both hardness and elastic modulus increase.

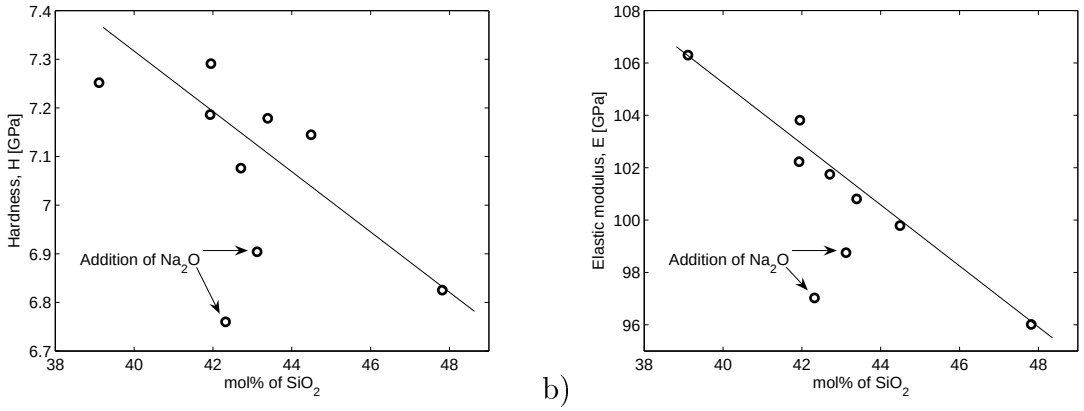

a) b)

Figure 3.2: a) Hardness and b) elastic modulus of all the glasses as a function of the SiO_2 content given in molar %. The glasses in the Na-series are marked. The line is given for a guide to the eye.

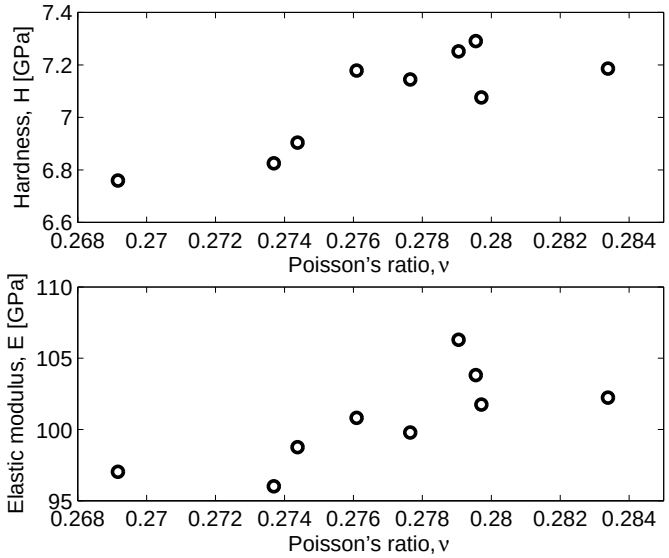

Figure 3.3: Hardness and elastic modulus of the glasses as a function of the Poisson's ratio.

Glass	v_t [m/s]	v_l [m/s]	G [GPa]	K [GPa]	E [GPa]	ν
1	3650	6540	37.69	70.71	96.01	0.274
2	3690	6650	39.05	74.80	99.79	0.278
3	3740	6760	40.57	78.49	103.81	0.280
4	3770	6810	41.55	80.18	106.30	0.279
5	3720	6680	39.50	75.04	100.81	0.276
6	3730	6750	39.75	76.98	101.75	0.280
7	3740	6800	39.83	78.66	102.23	0.284
8	3680	6600	38.75	72.95	98.75	0.274
9	3670	6530	38.22	70.06	97.03	0.269

Table 3.4: Results of the ultrasound velocity measurements and parameters G, K, E and ν derived from the transversal and longitudinal velocities.

3.3 Viscosity

Viscosity is a reflection of the melt structure and depends on the short range order (local bonds) and on the medium range order (clusters, etc.). For glasses viscosity is usually measured at temperatures from T_g and up, if the glass does not crystallize. Generally viscosity is measured by penetration or parallel-compression methods at the low end of temperatures around T_g and at high temperatures above T_c in the melt viscosity is measured by rotational rheometry. In this work high temperature viscosity is measured by rotational rheometry starting at 1500 °C and stepping down with 25 °C increments until the glass crystallizes. The simplest way to model the temperature-viscosity relationship is by an Arrhenian equation

$$\eta = \eta_\infty \exp(E/RT), \tag{3.5}$$

where E is an activation energy for the viscous flow, R the gas constant and η_∞ a constant denoting the high temperature limit of viscosity. However, most liquids do not follow this Arrhenian behavior and do not show linear dependency between $\log \eta$ and $1/T$, meaning that the activation energy is temperature dependent.

Several other models have been developed to take into account the non-linearity of viscosity. One of them is the model by Avramov and Milchev (1988); Avramov (1998, 2005), which has been used in this study. The Avramov and Milchev model has two assumptions; firstly viscosity is inversely proportional to the average jump frequency of individual building units (molecules)

$$\eta = K/\langle \nu \rangle, \tag{3.6}$$

where K is a constant and secondly that the individual molecules jump frequency is

$$\nu(E) = \nu_0 \exp(-E/RT) \tag{3.7}$$

where E is the particular activation energy. The average jump frequency can be solved for any distribution function of the activation energies. Assuming that the low energy part follows a Poisson's distribution gives

$$\langle \nu \rangle = \nu_0 \exp\Big(-\frac{E_{max}}{\sigma}\Big). \tag{3.8}$$

The dispersion of the system (σ) is a function of entropy (S)

$$\sigma = \sigma_r \exp\Big(-\frac{2(S - S_r)}{ZR}\Big), \tag{3.9}$$

where the r denotes the reference state and Z is a constant denoting the degeneracy of the system. By combining equations (3.6) to (3.9) and using T_g as the reference state and remembering that above T_g entropy can be described as $S = S_g + C_p \ln(T/T_g)$, the temperature dependence of η can be described as

$$\eta = \eta_\infty \exp\Big[\epsilon\Big(\frac{T_r}{T}\Big)^\alpha\Big], \tag{3.10}$$

where $\epsilon = E_{max}/\sigma_g$, $\alpha = 2C_p/ZR$ and η_∞ is the high temperature viscosity. The parameter α can be used as a fragility index determining how far away a melt is from Arrhenian behavior Angell (1995). $\alpha = 1$ is a strong Arrhenian liquid and the melt is more fragile with increasing α. This can be reformulated (Yue, 2008; Solvang et al., 2004; **?**) to

$$\log \eta = A + (12 - A)\Big(\frac{T_g}{T}\Big)^\alpha. \tag{3.11}$$

where $A = \log \eta_\infty$. From equation (3.11) it is seen that $\log \eta = 12$ when $T = T_g$, which has been verified for oxide glasses (Yue, 2008; Yue et al., 2004b,a). By using the measured high temperature viscosities (see Table 3.5) and the DSC defined temperature for $\eta(T_g) = 10^{12}$ Pa s, the entire viscosity curve can be predicted with equation (3.11) by optimizing the parameters. These parameters are given in Table 3.2. The fragility indexes of all the glasses as function of molar % oxide of the additive oxide are shown in Figure 3.4. For discussion of the results see article IV.

It is worth to notice glass 4. It behaves rather different from the other compositions, it has a very high crystallization temperature, thus its viscosity measurements were started at 1000 K higher temperature to get more measurement points for a better fit of equation (3.11). At the two highest temperature points the viscosity is so low and thus the rotator speed so high and torques so low that the instrument accuracy is not high enough to measure these points and thus the two points were discarded.

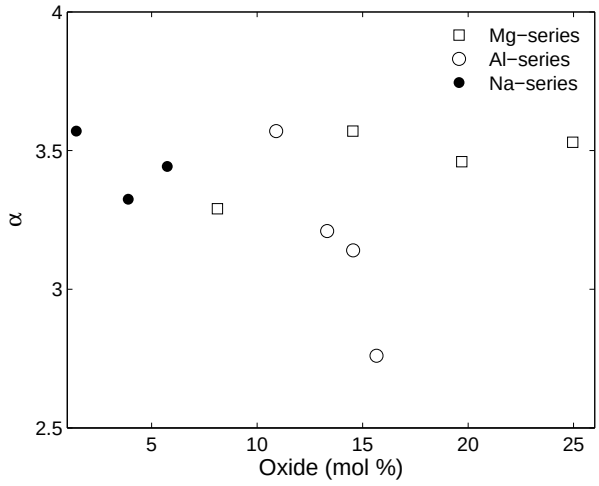

Figure 3.4: The fragility index (α) of all the glasses, with x-axis showing the amount of oxide either MgO, Al_2O_3 or Na_2O, i.e. in Mg-series the amount of MgO.

	Mg-series; η [Pas]				Al-series; η [Pas]			Na-series; η [Pas]	
T [K]/ glass	1	2	3	4	5	6	7	8	9
1773				0.31					
1748				0.37					
1723	1.60	0.92	0.49	0.49	1.04	1.02	1.10	0.74	0.81
1698	1.96	1.15	0.67	0.58	1.31	1.25	1.43	0.96	0.98
1673	2.55	1.46	0.89	0.72	1.63	1.61	2.00	1.22	1.22
1648	3.36	1.88	1.09	0.94	2.26	2.22	2.76	1.68	1.51
1623	4.44	2.42	1.42	1.19	3.07	3.09	3.90	2.22	1.89
1598	5.95	3.22	1.88		4.14	4.15	5.66	2.88	2.44
1573	8.11	4.33	2.52		5.68	5.78	8.15	3.89	3.17
1548	11.19	5.92	3.44		8.01	8.33	12.20	5.62	4.19
1523	15.81	8.30			11.74			7.62	5.66
1498	22.70	11.96			17.22			9.27	7.71
1473		17.47			28.37			12.92	10.81
1448		25.48						19.23	15.59
1423									21.38

Table 3.5: Measured high temperature viscosities in [Pas] of all the glasses.

Overall it can be seen that the change in viscosity in the whole temperature range before crystallization is very small compared to the other glasses.

Several works on viscosity of basaltic glasses are made, where varying compositions are fitted with one and same model. The metaluminous melts, the group in which the melts used in this study belong to, generally follow well the models at all temperatures while peralkaline and peraluminous melt diverge more (Russell and Giordano, 2005; Giordano et al., 2006). A large study on aluminosilicate melt viscosities with varying compositions is made recently (Solvang, 2002), where the NBO/T, Al_2O_3 and Ca/(Mg+Ca) are regulated.

Iron-bearing Na_2O-Al_2O_3-SiO_2 melts have been used as models for magma to determine viscosity in the range of $10^8 - 10^{14.5}$Pa s with the micropenetration technique. Depending on the composition the temperatures that are used are between 500 to 1000 °C. In this range the measured viscosities of the glasses follow an Arrhenian behavior (Webb, 2005). On the other hand Mysen (2003) shows for aluminosilicate melts that there is change in the Q^n speciation as a function of temperature in these depolymerized melts and that the aluminum distribution in the Q^n species changes also. This causes most likely non-Arrhenian temperature dependence of the viscosity. The non-Arrhenian behavior is seen in the measurements made here.

3.4 Relation to basalt wool

The obtained results on the bulk glass samples can as a first approximation be assumed to hold also for fiber glass. So increase in E-modulus implies also an increase of the hardness of the glass, which can be achieved both by increasing MgO or Al_2O_3. Of these Al_2O_3 produces a more polymerized and stable network, also increasing the crystallization and liquidus temperatures. Addition of Na_2O would produce the least brittle fibers within this group, but they would also have considerably lower crystallization and melting temperatures, reducing the high temperature tolerance of the product.

In general all the basalt glasses are very dense and brittle, and only a large increase in Na_2O changes this a little. With the basaltic composition we are far away from the optimal 'low-brittleness' glasses (Sehgal and Ito, 1999), thus effectively no change in composition can bring basalt close to a low-brittleness glass.

3.5 Further work

Within such a study several other elements could be varied. Due to limited time only 9 compositions were studied, where the varied oxides were chosen such that they could

give significant information with respect to fiber production. Of the oxides, magnesia is related to the spinnability of the melt, alumina to the bio-solubility of the fibers and sodium oxide is a general flux that can be used to reduce the melting and crystallization temperatures. Other oxides that could be tested are calcium oxide and iron oxide, the former is also related to the spinnability of a melt and the later is very abundant in natural raw materials.

Within this study a few other issues on the glasses would be of importance to know. Firstly the iron oxidation state of each glass. This would give information on how the chemical composition affects the oxidation of the melts, since all the glasses have a similar thermal/melting history. Secondly, as all the glasses have various crystallization and liquidus temperatures, it would be of interest to identify the crystallizing phases in each glass. Also to see how the phase distributions change with the chemical substitutions. As the main liquidus peak for several of the glasses is at about 1220°C, it is probable that the main phase of the glasses is same in these glasses, but the other phases should be different.

Chapter 4

Crystallization

In a crystalline material atoms are situated in a periodic or repeating array over large atomic distances, i.e. there exists long range order. During solidification the atoms will take position in a repetitive three-dimensional pattern where each atom is bonded to its nearest neighbor atoms. All metals, ceramics and some polymers form a crystalline structure during normal solidification conditions. In a metal bonded by metallic bonds and in ceramics by ionic bonds. Whether a liquid crystallizes depends on its ease at which atoms in the random liquid structure can transform to an ordered state during solidification. Generally a complex structure is more prone not to become ordered, as well as a rapid cooling through the solidification temperature favors the formation of a non-crystalline solid, a glass. Crystallization is a crucial issue when considering glass-forming ability and fibrization process of basaltic melts. In this chapter a brief introduction to crystallization in general will be given and a detailed discussion on specific topics in basalt crystallization.

4.1 Nucleation and growth

4.1.1 General aspects

Crystallization of a material is a combination of nucleation and crystal growth. There has to exist nucleus from which the crystals can grow, either in the melt or in the glass, depending on which direction from high or low temperatures the crystallization process is approached. If no nucleus exist in the melt it will turn into glass during cooling.

A Time-Temperature-Transformation diagram (TTT-diagram) describes how nucleation and growth can be expected to behave with time or temperature (Figure 4.1). From the figure it is evident that just below the melting temperature the time required to form crystals is long. Approaching T_m the time required to form nuclei and crystals

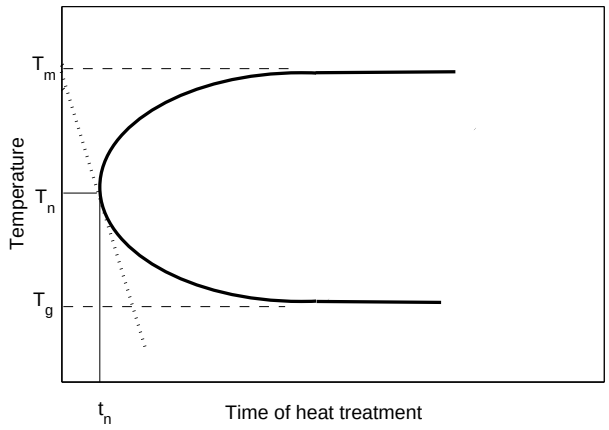

Figure 4.1: A general TTT- diagram, that shows the dependence between crystal growth, time and temperature. T_m denotes the melt temperature where crystallization (and nucleation) approach zero in the high temperature limit, T_g denotes the glass transition temperature where nucleation (and crystallization) approach zero i.e. requires infinite times and T_n is the temperature where shortest time (t_n) for crystallization is required.

will be infinite. By lowering the temperature the required time becomes shorter, until a certain temperature T_n where a minimum in time (t_n) is found where the crystal formation has a maximum. At temperatures lower than this the crystal formation requires again longer times, until the temperature reaches T_g where no crystallization occurs, or the time needed is infinite. The form of the curve results from the competition between the kinetic and the thermodynamic factors. This will be described in more detail in the following paragraphs. At T_n the conditions are least favorable for formation of glass, and most favorable for crystallization. A similar time-temperature diagram is valid for nucleation; it is just shifted to lower temperatures and somewhat shorter times.

Similar type of diagrams with T-T-M where M is a materials parameter depending on the crystallization degree can also be produced. For example, an image showing hardness, density or fracture toughness with respect to heat treatment time and temperature is a valuable tool for designing glass ceramics. Such TTM dependencies have been determined on glass ceramics produced of fly ash, which is a major waste material from power plants (Kim and Kim, 2005).

Nucleation

For a material to crystallize there has to be nucleus present in the melt. The nucleation can be either homogeneous i.e. they will form spontaneously from the melt or heterogeneous where nucleus will be formed on pre-existing surfaces as impurities in the melt or crucible walls.

Classical nucleation theory addresses homogeneous nucleation where there is an equal probability for a nucleus to form anywhere in the melt. In the calculation of nucleation rate it is assumed that the nucleus formed are spherical, and that two barriers for the formation exists. The thermodynamic barrier, which involves the free energy change within the system when the nucleus is formed. Secondly the kinetic barrier, which is related to the movement and rearrangement of mass to form a ordered structure/particle from the disordered liquid. The process is described by

$$I = Ae^{-\frac{W^* + \Delta G_D}{kT}} \tag{4.1}$$

where A is a constant, W^* is the thermodynamic barrier, and more precisely the work required to form a nucleus of critical size i.e. one that will not re-dissolve into the melt, ΔG_D is the kinetic free energy barrier, k is the Boltzmann's constant and T the absolute temperature. The thermodynamic barrier involves two changes, first the arrangement of atoms into a crystalline structure will lower the volume free energy as the free energy of a crystalline state is lower than that of a melt. Secondly this is counteracted by the increase in surface energy, as it will increase due to the formation of new surface between the the regions of different structure. The kinetic barrier is related to the effective diffusion coefficient of the material by

$$D = \frac{kT\lambda^2}{h} \quad e^{\frac{-\Delta G_D}{kT}}, \tag{4.2}$$

where λ is the atomic jumps distance and h Planck's constant. And on the other hand the diffusion coefficient D can be expressed by the viscosity η of the melt via the Stokes-Einstein relation

$$D = \frac{kT}{3\pi\lambda\eta}. \tag{4.3}$$

These can be substituted into Eq 4.1 to eliminate ΔG_D

$$I = \frac{Ah}{3\pi\lambda^3\eta} \quad e^{-\frac{W^*}{kT}}. \tag{4.4}$$

For the heterogeneous nucleation similar expressions can be used by changing some parameters

$$I_{het} = A_{het}e^{-\frac{W^*_{het} + \Delta G_D}{kT}}, \tag{4.5}$$

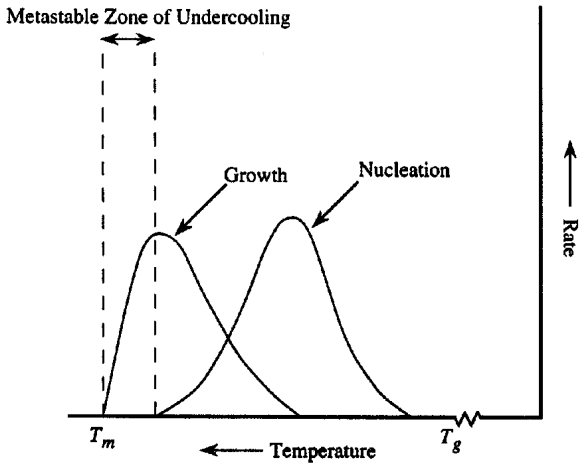

Figure 4.2: Nucleation and crystallization rates as a function of temperature. The rates are bounded by T_m from above and T_g from below.

where the subscript *het* refers to heterogeneous nucleation. The nucleation rate expressions can be used to predict the shape of the nucleation curve, I, as a function of temperature. An example of a nucleation curve is shown in figure 4.2. When the temperature is lowered below T_m, the change in free energy can allow nucleus to form, but when the temperature is very close to T_m ΔG_D is very small, causing the critical radius of a nuclei to be very large. As the probability that such a nucleus would occur is small, there is a metastable zone of under-cooling with no nucleation. At temperatures below this zone, the critical radius of a stable nucleus is sufficiently small that the probability of formation of a nucleus large enough is significant. Below the metastable zone the thermodynamic barrier decreases with decreasing temperature and the nucleation rate will increase correspondingly. But lowering the temperature causes increase of the viscosity, and this will quickly increase the kinetic barrier. The higher kinetic barrier decreases the rate of nucleation until there is essentially no nucleation. The zone of under-cooling varies depending on the material investigated.

Crystal growth

Crystal growth rate, U, can be expressed by two limiting forces just as the nucleation ΔE the kinetic barrier and ΔG the thermodynamic barrier.

$$U = a_0 \nu e^{\frac{-\Delta E}{kT}} \left(1 - e^{\frac{\Delta G}{kT}}\right), \tag{4.6}$$

where a_0 is the inter-atomic separation distance and ν the vibrational frequency. For the kinetic barrier the same diffusion equations as for nucleation (eq 4.2 and 4.3) can

be used. Then the crystal growth rate is given by

$$U = \left(\frac{kT}{3\pi a_0^2 \eta}\right)\left(1 - e^{\frac{\Delta G}{kT}}\right). \tag{4.7}$$

The rate of crystal growth is depicted in figure 4.2 and it is very similar to nucleation rate, as is evident from the equations 4.4 and 4.7. Crystal growth is not limited by any metastable zone of under-cooling, but as soon as $T < T_m$ growth can occur if there is nucleus present. The nuclei can have formed earlier, and the structure or composition of them can be different from the growing crystal phase. This is often true for heterogeneous nucleation. In melts that have a low viscosity, the crystal growth rate is determined by thermodynamic parameters, and it will be high. As the temperature decreases the growth rate will decrease due to the increasing viscosity until it reaches zero.

4.1.2 Crystallization of basaltic melts and glasses

As mentioned earlier basalts have a strong tendency to crystallize. The cooling of the melt has to be rapid enough to avoid the crystallization. Vice versa when the glass is heated it starts to crystallize at temperatures at or somewhat above the glass transition range. The temperature range where an under cooled basalt melt exists is narrow.

The composition of basalts that have been used in crystallization studies in literature varies considerably due to the large natural variation in the rock compositions. But some common conclusions can be drawn from them. The phase that usually nucleates from the melt is spinel, some times more specifically defined as magnetite, titanomagnetite or hematite. Some crystal growth of these phases is observed but generally spinel functions as a nucleating agent for pyroxenes that are the main phase to crystallize (Tošić et al., 1998; Bouhifd et al., 2004; Lubas et al., 2005). The pyroxene is often of the augite type. This has been confirmed by XRD or ^{27}Al MAS NMR measurements. In DSC scans upon heating a basalt, two or more crystallization peaks are often seen indicating more than one crystalline phase. If the crystallization temperatures are well separated it indicates that spinel is the lower one and that it grows to detectable sizes (Burkhard, 2001), while overlapping crystallization temperatures are related to different pyroxenes, as has been determined by XRD measurements where phases as augite [(CaFeMg)SiO_3], diopside [$Ca(Mg_{0.16}Fe_{0.85})(SiO_3)_2$] and aluminian-diopside [Ca(Mg,Al)(Si,Al)$_2O_6$] are observed (Yilmaz et al., 2006). By ^{27}Al MAS NMR, the crystal phase has been determined to be augite. It is also observed that before crystallization the Al-arrangement in the glass is nearly similar to the arrangement after crystallization. From this it is concluded that the short range order in the glass is close to augite type (Lubas et al., 2005).

	SiO_2	Al_2O_3	TiO_2	FeO	CaO	MgO	K_2O	Na_2O	P_2O_5	SO_3
Fiber 1	44.2	11.4	0.6	6.6	18.5	15.5	0.9	2.1	0.1	0.2
Fiber 2	43.5	11.1	0.5	5.6	18.4	17.5	0.9	2.2	0.1	0.2

Table 4.1: Composition of the studied basalt wool fibers (in mol%). The chemical compositions were analyzed using a X-ray fluorescence spectrometer (Philips 1404), with an error of less than 0.1wt%.

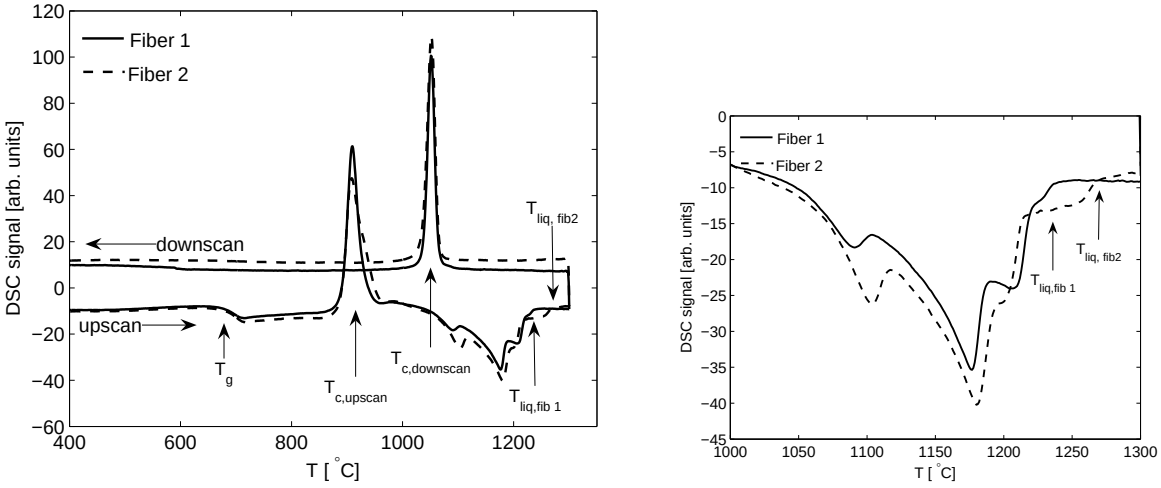

Figure 4.3: DSC up- and downscans of basalt glasses 1 and 2. In the figure are marked T_g, T_c and T_{liq}. On the right a close up view of the melting peaks of the two glasses, with the difference in the liquidus temperatures shown with arrows.

The oxidation state of iron Fe^{2+}/Fe^{3+} has considerable effect on the crystallization, thus also the atmosphere where the phase transition occurs. An increase in Fe^{3+} increases the nucleation rate i.e. the formation of spinel and this further increases the crystal growth rate.

4.2 A case study

Two chemically very similar basalts (compositions in Table 4.1) are discussed in articles I and II. Their glass transition temperatures are 676°C and 680°C, crystallization temperatures at 900°C for both and the liquidus temperatures i.e the temperature where all the crystals are molten are 1235°C and 1270°C for Fiber 1 and 2 respectively. These temperatures are measured by differential scanning calorimetry (DSC) with a heating rate of 20 °C/min. The DSC upscan curves of the glasses and the following downscan curves are shown in Figure 4.3 with the discussed temperatures.

The crystal phases of the samples were determined by XRD. The main phase in

all samples was pyroxene of augite and/or diopside type. Difference between the two structures could not be determined due to their similar XRD spectra. Further there was found some spinel structure. Both these findings agree well with what is generally observed in basalts. Spinel is the phase that nucleates and grows first and acts further as a nucleation base for the pyroxene which will then form the main crystalline phase.

4.2.1 Effect of the surrounding atmosphere on crystallization

The fibers were produced under reducing conditions, so all iron is in Fe^{2+} oxidation state. All following heating of the samples was made inside the DSC, where the atmosphere was controlled, either as ambient air or inert argon. XRD spectra showed spinel structure for the samples molten and crystallized in air atmosphere in the DSC. In these samples almost all iron is oxidized into Fe^{3+}, whereas the samples measured in argon only have 20% of Fe^{3+}. The abundance of Fe^{3+} is favorable for the nucleation of spinel. The presence of nuclei allows crystal growth to occur as soon as the temperature limit is passed. Thus the beginning of the main phase crystallization is at the same temperature independent of scan number and almost independent of maximum temperature (see Figure 1 of article II). It can be confirmed that spinel nucleated at higher temperatures and that the presence of spinel is a catalyst for the crystallization of pyroxene, thus the crystallization temperature is fairly controlled.

For the inert atmosphere measurements this is not the case. The crystallization and melting temperatures of the basaltic materials shift to higher temperatures when repeated up- and downscan cycles are performed in argon atmosphere (Figure 4.4a). This indicates that there is no well defined nucleation process occurring. Instead at a fairly high degree of under cooling finally spinel and/or pyroxene will nucleate and pyroxene continues to grow. The atmosphere has a great effect on the controllability of the crystallization, as the nucleation agents are only present in the oxygen containing atmosphere.

4.2.2 Structure in the liquid above liquidus temperature

Indirectly observed structure in a basaltic liquid is discussed in articles I and II. The structural order of the liquid is observed by two phenomenons, they will be reviewed shortly in the following.

All crystalline material is molten at temperatures above T_{liq} as no further endotherm is observed in the DSC scan, so there is no crystals. But, as observed by the experiments in argon, some order of the previous crystalline structure will be conserved in the liquid. After the first heating of the glass, the liquid will need a large under cooling before it crystallizes, as no suitable nucleation agents are present. Upon

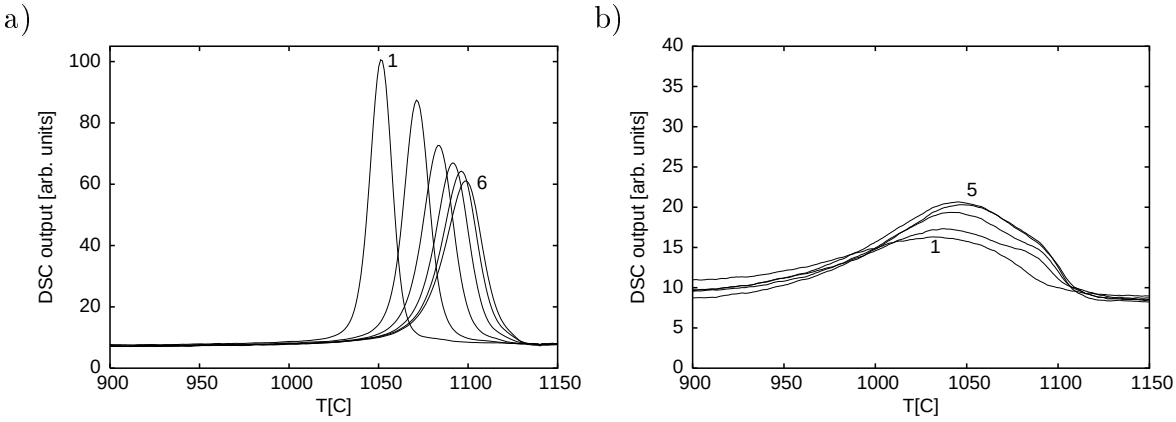

Figure 4.4: Crystallization peaks of fiber 1 with scan number indicated in the figure. The maximum temperature of the scans are a) 1300°C and b) 1400°C. Notice different scales on y-axis.

reheating, the crystalline material will melt when the temperature is high enough and when it is cooled again the crystallization will happen at a higher temperature than the first time. Some ions have kept their approximate positions of the previous crystal structure, so it is easier to start the crystallization, as the distances for the ions to reach lattice positions is shorter. This shift in the crystallization temperature to higher temperatures continues during following scans, this means that the time needed to form the 'perfect' crystal structure is not long enough during the cooling stage. Each time the crystalline structure melts, its approximate structure is kept by the melt and then during the following crystallization a more perfect structure will be achieved. As seen in figure 4.4a after several repeated scans the temperature change becomes smaller, indicating that the crystalline structure is as perfect as possible. Some fluctuation will always occur in the liquid resulting in limits on how much the order within the melt can accelerate the crystallization process.

With the basaltic composition that has T_{liq} at 1235°C (Fiber 1), the previously described crystallization peak shift to higher temperatures due to the structural order in the melt is seen when the maximum temperature of the melt is 1250, 1300 and 1350°C (i.e. T_{liq}+15, +65 and + 115°C). The shift is smallest for the highest maximum temperature. When the melt temperature is raised further to 1400°C (T_{liq} + 165°C) no shift is seen. At temperatures high enough above liquidus, the thermal energy of the ions is so large that the ions do not stay in certain positions and thus no structural order will be conserved in the liquid and the crystallization process will always start from the same random state. Similar results have been found for a bulk basaltic glass (Yue, 2004) where a sample is up-and down scanned in the DSC 21 times with a maximum temperature of T_{liq} + 70°C. This is in the temperature region where the

liquid remembers the previous crystalline structure and after 14 scans it is observed that the sample fully crystallizes. In the first scans there was always a glass phase incorporated; which though got smaller after each downscan as a larger fraction of the liquid had kept the crystalline structure and thus was able to crystallized during the downscan.

Also the crystallization process changes when the maximum temperature of the scan is raised. With maximum temperatures above but close to the liquidus temperature, the phase change from liquid to crystalline material during the downscan in a DSC shows a sharp well defined exotherm, the crystallization peak. When the maximum temperature is 150°C above T_{liq}, the crystallization is a broad process lasting over 100°C without a well defined peak temperature (Figures 4.4 a and b). This, the broad crystallization peak, indicates that the ions are far away from crystal lattice positions and need time to rearrange themselves. Further, during the next upscan a crystallization peak is observable. This indicates that not all material was able to crystallize during cooling (during the downscan) due to the high amount of disorder of the melt, but was left as glassy material, which then crystallizes upon the next heating.

The prevailability of the structure in the liquid was tested by keeping the liquid at 1300°C for 45 minutes, which is a long enough time for any process to reach equilibrium at such a high temperature. This did not change the crystallization peak to a broad peak which would result if the liquid had random structure. The peak kept the well defined shape and the following crystallization temperature was higher than the previous one. The liquid is able to keep the structural order for a prolonged time.

Further experiments

The structural order in a liquid can be observed by high temperature x-ray diffraction experiments. This kind of work has been performed on metallic glasses (Xiufang et al., 2006) and the same principles can be applied on oxide glasses. Small-angle x-ray diffraction would reveal if there is clusters that differ from the main matrix, but only if the two phases differ enough from each other. By wide-angle diffraction the inter atomic distances could be revealed, and if we have crystal-like structure this could give rise to a diffraction pattern if the total volume fraction of the crystal-like structure is large enough.

4.2.3 A peculiarity on fiber brittleness

In the beginning of this book it is mentioned that the whole project began due to a problem with an insulation fiber product. The product is produced from two different sets of raw materials, reaching in the end the same compositions, still one product is

brittle in use while the other fulfilled the strength parameters required for the product. These two fibers are the Fiber 1 and 2 discussed in this section.

When the fibers are produced from raw materials, there is a variety of crystalline phases that have to either be molten or dissolved in the melt during the residence time in the cupola furnace. The residence time is around 15 minutes at the highest temperature before the melt runs through and onto the spinner wheels. The maximum temperature of the furnace is 1500°C, but some crystalline phases, even common ones, as alumina need higher temperatures and thus they need to be dissolved in the melt. Though the main part is basalt and will be molten latest around 1300°C.

As discussed in article I, even though the basalt is in liquid state, some structural arrangement in the basaltic liquid will prevail for approximately 150°C above the liquidus temperature. As this structure within the melt can enhance the crystallization upon cooling, it functions as a nucleation agent. If volumes with structural order exist in the melt when the melt is spun to glass, these same small volumes can function as stress concentration points, as discussed in section 1.2.2, and cause the fiber to break easier under a certain load.

The liquidus temperatures for the crystallized Fiber 1 and 2 differ by 35°C with Fiber 2 requiring higher temperature to be totally molten, as is seen in Figure 4.3. And as it was Fiber 2, that was the brittle one, a possible reason for that can be concluded from this study. The temperature of the furnace with the available residence time has been high enough to melt all crystals for the composition and raw materials of Fiber 1, but for Fiber 2 this is not the case. There is no evidence that there would be crystalline remains in the glass, thus we are speaking of the domains with structural order that have survived the melting process, which then function as the weak points in the fiber.

This work suggests that the impact of remembered structural order in glass on the fiber strength is a crucial point to be considered when the fiber spinning process is designed.

Chapter 5

Nanoindentation on bulk and fiber glasses

5.1 Mechanical properties of glass by nanoindentation

Hardness and elastic modulus can be determined by nanoindentation. Measurements on wool type fiber glass and bulk glass are described in article III. The measured glass compositions are three different basalts and an E-glass with compositions shown in Table 5.1. All fiber samples are produced by the cascade spinning process (Axten et al., 1993) and fibers of all four compositions are indented. The indented bulk glasses are of Basalt Ob and E-glass composition.

	SiO_2	Al_2O_3	CaO	MgO	FeO	Na_2O	TiO_2	K_2O	P_2O_5	B_2O_3
Basalt Ob2	56.0	10.7	9.3	13.1	5.5	4.2	0.5	0.7	0.1	0.0
Basalt Ob	55.7	9.6	8.3	16.2	5.5	3.1	0.6	0.8	0.3	0.0
Basalt RW	44.8	11.5	19.0	18.0	2.6	2.3	0.6	1.0	0.1	0.0
E-glass	57.3	8.9	25.8	1.1	0.1	1.0	0.1	0.0	0.0	5.5

Table 5.1: Composition of the studied glasses in mol%. The values are determined by XRF measurements. Basalt RW in this study are the same fibers as used in the crystallization study with the label Fiber 2.

Hardness and reduced elastic modulus are measured for both bulk and fiber glasses as a function of depth by changing the indentation load and then for fibers also as a function of fiber diameter. If we assume that glass is a homogeneous material and that the production method does not cause layered structures (due to thermal, compositional, stress state etc. differences), then both hardness and elastic modulus should

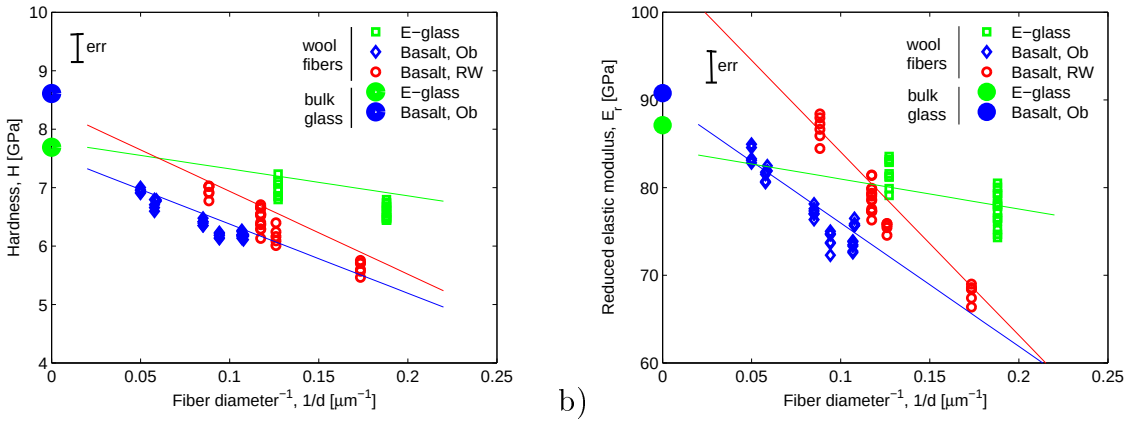

Figure 5.1: a) Hardness and b) reduced elastic modulus of all fiber compositions as a function of inverse fiber diameter. The bulk glass values for Basalt Ob and E-glass are added at d= ∞.

be constant when measuring them as a function of depth into the material. When measuring on the same fiber, H and E_r were indeed constant with depth, but when measuring on another fiber of the same composition but with a different diameter a parallel jump could be seen in H and E_r values. This jump can be explained with the diameter dependent measurements as shown in Figure 5.1, where H and E_r are depicted as inverse fiber diameter. H and E_r become larger the thicker the fiber is, but not reaching the values of bulk glass, which are shown on the y-axis. The bulk glass values are calculated as the average value of indentations deeper than 80 nm, below this depth H and E_r are constant, while in the upper layers some change is seen.

5.2 Nanoindentation - a probe on structure?

With nanoindentation the depth probed is 30 to 80 nm and the width of the indent is 0.5 to 0.8 μm, so even though we are probing depths in the nanoscale, at minimum the indent affects on the order of 4×10^9 atoms. We are thus discussing bulk properties of the glass, all information is an average over all bonds, atoms and glass structure defects within the indentation volume.

As discussed in section 2.2.1, the fictive temperature (T_f) of a glass gives the temperature at which the glass structure is frozen in. The higher T_f, the more open the structure of the glass, which Kiczenski et al. (2005) have shown by NMR spectroscopy i.e. increasing T_f the NBO content increases in the glass. In glass production this is achieved by increasing the cooling rate f. ex. by reducing the fiber diameter. The fictive temperature of continuously drawn fibers is proportional to the diameters of the fibers. Further on, the cooling rate (q_c) of the fibers can be approximated knowing the

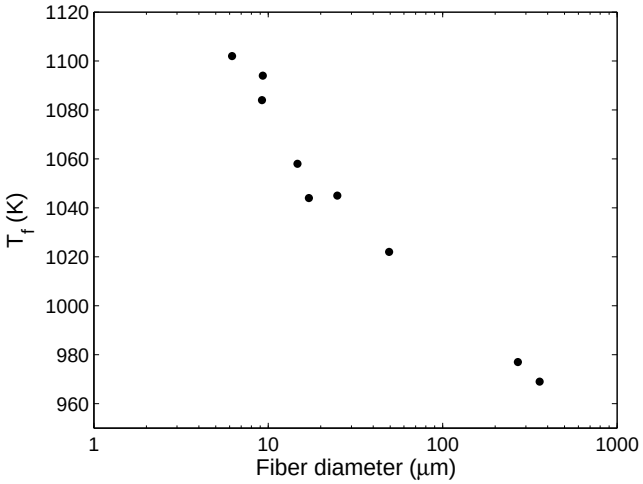

Figure 5.2: The fictive temperature (T_f) of continuous basaltic glass fibers, of composition Basalt Ob as a function of fiber diameter (Y. Z. Yue, unpublished data, 2003).

furnace temperature, die diameter, the drawing speed and the final fiber diameter (d) (Ohe von der, 2003). Thus it is possible directly to link (d), T_f and q_c, where the diameter reflects indirectly T_f via the cooling rate q. The fictive temperature of fibers can be measured with DSC by the enthalpy matching method (Moynihan et al., 1976; Yue et al., 2002). Figure 5.2 shows the fictive temperature dependence on fiber diameter for continuously drawn basalt glass fibers. It can clearly be seen that the thinner the fiber the higher T_f it has. This information can not be gained on the cascade process fibers as the fiber diameter distribution within the wool is always very large ranging from 2 μm to over 20 μm.

Increasing the temperature causes several structural modifications in a glass melt, such as cation site thermal expansion, local disorder and enhancement of motion of the ions. Glasses that could contain only Q^3 units will at higher temperatures contain also Q^2 and Q^4 units, increasing the network disorder (Henderson et al., 2006). The increase of disorder in the glass structure with increasing fictive temperature has also been observed. Within an aluminosilicate glass, cooled at normal rates, the aluminum tetrahedra is generally linked to a Si-tetrahedra, so Al-O-Si bonds are preferred, reflecting the aluminum avoidance principle described in section 2.2.2. At higher cooling rates i.e. higher fictive temperatures this ordering decreases and more Al-O-Al and Si-O-Si bonds are observed (Dubinsky and Stebbins, 2006).

In the previous section hardness and reduced elastic modulus were shown as a function of fiber diameter for the wool type fibers. Assuming that the cascade fibers also have a direct relationship between diameter and fictive temperature and that the fictive temperature is a measure of the structure in the glass, then our measurements of

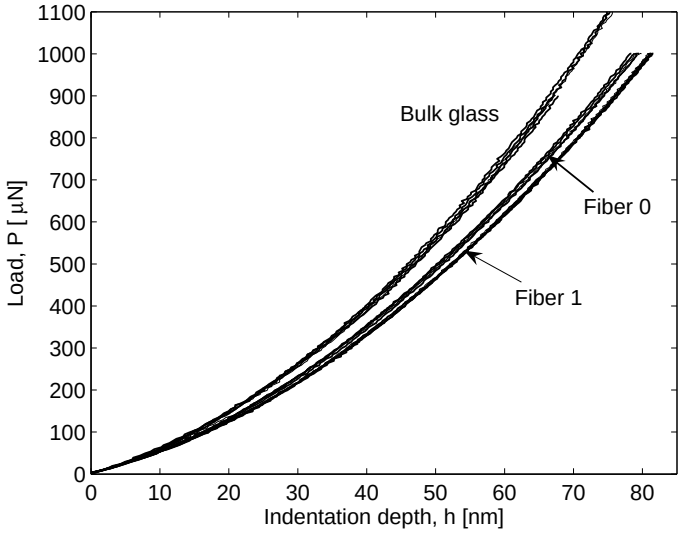

Figure 5.3: Loading curves for Basalt Ob bulk glass and two fibers with different diameters.

H and E_r can be linked to the atomistic average structure of the glass itself. Especially if looking at the difference between fiber and bulk glass, where the difference between T_f's is several hundred degrees, there the structural difference is also large. This can be seen in the upload curves of nanoindentation (Figure 5.3), as the form of an upload curve is related to the plastic and elastic deformation of the material. A considerable difference between bulk and fiber glass can be seen. The bulk glass has a more dense structure than fibers and defined from Figure 5.3 there is needed 100μN higher load to achieve an indentation depth of 60nm in the bulk glass samples compared to the fiber glass sample; that is 15% higher load.

5.3 Future ideas

It would be interesting to perform nanoindentation measurements on glass samples where the exact cooling rate is known. Both to confirm the results that we now have discovered and to get more precise information. There are several aspects to be worked on. First, the geometry issues associated when indenting fibers could be avoided with carefully prepared bulk glass samples that cover a fairly large range in cooling rates and thus fictive temperatures. This would give solid information on the relationship between the fictive temperature of the glass and the hardness and reduced elastic modulus of it. Further, the differences in the loading curves with varying T_f can be verified. Secondly, by using a new tip, the model for the loading curve observed in this study could also be verified. Third, the shape of the loading curve should be tested

with various glass compositions, to see if it still has the form $P = ah^2 + bh$ as discussed in article III. This would suggest that glasses do not behave as other materials during nanoindentation.

Chapter 6

Summary

In this work three separate topics within basaltic glasses have been covered. They all improve the existing knowledge on basaltic glass and fibers and give a basis for a better understanding of the glass when it is used in a product as insulation wool.

In the crystallization study, it is found that samples with rather similar composition can be distinguished by their endo- and exothermic responses during heating and cooling. It is further found that there exists structural order within the basaltic melt at temperatures up to 150°C above the liquidus temperature when the crystalline material is melted. This ordered structure in the melt affects the crystallization during the following cooling. The oxidation state of iron also affects the crystallization. In a reducing atmosphere iron is mainly in Fe^{2+} state, while in a oxygen rich atmosphere both Fe^{2+} and Fe^{3+} are present, their ratio depending on the melting conditions. The presence of Fe^{3+} enhances the nucleation and the following crystallization due to the formation of pyroxenes. The structural order in a melt is observed for both reduced and oxidized melts, and is thus independent of the iron oxidation state.

Changes in the chemical composition of basaltic glass induces changes in the physical properties of it, in parameters such as Young's modulus, hardness, fragility, glass transition temperature and density. Both thermal and mechanical properties are affected, and generally the observed changes can be related to changes in the network structure caused by the addition of an oxide. Addition of Al_2O_3 increases the network connectivity, the polymerization, causing generally a tougher glass, which is seen as increasing Young's modulus and T_g. The opposite of this is caused by addition of Na_2O. Na_2O is a modifier and increases the amount of non-bridging oxygen and decreases thus the polymerization and the density. The third tested oxide was the earth alkaline MgO. Additions of it increase NBO, density and the Young's modulus of the glass. It seems that the increasing NBO for the MgO substituted glasses is not causing a weaker

structure indicated by any of the measured parameters.

Nanoindentation is implemented as a testing tool for mechanical properties of thin glass fibers. It is confirmed that the method is applicable not only on coatings and bulk samples where it generally is used, but that it can also be used on fibers. Hardness and reduced elastic modulus of fibers can be determined by nanoindentation as well as their relationships to changes in fiber and glass properties. The cooling rate difference between bulk and fiber glass causes a distinct difference in the network structure of the glass. This can easily be seen in the results, where the fibers have considerably lower hardness and reduced elastic modulus. Fibers with different diameters, and thus different cooling rates, can also be distinguished by this method.

Bibliography

Angell, C. A. (1995). Formation of glasses from liquids and biopolymers. *Science*, 267:1924–1935.

Avramov, I. (1998). Viscosity of glassforming melts. *J. Non-Cryst. Solids*, 238:6–10.

Avramov, I. (2005). Viscosity in disordered media. *J. Non-Cryst. Solids*, 351:3163–3173.

Avramov, I. and Milchev, A. (1988). Effect of disorder on diffusion and viscosity in condensed systems. *J. Non-Cryst. Solids*, 104:253–260.

Axten, C. W., Bauer, J. F., Boymel, P. M., Copham, J. D., Cunningham, R. N., Kamstrup, O., Koenig, A., Konzen, J. L., Ohberg, I., Roe, C., Sacks, J., Singh, T. M., and Wolf, W. (1993). Man-made vitreous fibers: Nomenclature, chemistry and physical properties. Nomenclature Committee of TIMA Inc.

Bansal and Doremus, R. H. (1986). *Handbook of glass properties.* Academic Press.

Bartenev, G. M. (1970). *The structure and mechanical properties of inorganic glasses.* Wolter-Noordhoff Publishing Groningen, The Netherlands.

Bottinga, Y. and Weill, D. F. (1972). The viscosity of magmatic silicate liquids: A model for calculation. *Am. J. Sci.*, 272:438–475.

Bouhifd, M. A., Richet, P., Besson, P., Roskosz, M., and Ingrin, J. (2004). Redox state, microstructure and viscosity of a partially crystallized basalt melt. *Earth and Planetary Sci. Lett.*, 218:31–44.

Bückle, H. (1965). *Mikrohärteprüfung und ihre Andwendung.* Berliner Union Verlag, Stuttgart.

Burkhard, D. J. M. (1998). Microhardness of alkali silicate glasses with iron. *Phys. Chem. Glasses*, 39(1):1–3.

Burkhard, D. J. M. (2001). Crystallization and oxidation og Kilauea basalt glass: Processes during reheating experiments. *Journal of Petrology*, 42(3):507–527.

Conradt, R. (2004). Chemical structure, medium range order, and crystalline reference state of multicomponent oxida liquids and glasses. *J. Non-Cryst. Solids*, 345&346:16–23.

Deriano, S., Rouxel, T., LeFloch, M., and Beuneu, B. (2004). Structure and mechanical porperties of alkali-alkaline earth-silicate glasses. *Phys. Chem. Glasses*, 45(1):37–44.

Dubinsky, E. V. and Stebbins, J. F. (2006). Quench rate and temperature effects on framework ordering in aluminosilicate melts. *Am. Mineralogist*, 91:753–761.

Fischer-Cripps, A. C. (2004). *Nanoindentation*. Mechanical Engineering Series. Springer, 2 edition.

Gao, F., He, J., Wu, E., Liu, S., Yu, D., Li, D., Zhang, S., and Tian, Y. (2003). Hardness of covalent crystals. *Phys. Rev. Lett.*, 91(1).

Giordano, D., Mangiacapra, A., Potuzak, M., Russel, J. K., Romano, C., Dingwell, D. B., and Muro, A. D. (2006). An expanded non-Arrhenian model for silicate melt viscosity: A treatment for metaluminous, peraluminous and peralkaline liquids. *Chemical Geology*, 229:42–56.

Griffith, A. A. (1921). The phenomena of rupture and flow in solids. *Philos. Trans. Roy. Soc.*, A 221:163–198.

Hainsworth, S. V., Chandler, H. W., and Page, T. F. (1996). Analysis of nanoindentation load-displacement loading curves. *J. Mater. Res.*, 11(8):1987–1995.

Henderson, G. S., Calas, G., and Stebbins, J. F. (2006). The structure of silicate glasses and melts. *Elements*, 2:269–273.

Ito, S. (2002). Lightweight glasses require studies of brittleness properties. *The Glass-researcher*, 11(2):12–13.

Ito, S. (2004). Structural study on mechanical behavior of glass. *J. Ceram. Soc. Japan*, 112(9):477–485.

Jensen, M., Smedsjkaer, M. M., Estrup, M., Kristjansson, M., Lonnroth, N., and Yue, Y. Z. (2009). Hardness of basaltic glass-ceramics. *Eur. J. Glass Sci. Technol. A*, 50(4).

Kese, K. O., Li, Z. C., and Bergman, B. (2004). Influence of residual stresses on elastic modulus and hadness of soda-lime glass measured by nanoindentation. *J. Mater. Res.*, 19(10):3109–3119.

Kiczenski, T. J., Du, L.-S., and Stebbins, J. (2005). The effect of fictive temperature on the structure of e-glass: A high resolution, multinuclear NMR study. *J. Non-Cryst. Solids*, 351:3571–3578.

Kiczenski, T. J. and Stebbins, J. (2006). The development of a rapid quenching device for the study of the dependence of glass structure on fictive temperature. *Rev. Sci. Instruments*, 77:013901.

Kim, J. M. and Kim, H. S. (2005). Temperature-Time-Mechanical properties of glass-ceramics produced from coal fly ash. *J. Am. Ceram. Soc.*, 88(5):1227–1232.

Kurkjian, C. R., Gupta, P. K., Brow, R. K., and Lower, N. (2003). The intrinsic strength and fatigue of oxide glasses. *J. Non-Cryst. Solids*, 316:114–124.

Kurkjian, C. R. and Kammlott, G. W. (1995). Indentation behavior of soda-lime silica glass, fused silica, and single-crystal quartz at liquid nitrogen temperature. *J. Am. Ceram. Soc.*, 78(3):737–744.

Lawn, B. R. (2004). Fracture and deformation in brittle solids; A perspektive on the issue of scale. *J. Mater. Res.*, 19(1):22–29.

Lawn, B. R. and Marshall, D. B. (1979). Hardness, toughness and brittleness: An indentation analysis. *J. Am. Ceram. Soc.*, 62(7-8):347–350.

Lee, S. K. and Stebbins, J. F. (1999). The degree of aluminum avoidance in aluminosilicate glasses. *American Mineralogist*, 84:937–945.

Lee, S. K. and Stebbins, J. F. (2000). The structure of aluminosilicate glasses: High-resolution ^{17}O and ^{27}Al MAS and 3QMAS NMR study. *J. Phys. Chem. B*, 104:4091–4100.

Lin, C.-C. and Liu, L. (2006). Composition dependence of elasticity in aluminosilicate glasses. *Phys. Chem Minerals*, 33:332–346.

Loewenstein, W. (1954). The distribution of aluminumin the tetrahedra of silicates and aluminates. *Am. Mineralogist*, 39:92–96.

Lower, N. P., Brow, R. K., and Kurjian, C. R. (2004). Inert failure strains of sodium aluminosilicate glass fibers. *J. Non-Cryst. Solids*, 344:17–24.

Lubas, M., Sitarz, M., Fojud, Z., and Jurga, S. (2005). Structure of multicomponent SiO_2-Al_2O_3-Fe_2O_3-CaO-MgO glasses for the preparation of fibrous insulationg materials. *J. Molecular Structure*, 744-747:615–619.

Malzbender, J., de With, G., and den Toonder, J. (2000). The P-h^2 relationship in indentation. *J. Mater. Res*, 15(5):1209–1212.

Manika, I. and Maniks, J. (2006). Size effects in micro- and nanoscale indentation. *Acta Materialia*, 54:2049–2056.

Meinhard, H., Grau, P., and Mosch, S. (1997). Hardness and flow behaviour of glass in the nanometer range - An interpretation of the load dependence of the hardness. *Glastech. Ber. Glass Sci. Technol.*, 70(11):333–339.

Mohr, J. G. and Rowe, W. P. (1978). *Fiber glass*. Van Nostrand Reinhold Company, USA.

Moynihan, C. T., Eastel, A. J., DeBolt, M. A., and Tucker, J. (1976). Dependence of the fictive temperature of glass on cooling rate. *J. Am. Cer. Soc.*, 59(1-2):12–16.

Mysen, B. O. (1995). Structural behavior of Al^{3+} in silicate melts: insitu, high-temperature measurements as a function of bulk chemical composition. *Geochim. Cosmochim. Acta*, pages 455–474.

Mysen, B. O. (2003). Physics and chemistry of silicate glasses and melts. *Eur. J. Mineral.*, 15:781–802.

Nagata, K. and Hayashi, M. (2001). Structure relaxation of silicate melts containing iron oxide. *J. Non-Cryst. Solids*, 282:1–6.

Nathan, H. D. and Van Kirk, C. K. (1978). A model of magmatic crystallization. *J. Petrol.*, 19:66–94.

Neuville, D. R., Cormier, L., and Massiot, D. (2006). Al coordination ans speciation in calcium aluminosilicate glasses: Effects of composition determined by ^{27}Al MQ-MAS NMR and Raman spectroscopy. *Chemical Geology*, 229:173–185.

Ohe von der, R. (2003). *Simulation of glass fiber forming processes*. PhD thesis, Aalborg University, Denmark.

Oliver, W. C. and Pharr, G. M. (1992). An improved technique for determining hardness and elastic modulus using load and displacement sensing indentation experiments. *J. Mater. Res.*, 7:1564–1583.

Peng, Z., Gong, J., and Miao, H. (2004). On the description of indentation size effect in hardness testing for ceramics: Analysis of the nanoindentation data. *J. Europ. Ceram. Soc.*, 24:2193–2201.

Pharr, G. M. and Bolshakov, A. (2002). Understanding nanoindentation unloading curves. *J. Mater. Res.*, 17(10):2660–2671.

Quinn, J. B. and Quinn, G. D. (1997). Indentation brittleness of ceramics: a fresh approach. *J. Materials Sci.*, 32:4331–4346.

Rouxel, T. (2006). Elastic properties of glasses: a multiscale approach. *C. R. Mecanique*, 334:743–753.

Russell, J. K. and Giordano, D. (2005). A model for silicate melt viscosity in the system $CaMgSi_2O_6$-$CaAl_2Si_2O_8$-$NaAlSi_3O_8$. *GeoChim. Cosmochim. Acta*, 69(22):5333–5349.

Schilling, F. R., Sinogeikin, S. V., Hauser, M., and Bass, J. D. (2003). Elastic properties of model basaltic melt compositions at high temperatures. *J. Geophys. Res*, 108(B6):10.1029/2001JB000517.

Sehgal, J. and Ito, S. (1999). Brittleness of glass. *J. Non-Cryst. Solids*, 253:126–132.

Sehgal, J., Nakao, Y., Takahashi, H., and Ito, S. (1995). Brittleness of glasses by indentation. *J. Mater. Sci. Lett.*, 14:167–169.

Shelby, J. E. (2005). *Introduction to glass science and technology*. The Royal Society of Chemistry, 2 edition.

Solvang, M. (2002). *Rheological and thermodynamic response to compositional variation in high aluminosilicate melts*. PhD thesis, Aalborg University, Denmark.

Solvang, M., Yue, Y. Z., Jensen, S. L., and Dingwell, D. (2004). Rheological and thermodynamic behaviors of different calcium aluminosilicate melts with the same non-bridging oxygen content. *J. Non-Cryst. Solids*, 336:179–188.

Stebbins, J. F., Lee, S. K., and Oglesby, J. V. (1999). Al-O-Al oxygen sites in crystalline aluminates and aluminosilicate glasses: High resolution oxygen-17 NMR results. *Am. Mineralogist*.

Tošić, M. B., Ž. Dimitrijević, R., Radosavljević, S. A., and Duričić, M. A. (1998). Influence of the iron oxidation state on the nucleation of basalt glass. *J. Serb. Chem. Soc.*, 63(12):1019–1030.

Troyon, M. and Martin, M. (2003). A critical examination of the p-h2 relationship in nanoindentation. *App. Phys. Lett.*, 83(5):863–865.

Tsui, T. Y., Oliver, W. C., and Pharr, G. M. (1996). Influences of stress on the measurement of mechanical properties using nanoindentation: Part I. Exparimental studies in an aluminium alloy. *J. Mater. Res.*, 11(3):752–759.

Van Landingham, M. R. (2003). Review of instrumented indentation. *Journal of Research of the National Institute of Standards and Technology*, 108(4):249–265.

Webb, S. (2005). Structure and rheology of iron-bearing Na_2O-Al_2O_3-SiO_2 melts. *Eur. J. Mineral.*, 17:223–232.

Xiufang, B., Lina, H., and Caidong, W. (2006). Degree of local structural ordering anf its correlation with the glass forming ability of alloys. *J. Non-Cryst. Solids*, 352:4149–4154.

Yilmaz, S., Bayrak, G., Sen, S., and Sen, U. (2006). Structural characterization of basalt-based glass-ceramic coatings. *Materials and Design*, 27:1092–1096.

Yoshida, S., Hidaka, A., and Matsuoka, J. (2004). Crack initiation behavior of sodium aluminosilicate glasses. *J. Non-Cryst. Solids*, 344:37–43.

Yoshida, S., Sanglebœuf, J.-C., and Rouxel, T. (2005). Quantitative evaluation of indentation-induced densification in glass. *J. Mater. Res.*, 20(12):3404–3412.

Yue, Y. Z. (2004). Calorimetric studies of structural heterogeneity of silicate liquids. *Ceramic Transactions*, 170:31–45.

Yue, Y. Z. (2008). Characteristic temperatures of enthalpy relaxation in glass. *J. Non-Cryst. Solids.*

Yue, Y. Z., deC. Christiansen, J., and Jensen, S. L. (2002). Determination of the fictive temperatur for a hyperquenched glass. *Chem. Phys. Lett.*, 357:20–24.

Yue, Y. Z., von der, R. O., and Jensen, S. L. (2004a). Erratum:"fictive temperature, cooling rate, and viscosity of glasses". *J. Chemical Physics*, 121.

Yue, Y. Z., von der, R. O., and Jensen, S. L. (2004b). Fictive temperature, cooling rate, and viscosity of glasses. *J. Chemical Physics*, 120:8053–8059.

List of articles

I. Crystallization behaviour and structural order of iron-containing aluminosilicate liquids, Lonnroth N. and Yue Y. Z. *Physics and Chemistry of Glasses*, 2005. **46** (4) 315-319.

II. Structural order and crystallization of an iron-rich aluminosilicate liquid under oxidizing conditions, Lonnroth N. and Yue Y. Z. *J. Non-Crystalline Solids*, 2008. **354** 1190-1193.

III. Nanoindentation of glass wool fibers, Lonnroth N., Muhlstein C. L., Pantano C. and Yue Y. Z., *J. Non-Crystalline Solids*, 2008. **354** 3887-3895.

IV. Influence of chemical composition on the physical properties of basaltic glasses, Lonnroth N. and Yue Y. Z., *Glass Technol.: Eur. J. Glass Sci Technol. A*, 2009. **50** (3) 165-173.

Article I

Ninth Int. Conf. on Structure of Non-Crystalline Materials, Corning, New York, USA, 11–14 July 2004 Phys. Chem. Glasses., 2005, 46 (4), 315–319

Crystallisation behaviour and structural order of iron containing aluminosilicate liquids

N. Lönnroth & Y. Z. Yue[1]

Section of Chemistry, Department of Life Sciences, Aalborg University, Sohngaardsholmsvej 57, DK-9000 Aalborg, Denmark

Manuscript received 19 August 2004
Revision received 24 January 2005
Accepted 31 January 2005

Two hyperquenched fibre samples are investigated for both melt structure and the crystallisation behaviour by differential scanning calorimetry and by x-ray diffraction methods. The two samples are distinguished through their exothermic (crystallisation) response during repeated DSC up- and downscans to temperatures above liquidus temperature. After repeated scans the crystallisation temperature increases, implying that the crystalline phase becomes more organised. The shift in the crystallisation temperature is sensitive to minor changes in chemical composition. This sensitivity makes it possible to analyse the origins of different crystallisation behaviours in different samples.

Basaltic glasses have a strong tendency to crystallise[1] When such a glass is heated, or the melt is cooled using a differential scanning calorimeter (DSC), crystallisation is detected as an exothermic peak. The crystallisation behaviour of basalt glass is sensitive to variations in chemical composition, forming conditions and measurement environment.[2,3]

Normally the liquidus temperature T_{liq} is defined as the temperature at which the last crystal is dissolved and all the ions have free mobility. Generally it is believed that a liquid is disordered and has amorphous structure. However, recent studies[4] have made this standpoint questionable. Structural order and heterogeneity[5] is reported both in liquids and glasses. It was shown[1] that after repeated heating above T_{liq} and subsequent cooling, the crystallised product changes into a more stable structure with each re-crystallisation. It is concluded that after remelting the previously crystallised product, the melt has an order that favours a specific crystal structure. Also as the melt temperature is raised the effect diminishes, since at temperatures high enough above T_{liq} the melt is unable to keep its ordered structure. Such a study can contribute to the understanding of structure and property relationships in these materials.

[1] Corresponding author. Email address: yy@bio.aau.dk

For industrial purposes the structural order in liquids affects glass forming, fibre spinning processes and the physical and mechanical properties of the fibre.[6] The aim of this work is to study the crystallisation behaviour of a basaltic glass based on the existence of structural order present in the liquid above T_{liq}. In addition, this paper deals with how the crystallisation behaviour changes with chemical composition. To reach these goals DSC and x-ray diffraction (XRD) measurements have been applied.

Experimental

Materials used in this study are stone wool fibres with a basaltic composition which are produced by a cascade spinning process.[7,8] Before measurements, the fibres were sieved to remove glass droplets and to obtain a uniform thickness distribution. The fibres have relatively high iron and alumina concentrations (Table 1). A highly reducing environment was obtained using Cupola furnaces. In this way all iron in the fibres was reduced to Fe^{2+}. The compositions of fibres used in this study are listed in Table 1, from which it can be seen that the main differences between these two fibres are in the amounts of FeO and MgO.

Differential scanning calorimetry

The heat flow rate, i.e. the output of the DSC, was measured with a simultaneous thermal analyser (Netzsch STA 449C Jupiter). The sample, approximately 20 mg of fibres, was placed in a platinum crucible in the sample holder of the STA in room temperature. The samples were heated to 60°C, held for 5 min, heated at a speed of 20°C/min up to T_{max} and then cooled at 20°C/min to 300°C. The samples were subjected to these up- and downscans, repeatedly for 5–6 times, where T_{max} was 1250, 1300, 1350 or 1400°C, respectively. All measurements were performed under an argon flow to avoid oxidation of the samples.

A baseline with empty crucibles was measured before each temperature programme for both materials, and this was subtracted from the DSC signals of the glass samples.

Table 1. *Composition of the studied fibres (in wt%). The chemical compositions were analysed using an x-ray fluorescence spectrometer (Philips 1404), with an error of less than 0·1 wt%*

	SiO_2	Al_2O_3	TiO_2	FeO	CaO	MgO	K_2O	Na_2O	P_2O_5	SO_3
Fibre 1	41·5	18·2	2·2	7·4	16·2	9·5	1·3	2·1	0·3	0·2
Fibre 2	41·5	18·0	2·0	6·4	16·4	10·9	1·4	2·2	0·3	0·2

X-ray diffraction

Samples of fibre 2 from one and five up- and downscans up to 1300°C and one sample from a single 1400°C up- and downscan, using the temperature programme described above, were also analysed with a x-ray diffractometer (STOE, Darmstadt). These samples were pulverised from crystallised samples recovered from DSC crucibles.

Results

Figure 1 shows a typical first up- and downscan curve, where the glass transition temperature T_g, the crystallisation peak temperature, T_{c1} for upscan and T_{c2} for downscan, and the liquidus temperature T_{liq} are observed. In the following upscans only a melting peak is seen since the material has crystallised on the previous downscan. We concentrate mainly on the downscan crystallisation exotherm, since it shows the most interesting features of the liquid.

At the liquidus temperature all the remaining crystals have disappeared. T_{liq} for fibre 1 is 1230°C, and hence when heated to T_{max} it is totally molten. During the downscan the melt crystallises at a certain temperature, depending on both T_{max} and on the thermal history of the sample. When the sample is reheated to T_{max}, the subsequent crystallisation during downscan is shifted towards a higher temperature (Figure 2(a)). The crystallisation peak continues to shift to higher temperatures with each repeated up- and downscan. The number of scans needed to reach a steady state depends on the maximum temperature and on the chemical composition of the material.

With T_{max} 1250 and 1300°C, the crystallisation peak of fibre 1 is sharp and well defined, and it has a well defined shift with each repeated scan (Figure 2(a) and (b)). When T_{max} is raised to 1350°C the crystallisation peak becomes broader (Figure 2(c)), and the position of the peak is nearly constant after the second upscan. When T_{max} is 1400°C the peak becomes even broader and the shift almost vanishes (Figure 2(d)). At this maximum temperature, the crystallisation peak area is smaller than at lower maximum temperatures, and a glass transition occurs both during cooling and heating at each repeated scan (Figure 3), indicating the presence of a glass phase. This glass phase crystallises during upscans at 1010°C, which is about 100°C higher than that for the first upscan. A similar effect, the shift of the crystallisation temperature (T_{c1}) towards higher temperatures during upscan, is observed in Kilauea basalt by Burkhard[9] where the shift is of the order of 70°C.

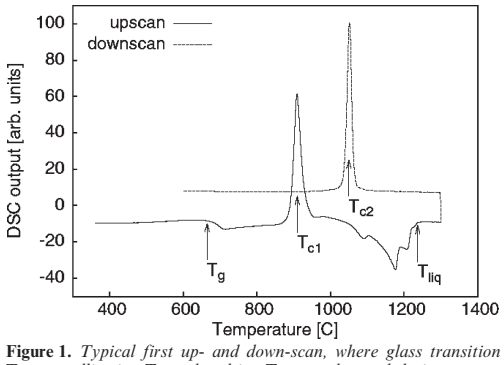

Figure 1. *Typical first up- and down-scan, where glass transition* T_g, *crystallisation* T_{c1} *and melting* T_{liq} *are observed during upscan and crystallisation* T_{c2} *during downscan*

The crystallisation behaviour of fibre 2 is similar to fibre 1, but since its liquidus temperature is 1270°C, the lowest maximum temperature used is 1300°C. The peak shift for fibre 2 at 1300°C is similar to that of fibre 1, at 1350°C the peak has become broader than for fibre 1 but it still shifts after each upscan, and at 1400°C the main difference is that the overall crystallisation temperatures are higher for fibre 2.

Discussion

Structural order and crystallisation

Traditionally, a molten material crystallises at a certain temperature and this phenomenon is independent of previous melting history. Here we observe that the crystallisation temperature shifts with the amount of up- and downscans, i.e. with the thermal history of the sample, where the maximum temperature also plays a role. The shift is more pronounced the closer the maximum temperature is to the liquidus temperature. This behaviour can be described as follows. The material has a crystalline structure when it melts, as the glassy fibres crystallised at around 900°C (sharp exotherm in the first upscan). At T_{liq} all of the crystal phase is then melted, with no further endothermic response being noticed in the DSC scans. In the liquid phase, the individual ions have free mobility as long as they find a new charge balancing position in which to move. When cooled, the mobility of the ions diminishes until the crystallisation temperature is reached, and hence a crystalline phase appears. As this crystalline material is reheated, some of the previous crystal structure is remembered by the liquid, and it is then easier for the ions to arrange into the crystal lattice when the temperature is dropped, thus the crystallisation occurs at a higher temperature than in the previous downscan. Due to the order in the liquid, it is easier for the ions to form a lattice and thus a more perfect crystal structure is formed during crystallisation. The structure in the liquid can be thought to consist of small nanoscale clusters of ions that stay nearly in their lattice positions causing an intermediate-range order. These structured clusters function as seeds for crystallisation and their structure, size and amount have a direct effect on the crystallisation. This process continues in the next scan.

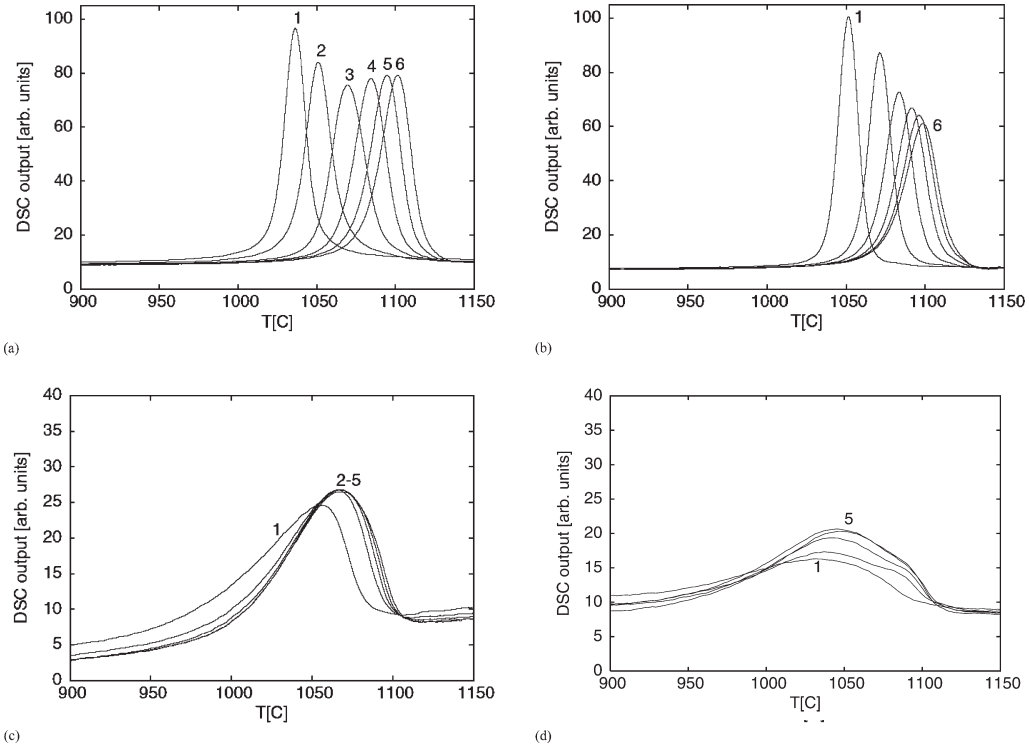

Figure 2. *Crystallisation peaks of fibre 1 with scan number indicated in the figure. The maximum temperature of the scans are (a) 1250, (b) 1300, (c) 1350 and (d) 1400°C. Notice different scales on y-axis*

Now the starting point for the liquid is a more perfect crystal structure which melts, so also the structure remembered by the liquid is more ordered. This can be seen since during the following downscan the crystallisation occurs at an even higher temperature than previously. Thus by performing repeated up- and downscans, the order in the liquid is increased.

Even though the shifting of the melting peak is small it is readily detectable. It shifts to higher temperatures as does the crystallisation peak. In comparison to the shift of the crystallisation peak, the shift of the melting peak is much smaller, only a few degrees per scan. Both peak shifts get smaller with larger scan number, but there is no apparent connection between the extent of the shifts. The melting peak shift may also be related to the more stable crystal structure, as removing impurities and crystal defects generally increases the melting point.

The above discussion of structure existing in liquid is verified by the scans with T_{max} being 1350 and 1400°C. When the maximum temperature is raised above 1300°C, the ions in the liquid become more and more mobile, and fewer of the clusters in the liquid are preserved. This is illustrated in Figures (2(c) and (d)), where the intensity of the peaks has decreased dramatically following an increase of the half-width of the peaks. Now the whole crystallisation process goes on for over 100°C, where it before was confined to a range of 20–40°C. Both observations indicate that the crystallisation process is not uniform and well defined, and that it is complicated by the high degree of disorder. This is also confirmed by the upscans up to 1400°C (Figure 3), where during every upscan a glass transition and a following crystallisation is observed. It seems that part of the molten material was not able to crystallise during cooling, but stayed in the glassy stage due to the high degree of disorder in the melt.

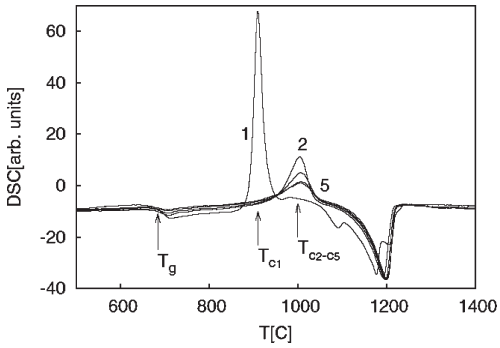

Figure 3. *Upscan of fibre 1 when T_{max} is 1400°C. Scan numbers, crystallisation peak maximums and glass transition indicated in the figure*

The structure of the crystalline material is studied by x-ray diffraction. The samples are taken from scans to 1300°C after one and five scans, where the crystallisation temperature difference between them is 50°C and, for comparison, a sample after one scan up to 1400°C. All the samples have, in the limit of detectability, the same crystal structure which resembles that of diopside/augite. The structure of these two cannot be distinguished as their diffraction peaks are so close to each other. Comparison between the different diffraction patterns shows that highest intensities and most well defined peaks are in the sample with five scans up to 1300°C, with next the sample with one scan up to 1300°C, whereas the peaks in the scan up to 1400°C show the most amorphous background noise (Figure 4). This confirms the interpretation of the DSC scans, i.e. due to the conserved order in the liquid repeated up- and downscans render the crystal structure more perfect. When the temperature is raised high enough above the liquidus, the crystallisation is then imperfect and an amorphous phase remains in the solid state.

To ensure that the observed crystallisation peak shifts are not due to dynamic processes, we conducted isothermal DSC measurements. The sample was kept at the maximum temperature (1300°C) for 15 min before downscanning. This measurement was done to ensure that: (i) the sample reaches thermal equilibrium, though this should be the case in all measurements as at these temperatures the viscosity of the melt is low (<20 Pa s[10]), (ii) the thermal lag between furnace and sample vanishes and (iii) the structure in the liquid has time to adjust to the prevailing temperature. The experiment was done on fibre 1 and the results are similar to those without the isotherm (Figure 5 curves 1300°C and 1300°C iso). The peak still shifts, although the shift is slightly less pronounced than for the sample that does not undergo the isotherm. Thus the ordered structure in the melt can be considered to be stable at a certain temperature. To ensure that the liquid is not able to recreate the ordered structure belonging to a certain T_{max} a second test was performed as follows. The sample was heated to 1400°C to melt the ordered structure, then cooled to 1300°C, and kept for 15 min to allow for the structure to rebuild before the downscan. The downscan showed crystallisation as with T_{max}=1400°C. Thus the liquid needs the history of the previous crystals to retain some order and to be able to enhance the following crystallisation.

The effect of sodium evaporation on the peak shift can be excluded as evaporation is higher the higher the maximum temperature, is and in our experiments we see the largest peak shifts with the lowest maximum temperatures.

Sensitivity to chemical composition

The results for the two fibres are different, but with similar main characteristics as expected since the compositions are very similar. So the previously discussed characteristics for the liquid and the conserved order within it are valid for both materials. The differences appear in the extent of the peak shift at the different temperatures (Figure 5). When T_{max} is 1300°C, the peak shift of both fibres is very similar, showing a 50°C change of crystallisation temperature after six scans. An increase of the maximum temperature to 1350°C affects fibre 1 more, where the peak is stationary after the first scan, while fibre 2 still has a 30°C shift in the

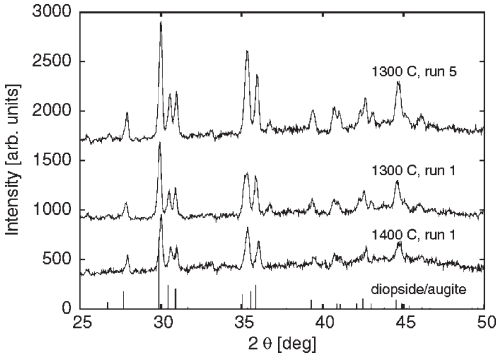

Figure 4. *X-ray diffraction patterns of fibre 2 with* T_{max} *1300°C (after one and five up- and downscans) and 1400°C (after one up- and downscan). On the x-axis calculated peak positions for diopside/augite*

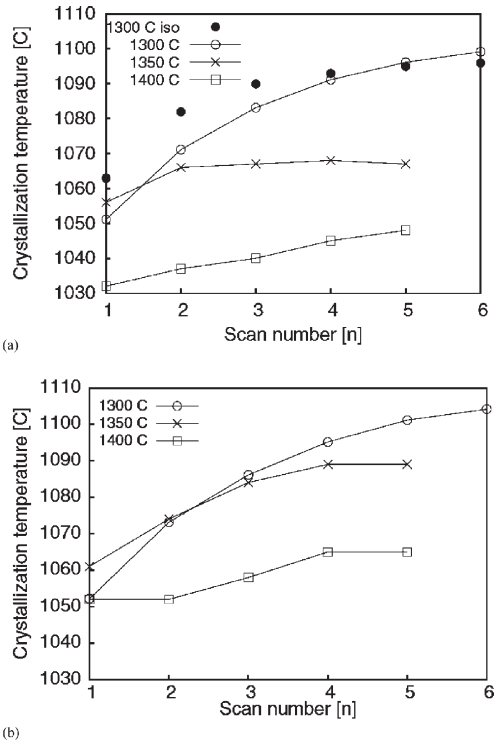

Figure 5. *The change of the crystallisation peak position as a function of scan number for each maximum temperature (*T_{max}*), which is indicated in the figure labels; (a) fibre 1 and (b) fibre 2. In (a) is also included peak positions for the isothermal experiment, where the sample was kept at* T_{max} *(1300°C) for 15 min*

crystallisation temperatures during the four first scans, whereafter the shift is negligible. Increasing T_{max} further to 1400°C produces a significant shift in fibre 1, since the crystallisation temperature of the first scan drops from 1050 to 1030°C compared to previous maximum temperatures, whereas this does not happen to fibre 2. A small increase in the crystallisation temperature with repeated scans is observed for both fibres at this T_{max}.

The higher liquidus temperature, T_{liq}, of fibre 2 can be a critical factor during production of fibres. If crystals remain in the melt, they will function as nuclei for crystallisation and the fibre properties will deteriorate since the glass structure is not homogeneous. Fibres are drawn at temperatures above and close to T_{liq}, so the structural order in the liquid affects the fibre drawing stability and the mechanical properties of the fibres.

Conclusions

Our results imply the presence of structural order in iron bearing silicate liquids in a certain range of temperatures above T_{liq}. This becomes visible after repeated up- and downscans with a DSC to temperatures above T_{liq}. The previous crystal structure is remembered to some extent by the liquid, which enhances the crystallisation during the downscan. The shift of the crystallisation peak to higher temperatures after each upscan is in response to increased order in the liquid. With increased maximum temperature of a scan, the kinetic energy of the ions increases and the structural order of the melt decreases. This is seen as a smaller shift of the crystallisation peak and as a residual glass phase in the solid state. The structural order of the liquid is verified, and a crystal structure with less defects can be obtained by performing repeated up- and downscans.

The two fibres used in this study can be distinguished by their liquidus temperature and by the way the crystallisation peak shifts in downscans with different maximum temperatures.

Acknowledgements

The authors thank Søren Primdahl for useful discussion and Rockwool International.

References

1. Yue, Y. Z. *J. Non-Cryst. Solids*, 2994, **345–346**, 523–7.
2. Burkhard, D. J. M. *Contrib. Miner. Petrol.*, 2002, **142**, 724–37.
3. Yilmaz, S., Özkan, O. T. & Günay, V. *Ceram. Int.*, 1996, **22**, 477–81.
4. Wilding, M. C., McMillan, P. F. & Navrotsky, A. *Physica A*, 2002, **419**, 381–90.
5. Martin, J. D., Goettler, S. J., Fossé, N. & Iton, L. *Nature*, 2002, **419**, 381–4.
6. Bauer, J. F. *Proc 1999 TAPPI Nonwovens Conference*, Orlando, 1999.
7. Axten, C. W. *et al*. Nomenclature Committee of TIMA Inc., 1993.
8. Yue, Y. Z. & Angell, C. A. *Nature*, 2004, **427**, 717–20.
9. Burkhard, D. J. M. *J. Petrol.*, 2001, **42** (3), 507–27.
10. Yue, Y. Z., von der Ohe, R. & Jensen, S. L. *J. Chem. Phys.*, 2004, **120**, 8053–9.

Article II

Available online at www.sciencedirect.com
ScienceDirect
Journal of Non-Crystalline Solids 354 (2008) 1190–1193
JOURNAL OF NON-CRYSTALLINE SOLIDS
www.elsevier.com/locate/jnoncrysol

Structural order and crystallization of an iron-rich aluminosilicate liquid under oxidizing condition

Nadja Lonnroth, Yuan-Zheng Yue *

Section of Chemistry, Aalborg University, Sohngaardsholmsvej 57, DK-9000 Aalborg, Denmark

Available online 26 November 2007

Abstract

An iron-rich aluminosilicate liquid is studied in different atmospheres by using differential scanning calorimetry. The results show that the oxidation state of iron and the maximum temperature of the scan have an effect on the liquid structure and on the crystallization behavior of the liquid during both cooling and reheating processes. Increase in Fe^{2+}/Fe^{3+} enhances crystallization and favors formation of a stable crystal structure. The structural order conserved in the liquid is an intrinsic phenomenon, which is not related to the oxidation state of iron.

PACS: 61.20.−p; 64.70.Dv; 07.20.Fw

Keywords: Crystallization; Structure; Calorimetry

1. Introduction

The structure of basaltic liquids in an inert argon atmosphere has been studied indirectly by performing differential scanning calorimetry (DSC) measurements by repeatedly heating samples up to temperatures above liquidus (T_{liq}) [1,2]. Experimental results reported in [1,2] indicate that some structural order of the previous crystal structure is conserved in the liquid. When the sample is cooled down its crystallization is affected by the structure in the liquid and with continued heating cycles the formed crystalline structure changes towards the energetically most stable one.

It is known that Fe^{2+} ions act as network modifiers in glass, and is octahedrally coordinated with six non-bridging oxygen. In contrast Fe^{3+} ions can be both tetrahedrally and octahedrally coordinated. If alkali ions are present in the glass, then Fe^{3+} can play a role as a network former. Studies on the dynamics of the oxidation [3,4] reveal how the oxidation process proceeds in the melt. The changes in coordination structures and oxidation states of iron during equilibration processes have been investigated for the iron–calcium–silicate liquid [5]. For the nucleation process an increase in Fe^{2+} content lowers the nucleation temperature by 5 °C and the nucleation rate by 13.4% according to [6]. The aim of this study is to gain understanding on the structure of the liquid above liquidus and to see how the oxidation state of iron affects the crystallization of this iron-rich aluminosilicate glass.

2. Experimental

A basalt-like glass with chemical composition of (in wt%) 41.5 SiO_2, 18.2 Al_2O_3, 2.2 TiO_2, 7.4 FeO, 16.2 CaO, 9.5 MgO, 1.3 K_2O, 2.1 Na_2O, 0.3 P_2O_5, 0.2 SO_3 is used in this study, where the iron is in reduced form (Fe^{2+}) due to strongly reducing conditions of the melt process. To understand better the melting, the crystallization, and oxidation processes we have conducted DSC

* Corresponding author. Tel.: +45 9635 8522; fax: +45 9635 0558.
E-mail address: yy@bio.aau.dk (Y.-Z. Yue).

0022-3093/$ - see front matter © 2007 Elsevier B.V. All rights reserved.
doi:10.1016/j.jnoncrysol.2006.10.082

measurements in air atmosphere, thus causing the iron to oxidize. The measurements are conducted with a simultaneous thermal analyzer (STA) (Netzsch STA 449C) that records both the heat flow rate, i.e. DSC output and the thermogravity (TG) signals. Approximately 20 mg of pulverized sample was placed in one of the platinum pans while the reference was kept empty. The samples were heated with the STA at a rate of 20 °C/min to a temperature above liquidus and then cooled to room temperature at the rate of 20 °C/min. This heating–cooling cycle is repeated six times for each maximum temperature. The procedure is similar to that used for the study in argon atmosphere [2]. The maximum temperatures (T_{max}) are 1250 °C, 1300 °C, 1350 °C, 1400 °C and 1425 °C, while the liquidus temperature of the glass lies at 1230 °C. For each of the temperatures a baseline was measured with empty crucibles, which was subtracted from the DSC signals of the glass samples.

To reveal the crystal structure of the melted and thereafter crystallized samples, some samples were recovered from the DSC pans and subjected to X-ray diffractometry (XRD). The samples were finely ground and placed onto silica wafers to have a homogenous background. Measurements were carried out with Cu radiation on a STOE θ–θ reflection diffractometer. To confirm the oxidation state of iron in the crystalline material, the samples measured by XRD were afterwards subjected to Mössbauer spectroscopy.

3. Results

Glasses with the above-mentioned composition show generally the following thermal responses when measured with a DSC in air atmosphere. During the first upscan, i.e. heating at 20 °C/min, a glass transition occurs at approximately 690 °C (T_g), the material crystallizes at around 900 °C, and finally the material begins to melt at 1100 °C. The liquidus temperature is 1230 °C, at which all crystals are molten. During the downscan, i.e. cooling, the material crystallizes at temperatures between 1000 °C and 1140 °C (T_c) and no other thermal responses are noted during the remaining cooling. Thus during following upscans the only thermal event is melting of the crystals formed during the prior downscanning. The exact temperatures of T_g, T_m and T_c vary with the maximum temperature of the scan (T_{max}), the thermal history and the measurement atmosphere.

When T_{max} is 1250 °C or 1300 °C the crystallization peak is narrow and sharp both in air and argon atmospheres, but in argon the crystallization temperature shifts considerably to higher temperatures with increasing scan number, while in air T_c is fairly constant at 1120 °C (see Figs. 1 and 2). Raising the maximum temperature to 1350 °C causes the peak to broaden, and in argon the crystallization peak is now stationary at 1070 °C and in air T_c is 1100 °C. When the maximum temperature reaches 1400 °C the following phenomena can be observed. Firstly, the

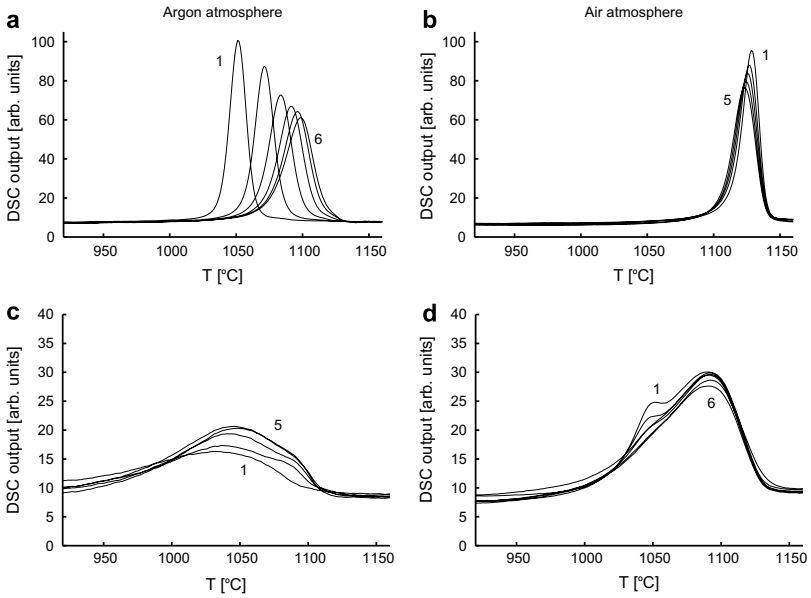

Fig. 1. Crystallization peaks of the first downscans in air and in argon atmospheres for maximum upscan temperatures of 1300 °C (upper diagrams) and 1400 °C (lower diagrams). Notice different scales on *y*-axis.

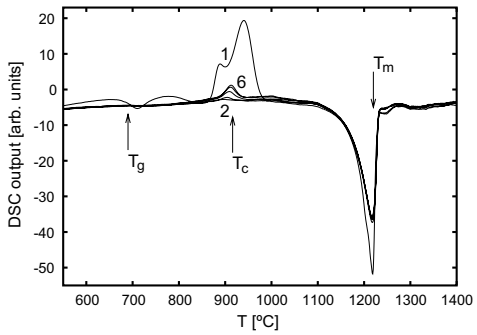

Fig. 2. DSC upscans in air atmosphere when the maximum temperature of a scan is 1400 °C. Scan numbers and glass transition, crystallization and melting temperatures are indicated in the figure.

Table 1
Redox state of iron in samples that have undergone one heating cycle, measured by Mössbauer spectroscopy with an accuracy of ±3%

Atmosphere	T_{max} (°C)	Fe^{2+} (mol%)	Fe^{3+} (mol%)
Air	1300	6	94
Air	1400	4	96
Argon	1300	80	20

crystallization peak for the downscans becomes very broad and covers a temperature interval of over 100 °C with maximums at $T_{c,argon} = 1040$ °C and $T_{c,air} = 1090$ °C. Secondly there appears a secondary crystallization peak in air at 1040 °C (Fig. 1). Finally, when this crystalline material is reheated during the next upscan a crystallization peak appears at 900 °C in air (Fig. 2), indicating existence of a glass phase within the solid, the volume fraction of which though is relatively small as the glass transition is not visible.

The Mössbauer measurements (see Table 1) reveal, as expected, that heating in air leads to nearly full oxidation of Fe^{2+} in the samples. The molar ratio $[Fe^{3+}]/[Fe^{2+} + Fe^{3+}]$ is 94% for the sample heated to 1300 °C, and 96% for the sample heated to 1400 °C.

4. Discussion

From the DSC measurements on the glass used in this study it is found that the oxidation state of the iron alters both the structural order of the liquid and the crystallization behavior. In general the differences of crystallization behavior, observed when the glass sample is heated in air and argon, respectively, are comparable to those observed in a basaltic liquid (see Ref. [7]). The first upscan crystallization occurs in two events in air and in one event in argon with an approximate crystallization temperature between the two peak temperatures of the air scan. The crystallization at a lower temperature in air is due to the increasing proportion of the Fe^{3+} ions which is favorable for the formation of spinel crystals that provide a platform for pyroxene to nucleate and grow on [8]. Both spinel and the most common pyroxene, augite, crystals are detected in our XRD measurements.

4.1. Oxidation of iron

When the maximum temperature of a DSC scan is between 1250 °C and 1350 °C the downscan crystallization peak becomes broader with increasing maximum temperature as also was the case for crystallization in argon, but the shift in crystallization temperature to higher temperatures with increasing scan number observed in argon (Figs. 1 and 2) does not occur in air atmosphere. Also the melting and crystallization temperatures for the samples with more Fe^{3+} ($T_{m,air} = 1220$ °C and $T_{c,air}$ (scan 5) = 1120 °C) are both higher than for the samples with less Fe^{3+} ($T_{m,argon} = 1200$ °C and $T_{c,argon}$ (scan 5) = 1097 °C). Both notions indicate that the oxidation of the Fe^{2+} ions has made the structure of the liquid more favorable for forming a stable crystal structure. Such liquid structure has lower energy barrier for ions to overcome for rearranging themselves in the way that a stable crystal phase easily forms during cooling. In argon atmosphere the crystalline phase had to be melted and recrystallized several times before the ions were in the most favorable positions for crystallization.

4.2. Liquid structure

As the maximum temperature is raised from 1350 °C to 1400 °C more pronounced changes occur. At this high temperature the liquid is so disordered that during cooling (downscan) the liquid is unable to rearrange in a manner to form a fully crystallized phase. The crystallization process for $T_{max} = 1400$ °C occurs over a temperature interval of 100 °C, whereas for $T_{max} = 1300$ °C the interval is 40 °C (Fig. 1). This significant difference in crystallization behavior can also be seen in a lower oxidation state of iron (Fig. 1), which confirms that the crystal memory effect and an ordered structure exists in the basaltic liquid in a certain temperature range above T_{liq}. As discussed in [1,2,9], the degree of the structural order in the liquid increases with increasing the number of up- and downscans, and this leads to a more and more easy formation of crystals. The ordered regimes of structure are most probably comparable to a scale of the so-called medium-range order (MRO), i.e. the nanometer scale. The MRO of the multi-component oxide liquids are also evidenced in [10], with respect to agreement between viscosity obtained by Adam–Gibbs MRO theory and experimental data. The structural order indirectly inferred in the present work and in [1,2] could be associated with microinhomogeneities of the glass [11]. Due to the difficulty of crystallization during downscans some glassy phase is conserved, which is revealed in the second upscan as an exotherm due to the crystallization of the glassy phase. The composition of

the glassy phase is different when heating in air or argon, as in argon the glassy phase crystallizes at approximately 80 °C higher temperature than in air. The higher crystallization temperature in the second scan in argon is also noted in [7].

Another noticeable change in the air scan when T_{max} is 1400 °C, is that the downscan crystallization of the liquid includes two exothermic events, where the crystallization temperatures differ by approximately 50 °C. When comparing the X-ray powder diffraction (XRD) patterns of the materials heated to 1300 °C and 1400 °C, the latter shows several diffraction maxima that do not occur in the former, but due to complexity of the materials it is not possible to identify the origin of these peaks. But both augite and spinel could be identified from the spectra and the unit cell sizes could be calculated for each of them.

5. Conclusions

In the studied basaltic liquid the oxidation state of iron and the maximum temperature of the DSC scan affect the crystallization process and thus the structural order of the liquid, for which crystallization can be used as an indirect indicator in the repeated DSC scanning method. Both in argon and air atmospheres a distinct change is observed in the downscan crystallization behavior when the maximum temperature is increased from 1300 °C to 1400 °C, indicating that the liquid structure, present in the liquid at temperatures below $T_{liq} + 200$ °C, is a general feature of these liquids irrespective of the oxidation state. But the oxidation state does affect the dynamics of the crystallization, as Fe^{3+} ions increase both the melting and crystallization temperatures.

Acknowledgments

The authors thank Finn Willy Poulsen and Steen Mørup for help with the XRD and the Mössbauer measurements, respectively. This work is financially supported by Rockwool International A/S.

References

[1] Y.Z. Yue, J. Non-Cryst. Solids 345&346C (2004) 523.
[2] N. Lönnroth, Y.Z. Yue, Phys. Chem. Glasses 46 (2005) 315.
[3] R.F. Cooper, J.B. Fanselow, J.K.R. Weber, D.R. Merkley, D.B. Poker, Science 274 (1996) 1173.
[4] G.B. Cook, R.F. Cooper, Am. Miner. 85 (2000) 397.
[5] K. Nagata, M. Hayashi, J. Non-Cryst. Solids 282 (2001) 1.
[6] M.B. Tosic, R.Z. Dimitrijevic, S.A. Radosavljevic, M.A. Duricic, J. Serb. Chem. Soc. 63 (1998) 1019.
[7] D.J.M. Burkhard, J. Petrol. 42 (2001) 507.
[8] M.A. Bouhifd, P. Richet, P. Besson, M. Roskosz, J. Ingrin, Earth Planet. Sci. Lett. 218 (2004) 31.
[9] Y.Z. Yue, Ceram. Trans. 170 (2004) 31.
[10] R. Conradt, J. Non-Cryst. Solids 345&346 (2004) 16.
[11] V.V. Golubkov, V.N. Bogdanov, A.Y. Pakhnin, V.A. Solovyev, E.V. Zhiveava, V.O. Kabanov, O.V. Yanush, S.V. Nimilov, A. Kisliuk, M. Soltvisch, D. Quitmann, J. Chem. Phys. 110 (1999) 4897.

Article III

Journal of Non-Crystalline Solids 354 (2008) 3887–3895

Contents lists available at ScienceDirect

Journal of Non-Crystalline Solids

journal homepage: www.elsevier.com/locate/jnoncrysol

Nanoindentation of glass wool fibers

Nadja Lonnroth [a,*], Christopher L. Muhlstein [b], Carlo Pantano [b], Yuanzheng Yue [a,*]

[a] Section of Chemistry, Aalborg University, DK-9000 Aalborg, Denmark
[b] Department of Materials Science and Engineering, Materials Research Institute, The Pennsylvania State University, PA-16802, United States

ARTICLE INFO

Article history:
Received 14 December 2006
Received in revised form 3 March 2008
Available online 14 June 2008

PACS:
81.05.Je
62.20.Qp
81.70.−q

Keywords:
Fibers and waveguides
Mechanical properties
Indentation, Microindentation
Aluminosilicates
Medium-range order

ABSTRACT

The nanoindentation technique is used to analyze the depth dependence of the hardness and the reduced elastic modulus of bulk glasses and glass wool fibers (4–12 μm in diameter) of calcium aluminosilicate composition. In spite of the fiber geometry and the delicate sample mounting-technique, nanoindentation proves to be a relatively accurate method that provides reproducible data for both hardness (H) and reduced elastic modulus (E_r) of thin glass fibers. It is found that H and E_r are generally lower for the fiber than for the bulk sample. Within a given fiber, both H and E_r are approximately constant with increasing indentation depth. However, both of these parameters decrease with diminishing fiber diameter. This trend is attributed to an increase of the free volume of the fibers with decreasing fiber diameter, i.e. to an increase of the fictive temperature.

1. Introduction

As modern materials, glass fibers play crucial roles both in industrial applications and in everyday life. For instance, they are widely used in the sectors of optical communication, construction, insulation, and composite materials technology. There are two types of glass fibers: continuous and discontinuous fibers. The former is produced by continuously drawing a fiber from melts, while the latter is obtained by stretching short discontinuous fibers from melts using centrifugal processes. Continuous glass fibers are often used for optical communication and reinforcement of materials ranging from plastics to cement, whereas discontinuous fibers are used for thermal and acoustic insulation. The primary objectives of the present study are aimed at the discontinuous fibers using both E-glass and basaltic glass compositions. The basaltic wool fibers are not only a good insulation material, but also an outstanding fire barrier due to high-temperature structural stability.

For efficient insulation and structural applications, the glass wool fibers should possess qualified mechanical properties. To obtain qualified mechanical properties, one of the most important things to do is to find out how the fiber forming conditions influences the mechanical properties of fibers. The present paper focuses on the dependences of both hardness (H) and reduced elastic modulus (E_r) of glass wool fibers on the glass forming condition. To reveal the intrinsic elastic and plastic responses of the fibers to external mechanical force, both E and H values of the fibers will be directly measured using the nanoindentation technique. To the best of our knowledge, direct measurements of elastic property and hardness of glass wool fibers have not been reported in literature. This study aims to enhance the understanding of how processing conditions affect the network structure and the associated deformation and failure of the material.

Mechanical properties of fibers are usually studied by measuring the tensile strength [1,2] or the strain to failure [3,4] under uniaxial loading. It is generally known that the strength of a glass is mainly governed by the size of defects present in the material [5] (i.e., weakest link statistics), resulting in higher strength for fibers than for bulk glass and an increasing trend for the tensile strength of fibers with decreasing fiber diameter [5–7]. Although tensile testing methods are most often applied to continuous fibers, the mechanical behavior of shorter, cylindrically-shaped fibers (e.g., discontinuous chopped or wool fibers) can also be quantified [8]. The tensile strength of continuous and discontinuous glass fibers is affected by parameters such as the chemical composition,

* Corresponding authors. Present address: Department of Fuel Cells and Solid State Chemistry, Risø National Laboratory, Technical University of Denmark, P.O. Box 49, 4000 Roskilde, Denmark. Tel.: +4546775722 (N. Lonnroth).
E-mail addresses: Nadja.loennroth@risoe.dk (N. Lonnroth), yy@bio.aau.dk(Y.Z. Yue).

0022-3093/$ - see front matter © 2008 Elsevier B.V. All rights reserved.
doi:10.1016/j.jnoncrysol.2008.04.014

melting temperature, melt homogeneity, cooling rate, drawing force and atmosphere [9,10]. The underlying origins of the variations in the behavior include contributions from not only the defect populations, but from changes in the atomic structure of the glass fiber as well. The structure and property differences between fiber and bulk glass are attributed to their differences in both cooling rate and tensional stress during forming [11,12]. Specifically, the temperature at which the structure of the liquid is frozen-in in the solid state is termed the 'fictive temperature' (T_f). Higher fictive temperatures are associated with more open structures (i.e., higher free volume) that have lower resistance to elastic and plastic deformation. Bulk glasses reach a quasi-equilibrium glass state during the annealing process and have a lower fictive temperature. Consequently, bulk glasses have a more compact and ordered intermediate-range structure and lower configurational entropy than fibers. The fiber forms of glasses have a higher T_f and a more disordered structure than bulk glass because the cooling rate during fiber production is up to $\sim 10^6$ K/s [13], and as well, because fibers are not intentionally annealed.

The fictive temperature is a function of both the chemistry and the thermal history of the glass, and the correlations between the mechanical properties of glasses and cooling rate (i.e., fiber diameter) are not well understood. This fundamental question is complicated by the fact that, compared to continuous fibers, there can be in homogeneneity in spun fibers associated with temperature uniformity in the melt feed and variability in the cooling rate [14]. Consequently, it is unclear if mechanical tests conducted on melt spun fibers can yield reproducible mechanical property data. Moreover, the flow behavior of the glasses cannot be evaluated in a tensile test, so indentation techniques must be used. Instrumented indentation testing at the nano- and micro scale are widely used to measure the hardness and elastic modulus of near-surface layers and of thin films. In principle, it can also be applied to sample geometries such as fibers and particulates. An early study with nanoindentation applied on polished cross sections of continuous glass fibers exists [15], as well as nanoindentation on nanofibers of several materials (silver, PLLA, vitreous SiO_2, etc.) [16–20]. The objective of this study is to use nanoindentation to characterize the mechanical properties of melt spun E- and basaltic glass fibers with a range of cooling rates (diameters). This strategy will allow us to explore the intrinsic atomic structure of the glasses without the complicating effects of cracks and other extrinsic flaws.

2. Nanoindentation analysis

Nanoindentation is a technique widely used for determining hardness (H) and elastic modulus (E) of the near-surface region of materials. The analysis is most often based on the Oliver–Pharr method where the load-depth unloading curve is used [21]. The hardness is defined as

$$H = \frac{P_{\max}}{A_c}, \tag{1}$$

where $P_{\max}$ is load and A_c is the projected contact area at the maximum depth of penetration. For a perfect Berkovich tip the contact area is

$$A_c = 24.56 h_c^2, \tag{2}$$

with contact depth given by $h_c = h_{\max} - \varepsilon P_{\max}/S$. Here S is the stiffness obtained from the unloading curve slope and ε is the indenter geometry constant, typically given the value 0.75 or 0.76 [22]. The unloading stiffness defines the reduced elastic modulus of the sample

$$E_r = \frac{\sqrt{\pi}}{2}\frac{S}{\sqrt{A_c}}, \tag{3}$$

from which the elastic modulus (E) of the sample, knowing the Poisson ratio v, is found by

$$\frac{1}{E_r} = \frac{1-v^2}{E} + \frac{1-v_i^2}{E_i}. \tag{4}$$

The E_i and v_i are, respectively, the elastic modulus and Poisson's ratio of the diamond indenter (E_i = 1140 GPa, v_i = 0.17 [23–27]).

The loading portion of the force-displacement curve generated during indentation with a sharp indenter, such as the Berkovich geometry, is a combination of both plastic and elastic deformation. This is generally true, even for brittle materials such as crystalline and amorphous ceramics. For the Berkovich tip it has been shown [28] that the loading curve in general follows the relationship:

$$P = Kh^2, \tag{5}$$

where K is a constant. This constant can be evaluated analytically and is a function of H and E and the shape of the indenter [29,30]. For a non-ideal tip the effect of tip rounding should be taken into account by using $h + h_b$ instead of h in Eq. (5), where h_b is the distance between the blunt end and the perfect end of the indenter cone [29].

The analysis methods described above are all based on the assumption that the contact between the indenter and the sample follows Hertzian contact stress theory [31]. With this methodology, it is assumed that both surfaces are smooth and that the indenter indents a semi-infinite, flat half-space where the stresses disappear at great distances from the contact zone. Compared to flat samples, the curved surface of fibers induces an asymmetry that becomes more pronounced with decreasing fiber diameter. The importance of the geometry to the measured properties of the fiber can be evaluated using the more general form of the solutions to the elastic contact problem.

The validity of the Oliver–Pharr analysis approach for instrumented indentation hinges on several key assumptions. In addition to requiring homogeneous, isotropic, linear elastic materials behaviors, the analysis also assumes that the substrate is a flat, infinite sheet. In the case of this work, the presence of a finite curvature of the fibers raises critical questions about what strategy should be used to interpret the force-displacement data from the instrumented indentation tests. The presence of a finite curvature for the substrate is not unique to this work, and has been encountered in a wide variety of contact mechanics problems and other instrumented indentation studies [20]. The general solution for the stresses and strains due to contact between two homogeneous, linear elastic bodies with arbitrary curvatures and orientation can be evaluated using solution strategies first established by Hertz and reviewed in many advanced mechanics textbooks [32]. The contact region can generally be described using elliptical integrals that, when properly implemented, capture the effect of the geometry on the resulting stiffness of the indenter-sample contact. If we apply this methodology to the indentation of fibers in this work, the conventional (i.e., Oliver–Pharr) analysis can be corrected for the finite curvature of the specimens.

The objective of this analysis is to quantify the contribution of the sample geometry to the apparent stiffness of the indenter-fiber contact. Let us begin by denoting the indenter as body '1' that is made from polycrystalline diamond (thereby ignoring orientation effects of the single crystal indenter) with an elastic modulus, E_1, of 1140 GPa and a Poisson's ratio, v_1, of 0.17 [23–27]. For the purposes of this analysis, we will approximate the Berkovich tip by an 'equivalent sphere' that has principal radii, R_1 and R_1', that are the size required for a sphere that would have the same projected contact area as the Berkovich geometry at the penetration depth of interest. The second body in the system is the fiber, which has an elastic modulus, E_2, of 100 GPa and a Poisson's ratio, v_2, of 0.17. These values are consistent with the silicate glasses evaluated in

this study, but the exact values of the materials properties are not necessary to calculate the error associated with the geometry of the fiber or to correct the hardness and reduced modulus. While not exact, this equivalent spherical contact strategy allows for a reasonable estimation of the effects of sample curvature and a correction of hardness and reduced modulus results. Berkovich indenters have a nominally spherical, finite radius tip that is on the order of 100 nm. Consequently, penetration depths that are 100 nm or less can deviate significantly from the ideal projected area of the Berkovich three-sided pyramid. However, the projected contact area inferred from the empirically measured stiffness and the associated projected contact area of the indenter-sample system can be corrected with the equivalent sphere strategy across the full range of contact depths. Moreover, since the penetration depths in this work are small, the idealization of the indentation tip as a sphere is not particularly problematic. If we assume that the substrate is flat, the principal radii of the second body, R_2 and R_2', are equal to infinity. However, if the actual geometry is considered, the major principal radius is infinity and the minor principal radius is equal to the radius of the fiber (2.5 to 10 μm). Normally, contact mechanics analyses also allow for arbitrary angles between the major principal radii of the two bodies, but since the equivalent spherical indenter is axisymmetric, the angle between the indenter and fiber, α, is zero. The general features of the geometry can then be lumped into two constants, A and B, which are defined as follows [32]:

$$A = \frac{1}{4}\left(\frac{1}{R_1}+\frac{1}{R_2}+\frac{1}{R_1'}+\frac{1}{R_2'}\right) + \frac{1}{4}\sqrt{\left[\left(\frac{1}{R_1}-\frac{1}{R_1'}\right)+\left(\frac{1}{R_2}-\frac{1}{R_2'}\right)\right]^2 - 4\left(\frac{1}{R_1}-\frac{1}{R_1'}\right)\left(\frac{1}{R_2}-\frac{1}{R_2'}\right)\sin^2\alpha}, \tag{6}$$

$$B = \frac{1}{4}\left(\frac{1}{R_1}+\frac{1}{R_2}+\frac{1}{R_1'}+\frac{1}{R_2'}\right) + \frac{1}{4}\sqrt{\left[\left(\frac{1}{R_1}-\frac{1}{R_1'}\right)+\left(\frac{1}{R_2}-\frac{1}{R_2'}\right)\right]^2 - 4\left(\frac{1}{R_1}-\frac{1}{R_1'}\right)\left(\frac{1}{R_2}-\frac{1}{R_2'}\right)\sin^2\alpha}. \tag{7}$$

The ratio of B to A is related to a quotient of elliptic integrals of the first and second kind. The complete elliptic integral of the first kind, $K(m)$, where m is a 'parameter' is given by the following relationship:

$$K(m) = \int_0^{\pi/2}\left[1 - m\sin^2\theta\right]^{-1/2}\mathrm{d}\theta. \tag{8}$$

Similarly, the complete elliptic integral of the second kind, $Q(\mathrm{m})$, is defined as follows:

$$Q(m) = \int_0^{\pi/2}\left[1 - m\sin^2\theta\right]^{1/2}\mathrm{d}\theta. \tag{9}$$

Standard convention in the mathematics literature is to denote the complete elliptic integral of the second kind as $E(m)$, but that nomenclature has been abandoned in this work to avoid confusion with various forms of the elastic modulus. The ratio of B to A is related to the complete elliptic integrals through the following relationship:

$$\frac{B}{A} = \frac{\left(\frac{1}{(1-m)}\right)Q(m) - K(m)}{K(m) - Q(m)}. \tag{10}$$

The root of this equation, m, can be found by standard iterative schemes available in commercial numerical analysis packages such as Mathematica and Matlab. The geometry captured by the ratio of B to A, and the appropriate elliptic integral parameter is then used to determine the compliance (or stiffness) of the indenter-fiber system. The materials properties (via the reduced modulus of the system) and geometry are lumped into a composite parameter, Δ, which has the following form:

$$\Delta = \frac{1}{A+B}\left(\frac{1-\nu_1}{E_1}+\frac{1-\nu_2}{E_2}\right). \tag{11}$$

The response of the system (such as stresses, strains, or displacements) typically scales with a ratio of a parameter, b, to Δ. The parameter b, is one of the two semi-minor axes of the elliptical contact region. This parameter combines the mechanical and geometric properties of the system with the applied force, P, through the following relationship:

$$b = \sqrt[3]{\frac{3(1-m)^{1/2}Q(m)P\Delta}{2\pi}}. \tag{12}$$

The second axis of the elliptical contact region, a, is a function of the size of the first axis and the elliptical integral parameter, m.

$$b = a\sqrt{(1-m)} \tag{13}$$

The area of the contact region is simply the area of the ellipse, πab. The compliance of the equivalent sphere system, C_{eq}, is then calculated from the following equation:

$$C_{\mathrm{eq}} = \frac{3\times\sqrt{(1-m)}K(m)(A+B)}{2\pi(b/\Delta)}. \tag{14}$$

The stiffness of the equivalent sphere system, S_{eq}, is given by the inverse of the equivalent compliance. If we compare the calculated compliance for the diamond indenter-fiber system to the compliance of the diamond indenter-flat substrate system, we can quantify the magnitude of the error associated with applying the standard Oliver–Pharr analysis to a fiber specimen.

Both the reduced elastic modulus and hardness values calculated from the unloading stiffness of the system using the Oliver–Pharr analysis strategy can be adjusted for the effects of the known fiber geometry by introducing a geometric correction factor. In general, the projected contact area determined for the flat substrate case is larger than when a small fiber is indented. As a result, the actual hardness of the fiber (over the size range and penetration depths relevant to this study) is higher than predicted by the Oliver–Pharr analysis approach. The actual hardness of the fiber, H_{fiber}, can be found by multiplying the calculated hardness by a ratio of the calculated contact areas for the equivalent sphere indentation on the flat, $A_{\mathrm{eq,flat}}$, and fiber, $A_{\mathrm{eq,fiber}}$, cases.

$$H_{\mathrm{fiber}} = H\left(\frac{A_{\mathrm{eq,flat}}}{A_{\mathrm{eq,fiber}}}\right). \tag{15}$$

A similar factor can be developed for correcting the reduced elastic modulus errors that are introduced by ignoring the curvature of the substrate. Recall from (3) that the reduced modulus of the system is proportional to the unloading stiffness, S, multiplied by a constant that is related to the geometry of the interacting bodies. If we consider only the effect of geometry (i.e., the elastic properties of the indenter and substrate are held constant) for the configurations relevant to this study, the stiffness of an equivalent indenter-fiber contact, $S_{\mathrm{eq,fiber}}$, is less than the equivalent indenter-flat substrate system, $S_{\mathrm{eq,flat}}$ As a result, the geometric factor for the flat system, $F_{\mathrm{eq,flat}}$,will be smaller than that of the fiber system, $F_{\mathrm{eq,fiber}}$. The ratio of these geometric factors is then related to the ratio of the system stiffnesses.

$$\frac{S_{\mathrm{eq,flat}}}{S_{\mathrm{eq,fiber}}} = \frac{F_{\mathrm{eq,fiber}}}{F_{\mathrm{eq,flat}}}. \tag{16}$$

Given this relationship, the reduced modulus calculated using the Oliver–Pharr method can be corrected for the finite curvature of

the substrate using a ratio of the unloading stiffnesses calculated for the equivalent sphere indentation case of interest.

$$E_{r,\text{fiber}} = E_r\left(\frac{S_{\text{eq,flat}}}{S_{\text{eq,fiber}}}\right). \quad (17)$$

The traditional (flat substrate) analysis method underestimates the actual elastic modulus of the fibers in this study. The magnitude of the error is a function of penetration depth and fiber radius, and was largest (~4%) at the deepest penetration depth (~150 nm) on the smallest (2.5 μm radius) fibers based on an implementation of the above analytical model in Matlab (2007 release). Because we are concerned with subtle, depth-dependent variations in mechanical properties, the reduced modulus and hardness values measured in this study using nanoindentation will be corrected using this equivalent spherical indenter approach by establishing correction factors from the ratio of the sample stiffnesses and projected contact areas for a given unloading curve.

3. Experimental

The materials examined in this study included three basaltic glasses and one E-glass. Basalt RW was a commercially manufactured stone wool, while Basalt Ob and Ob2 were both made in the laboratory by melting crushed raw basalt stones that were collected at different locations. The E-glass was a commercial calcium boroaluminosilicate composition. All of the samples were first melted in a Pt/Rh crucible for 3 h at 1500 °C and subsequently quenched in water. The bulk glass samples were then reheated and melted for 2 h at 1500 °C. The molten material was then cast on a brass plate and placed into an annealing furnace at the glass transition temperature, T_g, in a normal (i.e., ambient) atmosphere. Finally, the material was cooled to room temperature over 12 h. Before indentation, the samples were cut to size with a diamond saw (typical sample areas were ~1 cm^2). Residues from the cutting fluids were then removed with successive rinsing in reagent grade acetone followed by ethanol of similar purity, and the specimens were stored in sealed plastic bags. This procedure eliminated gross organic and particulate contamination, leaving the surfaces ready for nanoindentation testing.

The wool-type samples were produced by the cascade spinning process (wheel centrifuge process) [13]. The glass was heated in a furnace for approximately 2 h at 1530 °C and then poured onto the spinning wheels. This method created wool fibers with diameters ranging from 2–20 μm (6 μm average). While the cooling rate was a function of the processing conditions and the resulting fiber diameter, the typical rates were approximately 10^6 K/s [33]. The samples were stored in sealed plastic bags until indentation.

Nanoindentation was performed on a Hysitron Inc. TriboIndenter, where the forces were applied with a two axis, electrostatically actuated transducer. The force and depth resolutions of the transducer were 1 nN and 0.04 nm, respectively with a maximum range of ~10 000 μN and 4 μm. All indentations were made with a Berkovich diamond tip. The depth dependence of the cross-sectional area of the tip was calibrated by indenting, a manufacturer-supplied, fused silica reference material with peak loads ranging from 250 μN to 3000 μN. Each load was applied 5–8 times (the lower loads had more repetitions), and the resulting force-displacement data was evaluated with the 'known' elastic properties of the reference material (using the Oliver–Pharr method) to infer the projected contact area of the Berkovich indenter as a function of penetration depth.

The glass fibers evaluated in this work were aligned on glass slides under an optical microscope with a needle attached to a micromanipulator. The fibers were mounted to the substrate slide with two tiny droplets of slow-curing epoxy glue that were positioned approximately 1–2 mm apart. Capillary action-assisted flow of the adhesive insured that the fiber was bonded directly to the substrate slide. The glass slides were placed on the nanoindenter sample plate such that the fibers were aligned with the global *x*- or *y*-axis of the instrument. The optical microscope in the TriboIndenter was used to select a position for indentation on the center of the fiber between the epoxy attachment points. The indenter tip was then used as a contact-mode atomic force microscope (AFM) to image the surface of the fiber. The position of the center of the fiber was evaluated with individual line scans of the AFM image and the location of the fiber was manually adjusted to ensure that the indents were on the center line of the fiber. The drift rates of the instrument were kept low, below 0.1 nm/s, by letting the system equilibrate after positioning of the tip. The drift rate was monitored for 60 s before each indent and a linear fit of the last 20 s of the monitoring period was used to approximate the drift rates during subsequent indentation. All indentations were made in a force-controlled mode, with a constant loading/unloading rate of 300 μN/s. A trapezoidal waveform with maximum loads between 300 μN and 3000 μN with a hold time of 3 s was employed. The 1000 μN load was used as a standard value with which all samples were indented. For each fiber at least six indents were made with each maximum load.

4. Results

Interpretation of nanoindentation data relies on reproducible loading curves that can only be realized in low drift systems with uniform samples. Without high quality data, it is impossible to draw conclusions about the materials properties and their correlations with the structure of the atomic network. Fig. 1 shows an indentation on a Basalt RW fiber (note that the whole *z*-axis scale is only 47 nm compared to 1.2 μm on the *x*- and *y*-axis, so the curvature of the fiber sample is magnified) that illustrates typical alignment and features of the indent on a fiber. The indentation is located on the center line of the fiber and free of visible pileup. Representative load-depth curves for the experiments that were conducted on the fibers and larger, cast bulk glass specimens are shown in Fig. 2. For a perfectly homogeneous, isotropic, semi-infinite specimen, the loading curves should overlap and the unloading curves should all have the same initial slope, since H and E_r are independent of depth. As demonstrated for the Basal Ob shown in Fig. 2, the reproducibility of the loading curves is very good both for the bulk and the fiber glass. The slight variation observed in the fiber case is associated with the challenges of the sample geometry. With the quality of the data established, we will now review the results of the nanoindentation of *E*- and Basaltic glass fibers and bulk specimens.

4.1. Bulk glass samples

Bulk glass samples of the Basalt Ob and E-glass compositions were prepared to provide bulk reference data for the two glass systems used in the study. Indentation was performed on the melt surfaces of the samples without further treatment. Fig. 3 shows H and E_r as a function of indentation depth for the two bulk glasses. Indentation depths range from 30 nm to 140 nm with loads between 300 μN and 3000 μN. At depths larger than approximately 80 nm both H and E_r were nearly constant for both glasses, indicating that the average glass structure was homogenous below the top 80 nm layer. The difference between the upper 80 nm and the deeper bulk was larger for Basalt Ob than for E-glass, and at all depths both H and E_r were higher in the Basalt Ob than in the E-glass sample. The average bulk values for H and E_r were 8.6 GPa ± 3.5% and 90.3 GPa ± 3.3% for Basalt Ob and

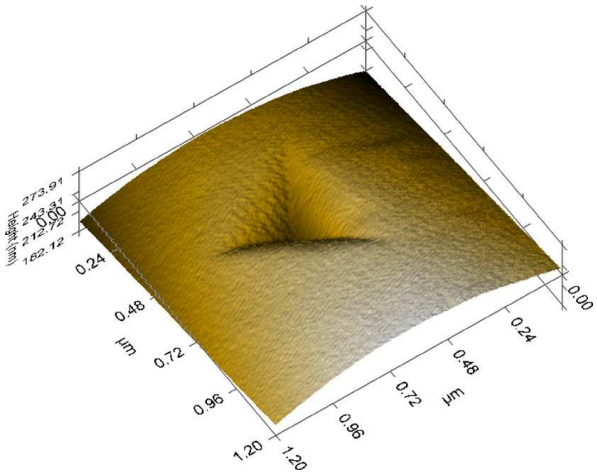

Fig. 1. Indentation on a fiber surface, the image is produced by using the nanoindentation tip as an AFM tip. The indentation load is 1000 μN. Note that the *z*-axis range is approximately 90 nm while the *x*- and *y*-axis ranges are 1.2 μm.

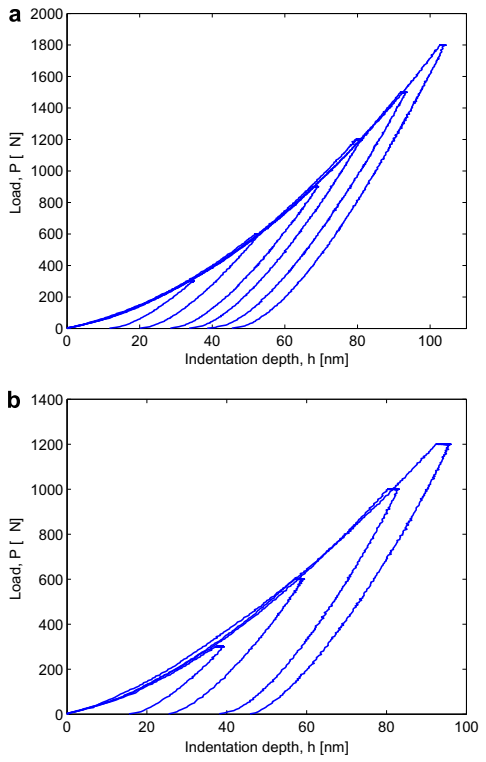

Fig. 2. Load-depth curves of indentations with various loads in (a) bulk glass and (b) fiber glass, showing the reproducibility of the upload curve for both materials.

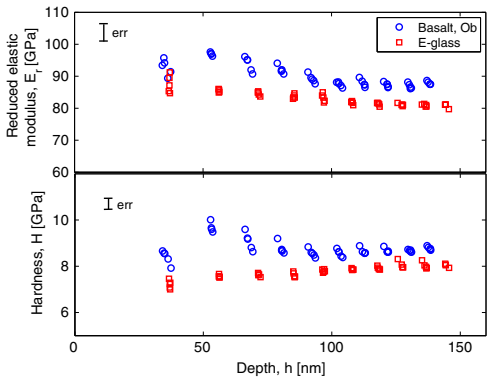

Fig. 3. Reduced elastic modulus (E_r) and hardness (H) of the bulk glasses, Basalt Ob and E-glass, as a function of indentation depth.

7.6 GPa ± 4.9% and 84.1 GPa ± 3.6% for E-glass respectively. These average values were determined from indentations deeper than 80 nm to avoid any effect of the surface. The information from the shallowest indentations (~30 nm) should be taken with care as the tip area function was not calibrated for penetrations shallower than 30 nm.

4.2. Fiber samples

Indentations with various peak loads were performed on fibers to determine the depth dependence of H and E_r. Loads only up to 1200 μN were used, and thus the resulting indentation depths were only up to ~110 nm. Shallower indentations were used to minimize the effect of the fiber curvature on the measurements. Fig. 4 shows H and E_r for the wool fiber samples as a function of maximum indentation depth. The indentations shown for each

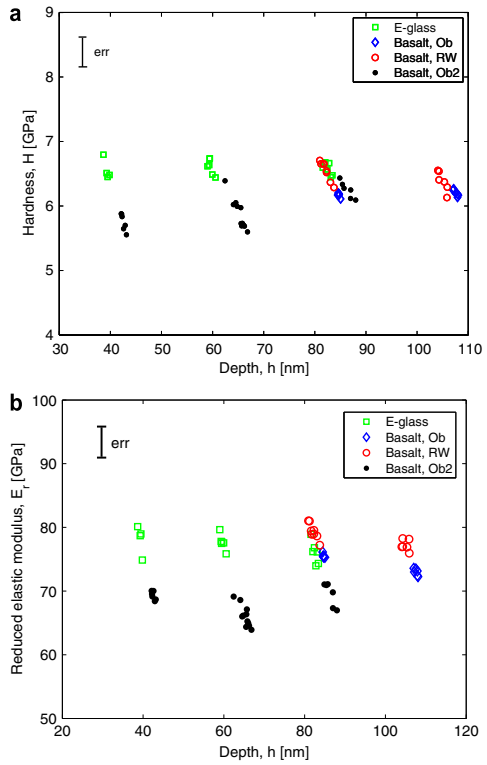

Fig. 4. (a) Hardness (H) and (b) reduced elastic modulus (E_r) of all wool fiber compositions, measured by indenting with increasing maximum load from 300 μN to 1200 μN. Each point represents a single indentation.

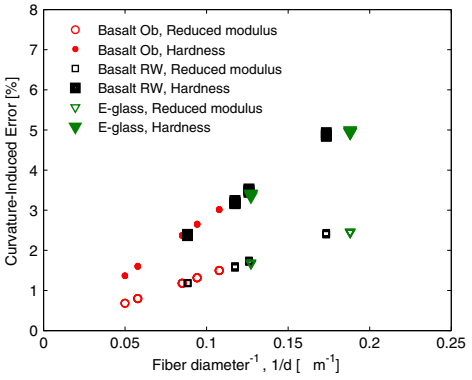

Fig. 5. Percentage error in reduced elastic modulus and hardness caused by ignoring the curvature of the fiber surface. The magnitude of the error was approximated by the equivalent sphere method.

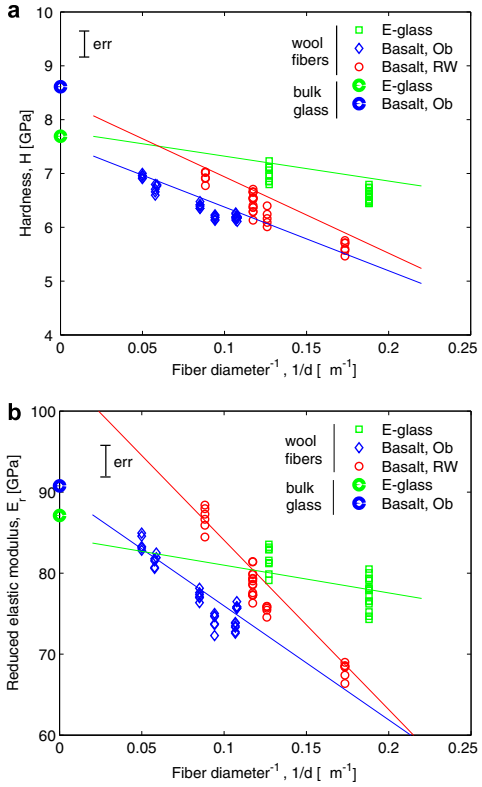

Fig. 6. Variation of (a) hardness (H) and (b) reduced elastic modulus (E_r) with fiber diameter, shown as a function of the inverse of the fiber diameter ($1/d$). The bulk glass values for E-glass and Basalt Ob are included at $1/d = 0$. All indentations are made with the maximum load of 1000 μN. The solid lines indicate a linear fit through the mean values of the hardness and reduced elastic modulus results after the correction for fiber curvature with the equivalent sphere model. The curvature correction has a negligible effect on the magnitude or the trends in the data.

composition were made on the same fiber to avoid effects caused by changes in fiber diameter. The scatter in the measured points in glasses E-glass, Basalt Ob and Basalt RW were mainly caused by the operator, as it was very challenging to precisely align the fiber axis and the indenter tip. Only indents closer than ±0.4 μm to the center line of the long axis of the fiber were included in the analysis. Similarly, the Basalt Ob2 indentations were generally more misaligned, so the H and E_r values were systematically lower. Taking into account the typical spread of the data, the general observation for H and E_r was that they were constant with indentation depth. The measured values exhibited a maximum variation of 7% for each composition and fiber diameter within the indented depth range.

Fibers with different diameters were measured for all compositions. The error associated with ignoring the finite curvature of the fiber surface for each indent was approximated with the previously described equivalent sphere method. As shown in Fig. 5, the error in reduced elastic modulus was largest (~2.5%) for the smallest fiber diameters. Similarly, the largest error in the measured hardness due to the flat substrate approximation was ~5.25%. The

effect of fiber diameter, i.e. fictive temperature of the glass, on both hardness and reduced elastic modulus can be seen in Fig. 6. Here both H and E_r determined using the Oliver–Pharr analysis method are plotted as functions of the inverse fiber diameter. This representation of the results allows for a direct comparison between the bulk and fiber glasses. The solid trend lines in the figure were determined by a linear regression of the mean values of the curvature-corrected hardness and reduced modulus of the fibers. It is important to note that the curvature-induced errors are small and do not significantly affect the magnitude of the measured values or the trends in the data.

5. Discussion

Macroscopic specimens of basaltic and E-glasses were used in this work to establish the baseline nanomechanical properties of the surfaces of the materials. This direct comparison of the large, cast samples to the micron-scale fibers allowed us to differentiate between trends that were a byproduct of the chemistry of the systems and those that were associated with fictive temperature effects. Generally-accepted values for hardness and elastic modulus are 5.6 GPa and 80 GPa for E-glass [34]. Similar experiments on basaltic glasses have established that the hardness is typically 7–7.7 GPa and the elastic modulus is 90–100 GPa [35–37]. While these values were derived from experiments that probed a relatively large volume of the material, they mirrored the trends observed in the nanoindentation experiments described in this work; i.e. E-glass had a lower H and E_r than basaltic glass. As expected, the near-surface region of the basaltic and E-glasses exhibited properties that were different than those measured at large penetration depths (Fig. 3). The observed variation in H and E_r in the experiments with penetration depths less than 80 nm can be related to structure/composition gradients or surface layers originating in the processing, and/or to an indentation size effect, ISE [38–40]. Given the similarities in structure of the basaltic and E-glass, one would expect to observe similar behavior if an indentation size effect was the origin of an elevated hardness for shallow penetration depths. Since the hardness values in the upper layer in the basalt and the E-glass showed opposite behavior (i.e., the basaltic glass hardness increased with decreasing penetration depth, and the E-glass hardness slightly decreased as the penetration depth was reduced), the variation can be ascribed to the surface properties of the specimens rather than an ISE. Fortunately, previously published processing studies of E- and basaltic glasses can link the chemistry and structure of the glasses to the observed inhomogeneity.

An explanation for the near-surface mechanical property variations can be found in the surface chemistry of the surfaces of the two glasses. In the bulk of the basaltic glass, approximately 83% iron is primarily in the lower oxidation (i.e., Fe^{2+}) state [41,42]. In contrast, the Fe^{2+} in the outermost surface layers would have an opportunity to further oxidize during casting and annealing of the glass samples. This change in oxidation state could alter the local coordination of iron from purely tetrahedral to mixed tetra- and octahedral, where the enhanced cross-linking around the oxidized iron species would elevate the hardness and reduced elastic modulus of the glass. Similar chemical-structural arguments can be made for the reduction of the elastic and plastic deformation resistance of the E-glass surfaces. The well-known evaporation of boron-oxide from the E-glass surface could reduce the degree of cross- linking and thereby weaken the local network structure [43,44]. While the surface chemistry of the cast basaltic and E-glass specimens used in this work has not yet to been evaluated, the observed near-surface variation in mechanical properties measured with nanoindentation are consistent with changes that can be expected during processing of the materials and the absence of variations in the properties of a given fiber. In contrast, the near-surface mechanical properties of the fiber forms of the glasses were relatively uniform.

Provided that gross variations in chemistry do not occur during processing, fibers are an outstanding system for evaluating the effects of fictive temperature on the mechanical properties of silicate glasses. While the concept of the fictive temperature has been theoretically and empirically demonstrated, the correlation between glass structure and mechanical deformation is not particularly clear. In this work we have shown that the systematic variation in cooling rate that is associated with different fiber diameters has a marked effect on the mechanical behavior of the glasses (Fig. 6). Furthermore, the H and E_r of a given fiber were essentially invariant for penetration depths less than ~110 nm (Fig. 4). These interesting findings raise two critical questions about how to interpret the differences between the fiber and bulk mechanical property data. Firstly, are previous empirical and numerical modeling studies of fiber glasses and residual stress effects consistent with the (apparently) uniform fibers? Secondly, is there additional information from the instrumented indentation tests that can be used to compare the flow of silicate glass in the bulk and fiber forms?

The two bulk glasses and their corresponding fiber samples were produced from the same batches with similar melting history. Consequently, the observed differences in fiber versus bulk properties originated in the final production stage when either the fiber or bulk piece was cast or drawn from the melt. Generally, a change in the fiber diameter requires changes in both the cooling rate of the glass and the mechanical stress applied during drawing. Moreover, the non-uniform cooling rates between the surface and bulk of the fiber, and/or non-uniform stress state [45] due to a distribution of 'frozen-in' drawing-strains across the fiber, could lead to axisymmetrically-distributed variations in properties across the cylindrical fiber. In principle, both the cooling rate and mechanical stress state can modify the intrinsic structure of a glass and the state of (residual) stress in the materials. Instrumented indentation experiments conducted on an externally loaded soda-lime glass model system demonstrate that distortion of the glass network may lead to measurable changes in the elastic modulus and (to a lesser extent) the hardness [46]. However, the stresses that can be present in as-processed fibers may not be significant. For example, experiments performed on polished cross sections of fibers by Li et al. [15] showed no change in hardness or reduced modulus across the fibers' cross sections. While surprising in some respects, the invariance of properties in the fibers was consistent with FEM simulations [33] of the temperature distribution across a fiber during a drawing process. In the case of the cascade spun wool fibers in this work, the mechanical stress during production was negligible compared to stresses during continuous fiber drawing. As a result, the observations of a slight increase in H and E_r with fiber diameter (for a given peak indentation load) and the general finding that these properties were well below bulk glass values (Fig. 6) suggest that trends are strongly correlated with the cooling rate. The more open structure (and high T_f) of the rapidly-cooled wool glass was associated with lower resistance to elastic and plastic deformation. Additionally, the network structure of the fiber glasses appeared to be uniform within the first ~110 nm from the outer surface (Fig. 4). While our measurements were confined to depths less than 1/10 of the fiber diameter, cooling a homogeneous liquid by fiber drawing should not cause stratification across the fiber. As a result, we believe that the relatively uniform values for H and E_r from 80 nm to100 nm prevail deeper into the fiber.

Most analyses of instrumented indentation data are heavily focused on the unloading portion of the experiment. However, the initial loading of the specimen can be used to corroborate elastic

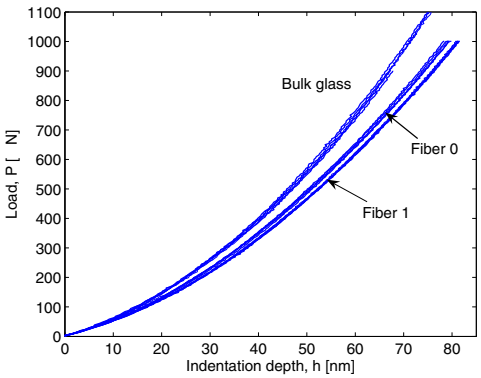

Fig. 7. Loading curves of bulk and fiber glasses of Basalt Ob. The image shows the general consistency between indentations, the typical difference between bulk glass and fiber glass loading curve slopes and even the difference between fibers of the same material but with different diameters.

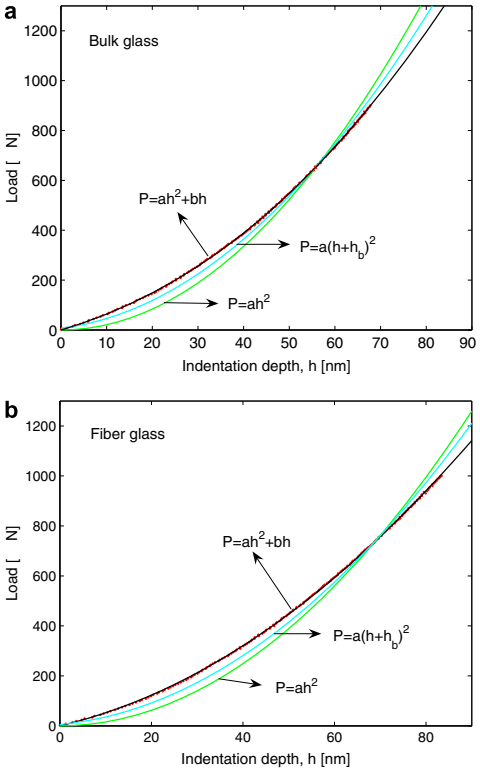

Fig. 8. Fitting the loading curve of (a) a bulk glass and (b) a fiber glass indentation with different models generally in use. The measurement is represented by the thick red dots, and the different fit models are given in the figures.

and plastic deformation trends by using energy-based concepts. The total work, W_{tot}, of an indentation is defined as the area beneath the loading curve. The total work contains contributions from the plastic work W_p (the area between the loading and unloading curves) and the elastic work W_e (the area under the unloading curve) [31]. Representative loading curves of a fiber and a bulk glass of same composition are shown in Fig. 7. The loading curves were rather sensitive to the structure of the indented material, since clear differences between fibers of same material were observed. This finding demonstrates the value of evaluating the totality of an instrumented indentation experiment. Analysis of the load-displacement curves in this work revealed that W_{tot} was smaller for the bulk than the fiber forms of the glasses. This observation was consistent with the higher hardness measured from the unloading curve stiffness using the Oliver–Pharr method. While not applied in this work, the more open network structure of the fibers could have been characterized by measuring the density or the molecular volume of the glasses [11]. In this study, the glass network structure was linked to the mechanical response via the elastic and plastic work measured during the nanoindentation process. The relative elastic and plastic works of bulk and fiber samples revealed that W_e and W_p were approximately equal in fibers whereas the W_e was comparatively larger than W_p in bulk glass. For this reason, the bulk glass had a larger elastic recovery after the indentation than fiber glass; also E_r was larger for bulk than fiber glass.

In addition to the area under the loading curve, its shape can be used to confirm that the elastic-plastic deformation behavior of the bulk and fiber forms of the glasses were different. It is generally accepted that loading curves obtained by nanoindentation with a Berkovich tip follow Eq. (5) (with the indicated depth correction). We have studied the shape of the loading curves obtained both on the bulk glass samples and the fiber samples, and found the best fit to be of the type $P = ah^2 + bh$ (Fig. 8). The constant a is analytically described elsewhere [29,30] and it is a function of H, E_r and geometrical factors. A perfect Berkovich indentation tip and a 'well behaved' material should follow $P = ah^2$. It is tempting to ascribe the bh correction factor to the curvature of the fiber surface in addition to the conventional tip non-ideality due to blunting. However, since both the bulk and fiber specimens are accurately represented by the same functional form, the bh term cannot be attributed solely to fiber curvature. Based on the Oliver–Pharr (all samples had different H and E_r values) one would expect that $a_{bulk} \neq a_{fiber}$ and $a_{fiber1} \neq a_{fiber2}$. Indeed, we have found that $a_{fiber} \approx 0.10$, $a_{bulk} \approx 0.13$ and $b_{bulk} \approx b_{fiber} \approx 4.5$ for both Basalt Ob and E-glass. Our results indicate that the details of the glass structure affect the general shape of the glass loading curves, as was also noted by Manika et al [47].

The energetic and loading curve trends detailed above can be related to the bond types in these glasses. Most of the reported nanoindentation loading curve studies were based on crystalline materials and on vitreous SiO_2 [28–30]. Microindentation studies conducted on glasses [48,49] have demonstrated that anomalous, low density glasses such as vitreous SiO_2 deform mainly due to densification. The 'normal' glasses (with intermediate densities) deform by both densification and plastic flow, while high density glasses exhibit only plastic flow. The glasses used in this study belong to the group with high density that deform mainly due to plastic flow. In the fiber-glass structure, more of the interatomic bonds are displaced from their 'equilibrium' distance or local coordination state, and thus, are more easily plastically deformed and should exhibit more densification than the bulk form. The relative contributions of densification and shear flow to the plastic deformation process in this work were established by quantifying the shape of the indentation site. Analyses of transverse sections of the in-situ AFM images from representative indents the bulk and

fiber glasses were used to determine the extent of pile-up in the basaltic and E-glasses. Previous studies have shown that pile-up in silicate glasses can be directly linked to the underlying deformation mechanisms and glass structures [50]. In the case of the fibers, visible pileup formation started to occur when the indentation load exceeded 1000–1200 μN. Load levels approaching 1500 μN were required to induce measurable pile-up in the bulk samples. In addition to the delayed onset of pile-up in the bulk glasses, the relative magnitude with respect to penetration depth was also lower than was observed in the fiber forms. These observations were consistent with the notion that the higher cooling rates of the fibers were correlated with a more open network structure and higher fictive temperatures.

6. Conclusions

In spite of the experimental challenges that were expected, this work showed that nanoindentation can be used as a tool for measuring hardness (H) and reduced elastic modulus (E_r) of glass fibers, including melt spun wool fiber. More importantly, the nanoindentation data demonstrated that the more open network structure associated with higher fictive temperature fibers was correlated with the elastic and plastic deformation behavior of basaltic and E-glasses. Irrespective of the glass composition, the hardness and the reduced elastic modulus were lower for a glass fiber than a bulk glass sample. This was related to the differences in the intrinsic structure of glasses that was caused by the difference between the cooling rates of the bulk and fiber glasses. The higher cooling rate of the fibers resulted in a more open structure that had lower H and E_r values. Finally, the more open structure of the fiber glass was correlated with a larger amount of plastic flow that was driven by a small degree of shear plastic flow.

7. Acknowledgements

This work was supported by Rockwool International and the NSF International Materials Institute on New Functionality on Glasses (DMR-0409588/540792-8001). This publication was also supported by the Pennsylvania State University Materials Research Institute NanoFabrication Network and the National Science Foundation Cooperative Agreement No. 0335765, National Nanotechnology Infrastructure Network, with Cornell University.

References

[1] K.L. Loewenstein, J. Dowd, Glass Technol. 9 (6) (1968) 164.
[2] W.J. Kroenke, J. Am. Ceram. Soc. 49 (9) (1966) 508.
[3] C.R. Kurkjian, P.K. Gupta, R.K. Brow, N. Lower, J. Non-Cryst. Solids 316 (2003) 114.
[4] N.P. Lower, R.K. Brow, C.R. Kurkjian, J. Non-Cryst. Solids 344 (2004) 17.
[5] A.A. Griffith, Philos. Trans. Roy. Soc. A 221 (1921) 163.
[6] G.M. Bartenev, L.K. Izmailova, Sov. Phys.-Sol. State 6 (4) (1964) 920.
[7] G.M. Bartenev, The Structure and Mechanical Properties of Inorganic Glasses, Translated by F.F. Jaray, Wolters-Noordhoff Publishing, Groningen, 1970.
[8] V.V. Gur'ev, E.I. Neproshin, G.E. Mostovoi, Glass Ceram. 58 (1–2) (2001) 62.
[9] I. Wojnárovits, Glass Sci. Technol. 68 (11) (1995) 360.
[10] J.F. Bauer, Int. Nonwovens J. 13 (4) (2004) 2.
[11] C. Shelby, Introduction to Glass Science and Technology, The Royal Society of Chemistry, Cambridge, UK, 1997.
[12] M. Ya, J. Deubener, Y.Z. Yue, J. Am. Ceram. Soc. 91 (3) (2008) 745.
[13] Y.Z. Yue, R. von der Ohe, S.L. Jensen, J. Chem. Phys. 120 (2004) 8053.
[14] C.W. Axten, J.F. Bauer, P.M. Boymel, J.D. Copham, R.N. Cunningham, O. Kamstrup, A. Koenig, J.L. Konzen, I. Ohberg, C. Roe, J. Sacks, T.M. Singh, W. Wolf, Man-made Vitreous Fibers : Nomenclature, Chemistry, and Physical Properties, TIMA, Inc., North American Insulation Manufacturers' Association, 1993.
[15] X. Li, B. Bhushan, P.B. McGinnis, Mater. Lett. 29 (1996) 215.
[16] X. Li, H. Gao, C.J. Murphy, K.K. Caswell, Nanoletters 3 (11) (2003) 1495.
[17] M. Wang, H-J. Jin, D.L. Kaplan, G.C. Rutledge, Marcomolecules 37 (2004) 6856.
[18] H. Ni, X. Li, H. Gao, Appl. Phys. Lett. 88 (2006) 043108.
[19] E.P.S. Tan, C.T. Lim, Appl. Phys. Lett. 87 (12) (2005) 123106.
[20] G. Feng, W.D. Nix, Y. Yoon, C.J. Lee, J. Appl. Phys. 99 (2006) 074304.
[21] W.C. Oliver, G.M. Pharr, J. Mater. Res. 7 (6) (1992) 1564.
[22] G.M. Pharr, A. Bolshakov, J. Mater. Res. 17 (10) (2002) 2660.
[23] C.A. Klein, Mat. Res. Bull. 27 (12) (1992) 1407.
[24] M.H. Grimsditch, A.K. Ramdas, Phys. Rev. B 11 (8) (1975) 3139.
[25] C.K. Hruska, J. Appl. Phys. 72 (6) (1992).
[26] H.J. McSkimin, J.P. Andreatch, P. Glynn, J. Appl. Phys. 43 (3) (1972) 985.
[27] E.S. Zouboulis, M. Grimsditch, A.K. Ramdas, S. Rodriguez, Phys. Rev. B 57 (5) (1998) 2889.
[28] S.V. Hainsworth, H.W. Chandler, T.F. Page, J. Mater. Res. 11 (8) (1996) 1987.
[29] J. Malzbender, G. de With, J. den Toonder, J. Mater. Res. 15 (5) (2000) 1209.
[30] M. Troyon, M. Martin, Appl. Phys. Lett. 83 (5) (2003).
[31] A.C. Fischer-Cripps (Ed.), Nanoindentation Mechanical Engineering Series, 2nd Ed., Springer, New York, 2004.
[32] A.P. Boresi, R.P. Schmidt (Eds.), Advanced Mechanics of Materials, 6th Ed., John Wiley, New York, 2003. p. 681.
[33] R. von der Ohe, PhD thesis, Aalborg University, Denmark, 2003.
[34] J. Sehgal, Y. Nakao, H. Takahashi, S. Ito, J. Mater. Sci. Lett. 14 (1995) 167.
[35] M. Jensen, M. M. Smedskjær, M. Estrup, M. Kristjansson, N. Lonnroth, Y. Z. Yue, Eur. J. Glass Sci. Technol. Part A, submitted for publication.
[36] N. Lonnroth, Y. Z. Yue, Glass Technol. Eur. J. Glass Sci. Technol. Part A, in press.
[37] S.E. Artemenko, Fiber Chem. 35 (3) (2003) 226.
[38] H. Meinhard, P. Grau, G. Berg, S. Mosch, Glass Sci. Technol. 70 (11) (1997) 333.
[39] Z.H. Li, J.H. Gong, Z.J. Peng, H.Z. Miao, Key Eng. Mat. 280–283 (2005) 1659.
[40] S. Sebastian, M.A. Khadar, J. Mater. Sci. 40 (7) (2005) 1655.
[41] D.J.M. Burkhard, J. Petrol. 4 (3) (2001) 507.
[42] D.J.M. Burkhard, T. Scherer, J. Non-Cryst. Solids 352 (2006) 241.
[43] M.N. Palmisiano, A.L. Boehman, C.G. Pantano, J. Am. Ceram. Soc. 83 (10) (2000) 2423.
[44] G.P. Lamaze, H.H. Chen-Mayer, K.K. Soni, Appl. Surf. Sci. 238 (2004) 108.
[45] T.Y. Tsui, W.C. Oliver, G.M. Pharr, J. Mater. Res. 11 (3) (1996) 752.
[46] K.O. Kese, Z.C. Li, B. Bergman, J. Mater. Res. 19 (10) (2004) 3109.
[47] I. Manika, J. Maniks, Acta Mater. 54 (2006) 2049.
[48] C.R. Kurkjian, G.W. Kammlott, M.M. Chaudhri, J. Am. Ceram. Soc. 78 (1995) 737.
[49] J. Sehgal, S. Ito, J. Non-Cryst. Solids 253 (1999) 127.
[50] J.A. Howell, J.R. Hellmann, C.L. Muhlstein, Mater. Lett 62 (2008) 2140.

Article IV

Glass Technol.: Eur. J. Glass Sci. Technol. A, June 2009, **50** (3),165–173

Influence of chemical composition on the physical properties of basaltic glasses

N. Lonnroth & Y. Z. Yue[1]

Section of Chemistry, Aalborg University, Sohngaardsholmsvej 57, 9000 Aalborg, Denmark

Manuscript received 7 February 2007
Revision received 30 November 2008
Manuscript accepted 3 December 2008

The sensitivity of physical properties of a basaltic glass to compositional variations is explored and demonstrated by means of mechanical, rheological and thermo-analytical methods. Addition of MgO increases the melt fragility, the glass hardness, Young's modulus and the glass transition temperature (T_g), whereas addition of Na_2O decreases glass hardness, Young's modulus and T_g. Addition of Al_2O_3 decreases melt fragility, T_g and Young's modulus. The origin of the observed changes of the physical properties has been clarified in terms of the random network theory.

1. Introduction

Basalt is an abundant and important raw material that can be used for making vitrified or partially vitrified materials with a number of technological applications. Glasses of basaltic composition have a wide range of applications, in fibrous form from insulation wool[1] to filtration media[2] and as reinforcement[3] in glassy, ceramic or plastic media and in bulk glass form as a glass-ceramic coating[4–6] or in the construction industry[7–8] where slag waste is re-used. From a general point of view the chemical compositions of naturally occurring basalts have had a large effect on how our environment looks like nowadays, as the shapes of volcanoes are determined by the viscous behaviour of lava which is closely connected to its composition. Several studies on viscosity and crystallisation have been conducted on basaltic compositions[9–14] as these issues are relevant both to earth sciences and glass-ceramic production. When the glass itself is used or developed into a new application, e.g. glass ceramic, it is important to know how the various physical properties of the material are affected by variations in the chemical composition. This gives the possibility of optimising the chemical composition with respect to physical properties, production conditions and production cost.

A basaltic glass is an iron containing alkaline earth aluminosilicate glass including other oxides in minor amounts. Thus, due to the compositional complexity it is not easy to give a simple structural picture of the basaltic glasses. All of the compositions studied here belong to the metaluminous system, where $[Na_2O+K_2O+FeO]<[Fe_2O_3+Al_2O_3]<[MgO+CaO+Na_2O+K_2O+FeO]$ (in mol%).[15] This means that there are sufficient modifiers to act as charge balancing ions for Al- and Fe-tetrahedra. In the studied glasses there are 2·45–4·77 alkali and alkaline earth cations per intermediate ion, and thus, all Al^{3+} and Fe^{3+} ions are tetrahedrally coordinated. Therefore, the structural network is composed of Si-, Al- and Fe-tetrahedra charge balanced by some of the alkali and alkaline earth ions. The nonbridging oxygen ions of those tetrahedra are charge compensated by the excess of the alkali and alkaline earth cations, i.e. the so-called network modifiers.[e.g. 16–18] The composition of the base glass system studied in this work is close to that of natural basalts. Some stone wool products are based on this composition. In this work the focus is placed on detecting the responses of mechanical, thermal and rheological properties to systematic changes in chemical composition. The origin of those responses will be explored.

2. Experimental

The glasses examined in this study were all prepared from a glass composition used in insulation wool production (see Table 1). The base glass was taken from the production line before fiberising. Intentional variations in the composition of the glasses were made by increasing the MgO, Al_2O_3 and Na_2O content in the base glass batch, respectively, and this led to the three glass series: Mg-, Al- and Na-series (see Table 1). MgO and Al_2O_3 were added as oxides while Na_2O was added in the form of Na_2CO_3. All chemicals used were of analytical grade. The glass powders were mixed thoroughly before melting. All samples were melted twice in a Pt/Rh crucible in a furnace, first for 4 h at 1500°C followed by quenching in water. Then the glasses were reheated and melted for 2 h at 1500°C, cast onto a brass plate into bars, placed into an annealing furnace at the approximate glass transition temperature (T_g) and naturally cooled to room temperature. The vitreous nature of the samples was confirmed by XRD measurements. The glass bars were cut into pieces, the geometry of which depended

* Corresponding author. Email: yy@bio.aau.dk

Table 1. Chemical composition in mol% of studied glasses measured by XRF. Glass 2 is the base glass in the Al- and Na-series. Measured density and the calculated NBO/T (nonbridging oxygens per tetrahedra) ratio for each glass are also given

	Mg-series				*Al-series*			*Na-series*	
No.	*1*	**2**	*3*	*4*	*5*	*6*	*7*	*8*	*9*
SiO_2	47·82	**44·49**	41·95	39·11	43·39	42·71	41·93	43·12	42·32
Na_2O	1·58	**1·43**	1·40	1·37	1·46	1·46	1·48	3·89	5·74
K_2O	0·69	**0·67**	0·59	0·58	0·62	0·62	0·63	0·67	0·67
MgO	8·12	**14·54**	19·70	24·96	13·99	14·01	13·98	14·22	14·07
CaO	24·86	**23·10**	21·65	20·19	22·49	22·07	21·70	22·65	22·11
Al_2O_3	11·63	**10·90**	10·20	9·50	13·32	14·55	15·66	10·46	10·16
Fe_2O_3	1·20	**1·11**	1·03	0·98	1·08	1·04	1·05	1·14	1·11
FeO	3·61	**3·32**	3·09	2·93	3·24	3·13	3·17	3·43	3·34
TiO_2	0·25	**0·21**	0·21	0·20	0·22	0·22	0·22	0·24	0·24
P_2O_5	0·23	**0·22**	0·17	0·17	0·18	0·18	0·18	0·18	0·22
NBO/T	0·66	**0·85**	1·03	1·24	0·71	0·65	0·60	0·95	1·00
ρ	2·83	**2·87**	2·90	2·92	2·86	2·86	2·85	2·86	2·84

on the type of measurement being made.

The density of the samples was determined by measuring sample mass and sample volume with a helium pychnometer. Young's modulus, Poisson's ratio and the shear modulus were determined from the longitudinal and transverse sound velocities in the samples. The sound velocities were determined by measuring the time it takes for an ultrasound wave of known wavelength to travel a known length of sample material. The composition of the glass samples was measured using a x-ray fluorescence spectrometer, (Philips 1404) (see Table 1). The FeO/Fe_2O_3 ratio was estimated from Mössbauer measurements on a basalt glass with a similar melting history and composition as the ones studied here. The NBO/T ratio of the glasses (Table 1) was calculated based on the measured composition of the samples. The Mg-series consists of glasses 1–4 where the amount of MgO was increased from 8·12 to 24·96 mol%. In the other series glass 2 was used as the base glass to which substitutions were made. So the Al-series consists of glasses 2, 5, 6 and 7 where the Al_2O_3 content was increased from 10·90 to 15·66 mol%, and the Na-series consists of glasses 2, 8 and 9 where Na_2O was increased from 1·43 to 5·74 mol%.

Differential scanning calorimetry (DSC) measurements, using a simultaneous thermal analyser (Netzsch STA 449C Jupiter), were made on samples of approximately 30 mg mass. The glass transition temperature (T_g) was measured using a 10 K/min heating rate and determined from the second upscan to ensure that the sample had been cooled at the same rate as the heating rate.[19] The crystallisation onset temperature (T_c) and the liquidus temperature (T_l) were determined from 20 K/min heating rate scans.

Hardness was measured using a Duramin 5 (Struers) microhardness tester with a Vickers indenter. Indentations were performed with loads of 1·96, 2·94 and 4·91 N to note the effect of load. The hold time in all indentations was 5 s at maximum load. The transverse cut sample surfaces were polished by 3 μm diamond suspension before indentation, and indentation was performed across the sample. For each load and sample, 20 to 30 indents were made and both diagonals of the indent and the crack sizes were measured. Vickers hardness (H_V) was determined from the average indent diagonal length a using

$$H_V = \alpha_0 \frac{P}{a^2} \tag{1}$$

where α_0 is the indenter geometry constant (1·854 for a Vickers indenter) and P is the load. The indentation fracture toughness (K_{Ic}) of glass was determined from the half of the mean size of the two radial cracks, c, using[20–21]

$$K_{Ic} = \chi \frac{P}{c^{3/2}} \tag{2}$$

where χ is a function of the elasto-plastic ratio E/H_V, where E is Young's modulus. χ is given by

$$\chi = 0{\cdot}018\sqrt{\frac{E}{H_V}} \tag{3}$$

Brittleness of glasses can also be determined from indentation measurements. At small loads plastic deformation of the sample occurs, which is assessed by the hardness of the material, whereas at large loads brittle fracture of the sample will occur, which is assessed by the fracture toughness of the material. Thus Lawn & Marshall[22] have defined brittleness as

$$B = \frac{H_V}{K_{Ic}} \tag{4}$$

Sehgal and co-workers[21,23] have more recently shown that brittleness can be evaluated using

$$B = \gamma P^{1/4}\left(\frac{c}{a}\right)^{3/2} \tag{5}$$

where γ is a function of Young's modulus and hardness given by

$$\gamma = 31{\cdot}3\times10^{-3}H_V^{3/4}E^{1/2} \tag{6}$$

An approximate value of $\gamma = 2{\cdot}39\ N^{1/4}\ \mu m^{-1/4}$ was given by Sehgal & Ito,[23] with an error range of ±5% for typical inorganic glasses. In this study the values calculated for γ using Equation (6) were within ±2% of $2{\cdot}39\ N^{1/4}\ \mu m^{-1/4}$ and thus this fixed value was used in the analysis.

High temperature viscosity was determined using a concentric cylinder rotational viscometer,[24] with a Pt/Rh crucible and spindle. Measurements were carried out by controlling the speed and torque of the spindle and thus by knowing the geometry of the system the viscosity could be determined. Measurements were started at 1450°C and continued downward at 25°C intervals until crystallisation occurred. For glass 4 measurements were started at 1500°C due to the high T_l of the crystals obtained from this glass composition, so that the same number of data points

could be acquired for this glass as were obtained for the other glasses.

3. Results and discussion

3.1. Influence of glass structure on mechanical properties

The effect of compositional changes on the number of nonbridging oxygens (NBO) per tetrahedra is shown in Figure 1 and also given in Table 1. Increases in MgO and Na_2O led to an increased number of NBOs and an increase in Al_2O_3 decreased the number of NBOs. All R^{2+} ions (Mg, Ca) require two NBOs in their vicinity, where R^+ ions (Na, K) need only one NBO for charge neutrality. On a molar basis, additions of MgO and Na_2O produce both the same number of NBOs, two per added oxygen. Since Al_2O_3 provides only 1·5 oxygen per tetrahedron, the oxygens in the alkali (R_2O) and alkaline earth (RO) oxides are used in the formation of the aluminium–oxygen tetrahedra and are not available for the formation of NBOs. This has the net effect that each added Al^{3+} ion converts one NBO to one bridging oxygen (BO). This is visible in the Table 1, as NBO/T decreases with increasing Al_2O_3.

3.1.1. Hardness and density

The different indentation loads (1·96, 2·94 and 4·91 N) statistically gave the same hardness results. The smallest amount of cracking was observed at the lowest load of 1·96 N and the number as well as the length of the cracks increased with increasing load. Cracking causes release of internal energy within the material, and hence, effects the measured hardness value. To obtain the most accurate hardness values for these materials, the given hardnesses were calculated using only the 1·96 N indentations. Fracture toughness was determined from the length of the median radial cracks *c*. Only the highest load of 4·91 N always produced fully developed median radial cracks for all the samples, and thus fracture toughness was determined only from the cracks around 4·91 N indentations. Figure 2 shows H_V and K_{Ic} for each glass series as a function of molar content of the various oxides. The H_V and K_{Ic} values with error ranges are given in Table 2. Hardness is related to the average value of bond strengths in the material[25] in a given area, and thus it can be viewed as an indication of the strength of the network structure itself. An effort to look at hardness as a function of a network property, the density, is shown in Figure 3. Although there is a tendency for hardness to increase with density there is no real correlation between the values. The influences of increases in content of some selected oxides on the hardness and density is discussed in the following sections.

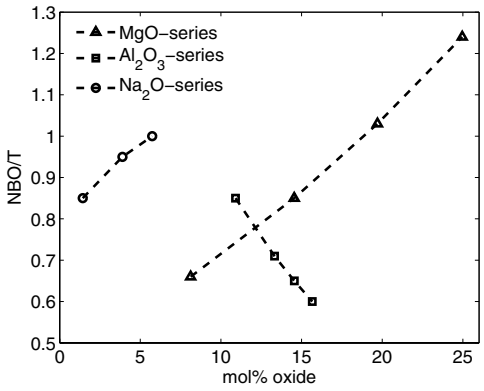

Figure 1. Change of NBO/T with substitution of MgO, Al_2O_3 and Na_2O in the respective series.

1. Addition of MgO and Na_2O

As alkaline earth ions (Mg, Ca) need two NBOs in their vicinity, a much stronger network linkage is provided at alkaline earth sites than at the alkali sites. So the R^{2+} ions are more tightly bound at their sites and are less mobile than R^+ ions that are bound to their sites by only one NBO. With this in mind, it is understandable that for the Mg-series hardness and Young's modulus increase as more MgO is added, since Mg^{2+} ions are well bound to their sites. For the Na-series the increase in NBOs and the single bond of Na^+ to the network creates a loose and open network. Thus in the Na-series H_V decreases drastically with increasing sodium content and the glass with the highest Na_2O content (glass 9) has the lowest brittleness of all glasses. Figure 4 shows B for all of the glasses as a function of density in the 'brittleness plot'. Compared to other glasses studied with respect to B, the glasses studied here are all dense and brittle.[23,26–27] The fracture toughness stays fairly constant in the both series. When discussing structure and density of glasses the type of the ions present has to be taken into account. Na^+ is lighter than Mg^{2+}. This mass difference, together with the looser Na^+–NBO bonds, makes the glasses with larger Na_2O contents less dense. In contrast the density increases with increasing MgO content.

2. Addition of Al_2O_3

Addition of Al_2O_3 leads to an increase in the number of alumina tetrahedra between the silica tetrahedra in the glass network as long as the total number of alkali and alkaline earth ions is higher than the number of Al^{3+} ions, which holds for all the Al-series glasses. No large change in the density of these glasses was observed and the small decrease of ρ can be related to the small mass difference in Al^{3+} and Si^{4+} ions. The hardness and fracture toughness were also relatively little affected by the increase in Al_2O_3, although a slight upward trend was observed in K_{Ic}. Generally,

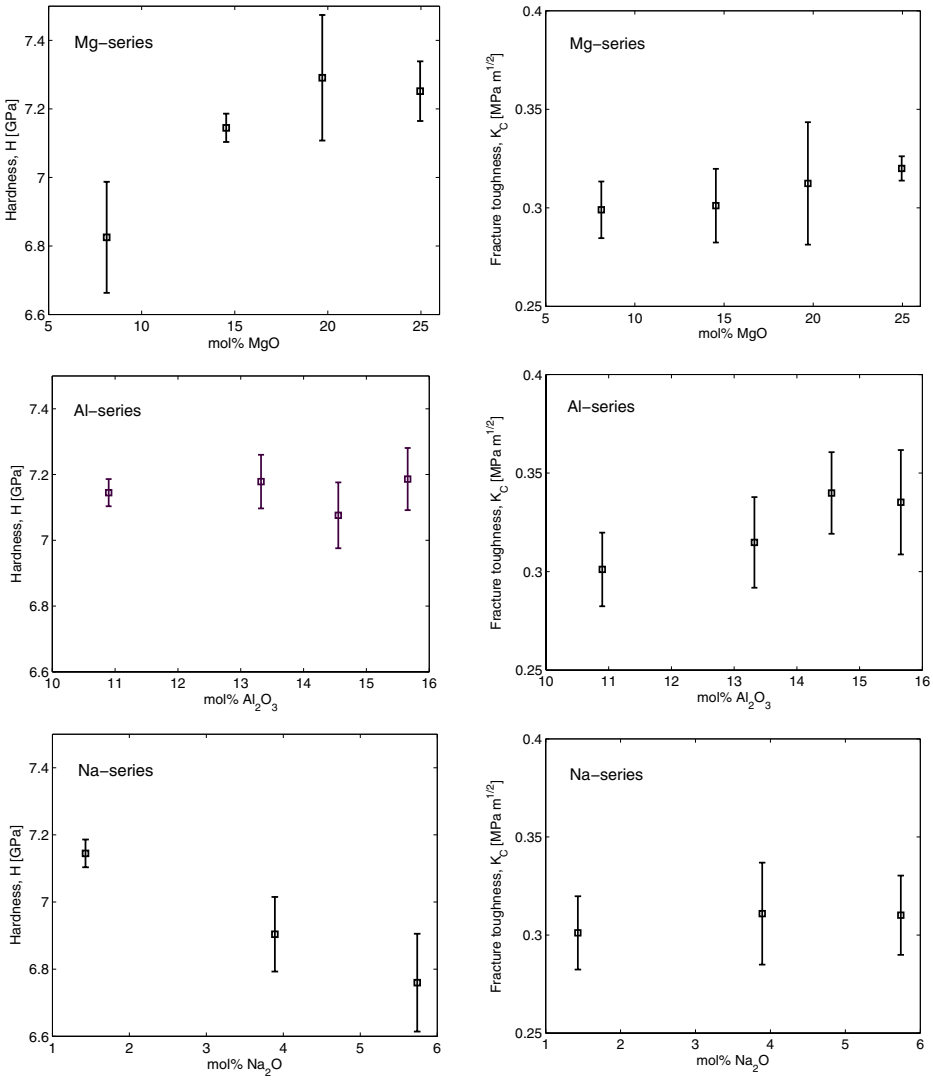

Figure 2. Hardness (H_V) and fracture toughness (K_{Ic}) for each series as a function of mol% of the respective oxide addition.

Table 2. Mechanical properties of the glasses. Young's modulus was derived from transverse and longitudinal sound velocities in the glasses, H_V and K_{Ic} were determined from indentation measurements and brittleness B *was determined using Equation (5)*

Glass	*E* (GPa)	*H* (GPa)	stdev (H)	K_{Ic} (MPa m$^{1/2}$)	stdev (K_{Ic})	B (μm$^{-1/2}$)	stdev (*B*)
1	96·01	6·83	0·16	0·30	0·01	8·0	0·4
2	99·79	7·14	0·04	0·30	0·02	8·2	0·6
3	103·81	7·29	0·18	0·31	0·03	8·0	0·8
4	106·30	7·25	0·09	0·32	0·01	8·0	0·2
5	100·81	7·18	0·08	0·31	0·02	7·9	0·6
6	101·75	7·08	0·10	0·34	0·02	7·3	0·5
7	102·23	7·19	0·09	0·34	0·03	7·4	0·5
8	98·75	6·90	0·11	0·31	0·03	7·8	0·6
9	97·03	6·76	0·14	0·31	0·02	7·7	0·5

the strength of the main network is not altered by the increasing number of alumina tetrahedra. The observed decrease in brittleness with Al_2O_3 addition (Figure 4) is a combined consequence of the changes in H_V and K_{Ic}. Generally in this density range brittleness should decrease with density.[26]

3.1.2. Elasticity

The elastic modulus of glass is highly dependent on the structure of the network. The latter is determined by characteristics of individual constituents, e.g. cationic field strength and coordination number, which govern the ionic packing density and the average bond

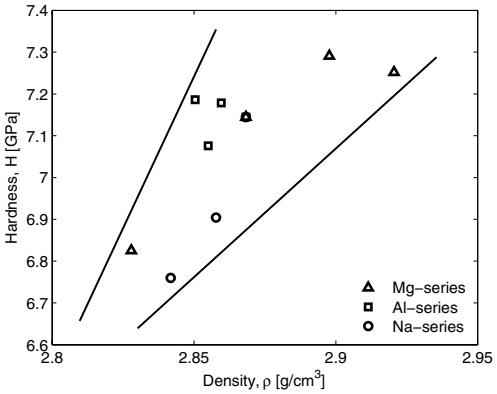

Figure 3. Hardness of all the investigated glasses as a function of density. The lines are guides for the eye

strength.[28] Contrary to what Lin and Liu[29] found the highest elastic modulus in our glasses is the one with highest SiO_2 content. Further in their study of basaltic glasses they observed an increasing trend in Young's modulus with increasing NBO/T. In the Al- and Na-series tested here the Young's modulus decreases with increasing NBO/T and for the Mg-series E is increasing (Figure 5). In pure sodium aluminosilicate glasses Yoshida *et al*[30] find that both hardness and Young's modulus increase with the Al_2O_3/Na_2O ratio. Similar to their study, we also varied the molar ratio of intermediate ions to modifier ions, i.e. $[Al_2O_3+Fe_2O_3]/[MgO+CaO+Na_2O+K_2O]$ and observed the responses of both hardness and Young's modulus. The intermediate/modifier ratio varies from 0·24–0·41 for all glass series studied in this work. However, the correlation found by Yoshida *et al* was not observed. This implies that no simple, general relation exists between composition and mechanical properties, which would be valid for different glass systems.

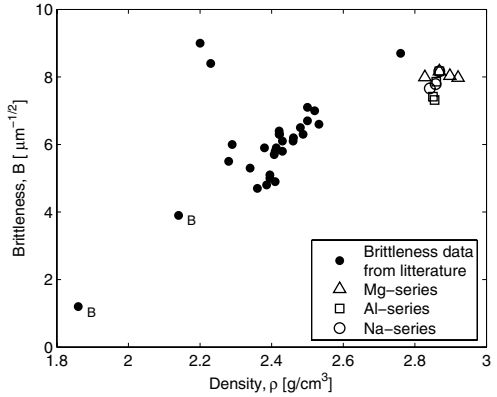

*Figure 4. Brittleness (*B*) of all the glass series as a function of glass density plotted together with brittleness data measured by Sehgal* et al.[26] *The two points marked with* B *are B_2O_3 based glasses, whereas the rest are SiO_2-based glasses*

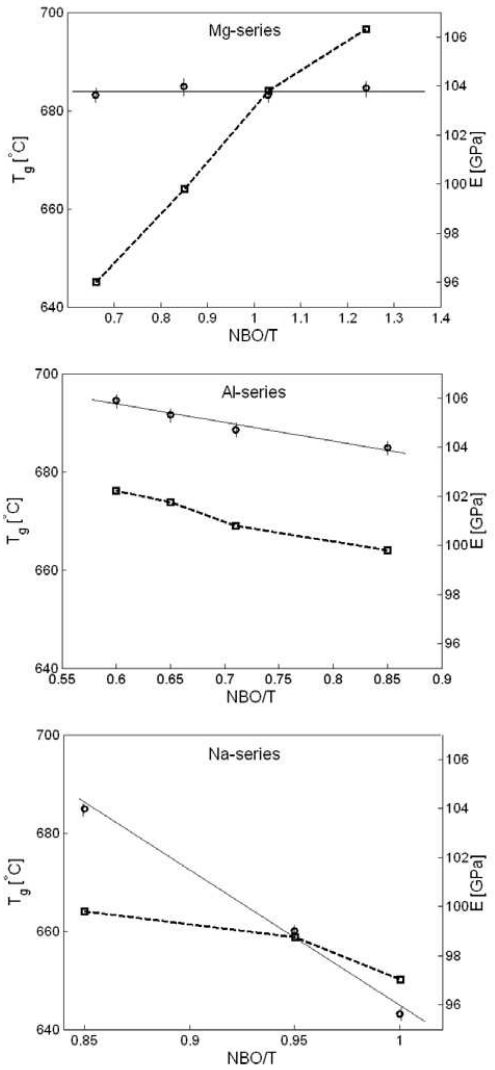

Figure 5. Glass transition temperature, T_g (—o—) and Young's modulus (--□--) as a function of NBO/T in the Mg-, Al- and Na-series. The lines are a guide for the eyes

3.2. Glass transition and crystallisation

The glass transition temperature, the crystallisation onset temperature and liquidus temperature were all measured using DSC, where T_l was defined as the offset temperature of the last melting peak. Liquidus calculations based on Nathan & van Kirk approach[31] were performed, but due to the complexity of the crystalline phases it was not possible to obtain reasonable T_l values. In all glasses the melting endotherm starts directly after the crystallisation exotherm, and in some cases they overlap. For all glass series T_g is shown as a function of NBO/T in Figure 5 and T_c and

T_l as a function of NBO/T are shown in Figure 6. All T_g, T_c and T_l values are given in Table 2.

For the Mg-series T_g remains constant within the error range of ±2°C, while T_c at first rises with addition of MgO, and then decreases with further additions. The liquidus temperature shows the opposite trends. The higher crystallisation temperature of glass 2 compared to glass 1 is associated with the overall optimal composition of glass 2 in terms of its relation to the crystallising phases. Glass 2 has only one crystalline phase, which can be seen when the glass melts; compared to the other glasses it has only one endotherm in the melting curve, while the other glasses have a secondary endotherm at a higher temperature. This is illustrated in Figure 7 where DSC heating curves for glass 2 and 7 are shown, where glass 2 has only one melting peak and glass 7 has up to four crystal phases as defined from the amount of local minima in the melting endotherm. Thus the liquidus temperature is lower for glass 2 as the high-melting crystal phases are absent (figures showing all the melting peaks can be found in Lonnroth[32]). The observed decrease in T_c and increase in T_l from glass 2 to 4 is dramatic, and can only be caused by a major change in the network structure. This can be understood by looking at the total amount of network modifiers compared to network formers (Equation (7)). This ratio changes drastically with the increases in MgO content.

$$\mathrm{M/F} = \frac{\text{modifiers}}{\text{formers}} = \frac{\sum(\mathrm{Na_2O, K_2O, MgO, CaO})}{\sum(\mathrm{SiO_2, Al_2O_3})} \quad (7)$$

With the initial increase in MgO (glass 2) there are still more network formers than modifiers M/F=0·72 (as is the usual case in network glasses). In glass 4 the increase in MgO is so large that there is an equal amount of network modifiers and formers, M/F=0·97 ≈1. This makes the amorphous structure less stable to temperature increases and, hence the glass crystallises easily, so that a decrease in T_c and an increase in T_l are observed. Glass 3 is intermediate between these two with M/F=0·83. The constant glass transition temperature of this series can be described by the overall glass structure that in general determines T_g. The glass transition is governed both by connectivity, i.e. the degree of polymerisation and the average bond strengths, which includes both glass forming ion–oxygen bonds and also glass modifying ion–oxygen bonds. The addition of MgO decreases the polymerisation of glass network, as assumed, but at the same time MgO has a strong ionic bond, stronger than other network modifiers present in the studied glasses, which strengthens the network. These two effects may cancel out each other, and hence, no change in T_g is observed with additions of MgO.

For the Na-series, the increase in the alkali modifier concentration causes a continuous decrease in the characteristic temperatures T_g, T_c and T_l. This

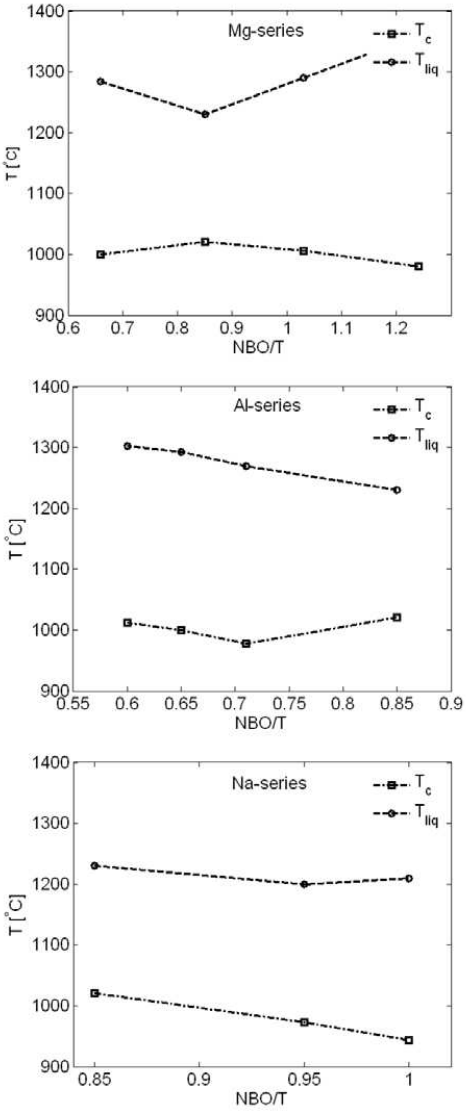

Figure 6. T_c *and* T_l *as a function of NBO/T in the Mg-, Al- and Na-series*

is directly related to the overall glass structure. An increase in the Na^+ content leads to an increase of the nonbridging oxygen, i.e. to weakening of the network, and hence, reduction of the degree of polymerisation. At the same time, the average bond strength decreases due to the weak bonds between Na^+ and oxygen ions. Therefore the addition of Na_2O decreases T_g, i.e. the glass transforms to a liquid at lower temperatures. Generally, the increasing Na^+ concentration makes the liquid less viscous. The high mobility of Na^+, the weak bonding of the sodium ions and the low network connectivity (or polymerisation)

of the high sodium glass, all account for the decrease in both T_c and T_l. Glass 8 has also only one melting peak, indicating that also this composition is optimal with respect to crystallisation.

The increase in Al_2O_3 causes an increase in T_g, indicating that increased concentration of aluminium tetrahedra in the silica network makes the structure more rigid and more polymerised. As each Al^{3+} binds one NBO of the Si^{4+} tetrahedron, NBO/T becomes smaller and the degree of polymerisation of the network increases. Further the modifier ions used by aluminium in charge balancing are more firmly bound to their sites than when bound to a NBO. The crystallisation temperature decreases dramatically with the first addition of Al_2O_3 (i.e. T_c changes from 1021 to 978°C when Al_2O_3 increases from 11·63 to 13·32 mol%.) but with further increase of Al_2O_3 T_c increases again up to 1012°C. Generally, alumina strengthens the glass network so that more thermal energy is required to transfer the glass to a crystalline state, which is noted in the Al-series in glasses 5 to 7 as an increase in T_c. The higher crystallisation temperature of glass 2 relative to the other glasses was discussed earlier.

For the Al- and the Na-series (where there is less than one NBO per tetrahedra) Young's modulus follows the same trends as T_g (Figure 5). Both T_g and Young's modulus increase with increasing Al_2O_3 content and decrease with increasing Na_2O content. The density in the Al-series decreases with increasing Al_2O_3 i.e., with decreasing NBO/*T*.

3.3. Melt fragility

High temperature viscosities and the viscosity at T_g were fitted with the Avramov and Milchev equation (AM equation)[33–34]

$$\eta = \eta_\infty \exp\left[\varepsilon\left(\frac{T_r}{T}\right)^\alpha\right] \quad (8)$$

where η_∞ is the high temperature viscosity, ε is a dimensionless activation energy at the glass transition temperature, T_r is a reference temperature and α is the fragility parameter. For oxide glasses, this equation can be transformed into the following expression[19,35–36]

$$\log\eta = A + (12 - A)\left(\frac{T_g}{T}\right)^\alpha \quad (9)$$

where A=log η_∞. From Equation (9) it is seen that log η=12, when T=T_g. This correlation has been verified for oxide glasses.[19,36] The measured viscosity data are shown in Figure 8 as a function of temperature scaled by T_g.[37] The obtained data are fitted with Equation (9), where α determines the curvature, i.e. the degree of departure from the Arrhenian behaviour, and hence, the fragility of liquid.[19,33,37] The viscosity values are reported elsewhere.[32] The parameters obtained for each glass are given in Table 3. For the Al-series it can be seen that increasing the Al_2O_3 content makes the melt stronger, since α becomes smaller. This is also an indication of the enhanced polymerisation of the network due to formation of [AlO_4] tetrahedra. In the Mg-series another trend is observed regarding the changes in the melt fragility with increasing the MgO content. It is seen that among the Mg-series glass 1 has the lowest MgO content and the smallest fragility. With increasing MgO content the fragility increases (from glass 1 to 2) and then remains approximately constant (from glass 2 to 4). This implies that MgO makes the melt more fragile. However, further studies are needed to find a more precise trend of the changes of melt fragility with the MgO content. In the Na-series the melt fragility slightly decreases with an increase of Na_2O (from glass 2 to glasses 8 and 9). This is understandable when considering the weaker bonding between alkali and oxygen ions in comparison to the bonding between the earth alkaline and oxygen ions. The stronger bonding causes a stronger attraction of oxygen ions by the cations, and hence, larger flow units. Thus, the energy barriers for viscous flow at around T_g are higher for the MgO containing glasses than for the Na_2O containing glasses. In other words, the former glasses are more fragile than the latter ones. This is evidenced by the slightly larger fragility of glasses 3 and 4 compared with glasses 8 and 9. With increasing NaO content (i.e. replacing earth alkaline oxides and glass forming oxides), the flow units become smaller, and thus, the melt fragility slightly decreases. Clearly the melt fragility is expected to decrease considerably when adding considerable amounts of Na_2O.

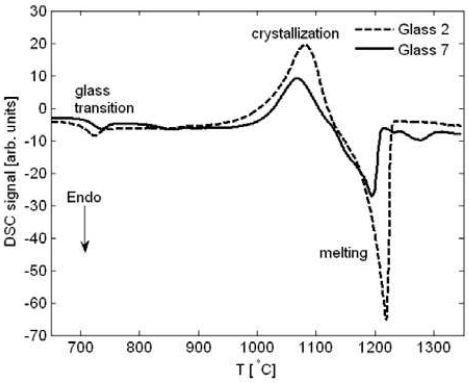

Figure 7. DSC heating curves for glasses 2 and 7 measured with a heating rate of 20K/min. The melting peak of glass 2 is a single well defined peak, while the main melting endotherm of glass 7 consists of two overlapping peaks and there are two smaller endotherms at even higher temperatures, i.e. the melting peaks of the high melting phases. The liquidus temperature of a glass was determined as the temperature at the offset of the last melting endotherm.

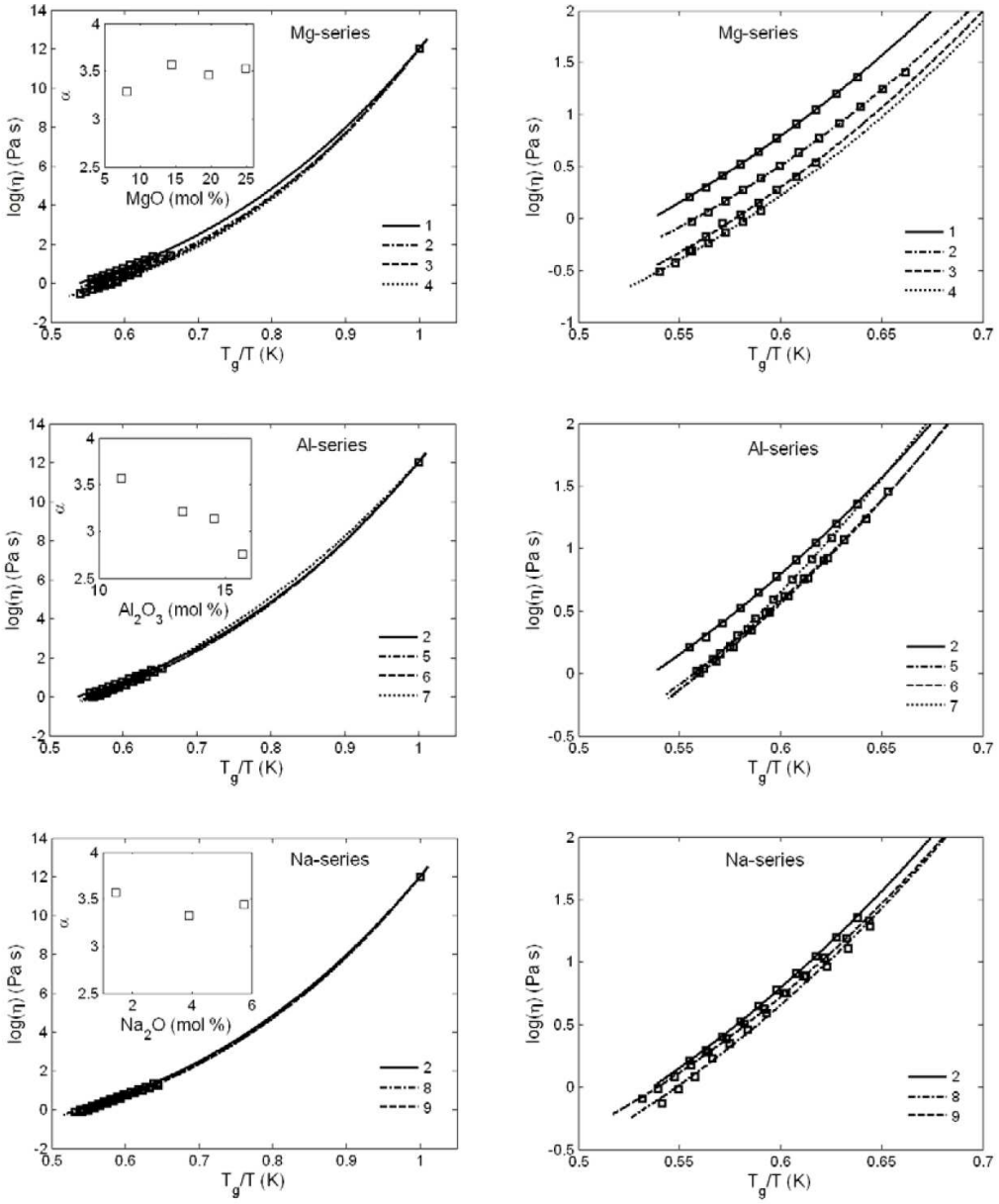

Figure 8. Viscosity (η) as a function of the T_g *scaled temperature for the Mg-, Al- and Na-series. Left panel:* η *for the whole temperature range. Inset: Fragility parameter (*α*) as a function of the respective increase of oxides. Right panel:* η *for the high temperature range*

4. Conclusions

A basaltic glass with additions of MgO, Al_2O_3 and Na_2O has been studied with respect to the characteristic temperatures (T_g, T_c and T_l), rheological parameters (viscosity and fragility), mechanical parameters (hardness, fracture toughness, Young's modulus and brittleness) and network indicators (density and the number of nonbridging oxygens). Changes in both the thermal and mechanical properties of the glasses can be related to modifications of the network structure of the glass. The compositions of glasses 2 and 8 have higher tendencies to form uniform crystalline phases than the other compositions studied, as only one crystalline phase

*Table 3. Characteristic temperatures of the glasses, T_g, T_c and T_l were measured by DSC, and the glasses that have only one melting peak are marked by *. The Avramov parameters are based on fitting the measured viscosity data to Equation (9)*

	Specific temperatures			*Avramov parameters*		
Glass	T_g *(°C)*	T_c *(°C)*	T_{liq} *(°C)*	$\log \eta_\infty$	T_g *(K)*	α
1	683	1000	1280	−1·78	956	3·29
2	685	1021	1232*	−1·71	958	3·57
3	683	1006	1295	−2·11	956	3·46
4	685	980	1355	−2·11	958	3·53
5	689	978	1270	−2·17	962	3·21
6	692	1000	1295	−2·32	965	3·14
7	695	1012	1305	−3·02	968	2·76
8	660	973	1200*	−1·89	933	3·32
9	643	944	1210	−1·63	916	3·44

is observed. The changes of the measured properties with addition of oxides can be interpreted by the role that the substituted oxides play in the glass network structure.

Generally, all the studied glasses have high density and are hard and brittle compared to glasses in the soda–lime–silica system. In particular an increase of the MgO content results in hard and brittle glasses with fragile melts that crystallise easily, i.e. they are not good glass formers. High MgO glass possesses large NBO/T, high density and high Young's modulus. In contrast, an increase of Na_2O content causes a decrease in hardness, brittleness and fracture toughness. Larger changes in Young's modulus and T_g are observed in the glasses with additions of Al_2O_3, where both Young's modulus and T_g increase with increasing Al_2O_3 content. All of the investigated glasses are relatively fragile systems, although a reduction in the fragility is observed with Al_2O_3 substitutions as alumina increases the degree of the network polymerisation.

Acknowledgements

We thank Rockwool International A/S for financial support, and Ralf Keding and Lothar Wondraczek for performing the XRD and Young's modulus measurements, respectively.

References

1. Wojnárovits, I. *Glastech. Ber.*, 1988, **61** (6), 157–60.
2. Bauer, J. F. *Int. Nonwovens J.*, 2004, **13** (4), 2–7.
3. Gur'ev, V. V., Neproshin, E. I. & Mostovoi, G. E. *Glass Ceram.*, 2001, **58**, 62–5.
4. Rincon, J. M., Cáceres, J., Cáceres, D. O., Russo, C. J. G.-O., Petkova, A. & Hristov, H. J. *Therm. Anal. Calorim.*, 1999, **56**, 931–8.
5. Matović, B., Bošković, S. & Logar, M. *J. Serb. Chem. Soc.*, 2003, **68** (6), 505–10.
6. Yilmaz, S., Bayrak, G., Sen, S. & Sen, U. *Mater. Design*, 2006, **27**, 1092–6.
7. Ferreira, E. B. & Zanotto, E. D. *Glass Sci. Tech.*, 2002, **75** (2), 75–86.
8. Agarwal, G., Hong, K. S., Fletcher, M. R. & Speyer, R. F. *J. Non-Cryst. Solids*, 1991, **130**, 187–97.
9. Burkhard, D. J. M. *J. Petrol.*, 2001, **42** (3), 507–27.
10. Burkhard, D. J. M. *Contrib. Miner. Petrol.*, 2002, **142**, 724–37.
11. Schilling, F. R., Sinogeikin, S. V., Hauser, M. & Bass, J. D. *J. Geophys. Res*, 2003, **108** (B6), 10.1029/2001JB000517.
12. Bouhifd, M. A., Richet, P., Besson, P., Roskosz, M. & Ingrin, J. *Earth Planetary Sci. Lett.*, 2004, **218**, 31–44.
13. Solvang, M., Yue, Y. Z. & Jensen, S. L. *J. Non-Cryst. Solids*, 2004, **345 & 346**, 782–6.
14. Webb, S. *Eur. J. Mineral.*, 2005, **17**, 223–32.
15. Giordano, D., Mangiacapra, A., Potuzak, M., Russel, J. K., Romano, C., Dingwell, D. B. and Di Muro, A. *Chem. Geol.*, 2006, **229**, 42–56.
16. Mysen, B., Virgo, D. & Kushiro, I., *Am. Miner.*, 1981, **66**, 678–701.
17. McMillan, P., Piriou, B. & Navrotsky, A.. *Geochim. Cosmochim. Acta*, 1982, **46**, 2021–37.
18. Engelhardt, G., Nofz, M., Forkel, K., Wihsmann, F. G., Mägi, M., Samonson, A. & Lippmaa E., *Phys. Chem. Glasses*, 1985, **26** (5), 157–65.
19. Yue, Y. Z. *J. Non-Cryst. Solids*, 2008, **354**, 1112–18.
20. Lawn, B. *Fracture of brittle solids*. Cambridge Solid State Science. Cambridge University Press, Second Edition, 1993.
21. Sehgal, J., Nakao, Y., Takahashi, H. & Ito, S. *J. Mater. Sci. Lett.*, 1995, **14**, 167–9.
22. Lawn, B. R. & Marshall, D. B. *J. Am. Ceram. Soc.*, 1979, **62** (7–8), 347–50.
23. Sehgal, J. & Ito, S. *J. Am. Ceram. Soc.*, 1998, **82** (9), 2485–8.
24. Solvang, M. *Rheological and thermodynamic response to compositional variation in high aluminosilicate melts.* 2002. PhD thesis, Aalborg University, Denmark.
25. Gao, F., He, J., Wu, E., Liu, S., Yu, D., Li, D., Zhang, S. & Tian, Y. *Phys. Rev. Lett.*, 2003, **91** (1).
26. Sehgal, J. & Ito, S. *J. Non-Cryst. Solids*, 1999, **253**, 126–32.
27. Ito, S. *J. Ceram. Soc. Jpn*, 2004, **112** (9), 477–85.
28. Deriano, S., Rouxel, T., LeFloch, M. & Beuneu, B. *Phys. Chem. Glasses*, 2004, **45** (1), 37–44.
29. Lin, C.C. & Liu L.G., *Phys. Chem.Miner.*, 2006, **33**, 332–46.
30. Yoshida, S., Hidaka, A. & Matsuoka, J. *J. Non-Cryst. Solids*, 2004, **344**, 37–43.
31. Nathan, H. D. & Van Kirk, C. K. *J. Petrol.*, 1978, **19**, 66–94.
32. Lonnroth, N. *Physical properties of basaltic glasses*. 2007. PhD thesis, Aalborg University, Denmark.
33. Avramov, I. & Milchev, A. *J. Non-Cryst. Solids*, 1988, **104**, 253–60.
34. Avramov, I. *J. Non-Cryst. Solids*, 1998, **238**, 6–10.
35. Solvang, M., Yue, Y. Z., Jensen, S. L. & Dingwell, D. *J. Non-Cryst. Solids*, 2004, **336**, 179.
36. Yue, Y. Z., von der Ohe, R. & Jensen, S. L. *J. Chem. Phys.*, 2004, **120**, 8053–9; 2004, **121** (22), 11508.
37. Angell, C. A. *Science*, 1995, **267**, 1924–35.